On the Evolution of Massive Stellar Triples

by

Jakob Stegmann

A Thesis submitted to Cardiff University
for the degree of Doctor of Philosophy

July 3, 2023

Summary

Most massive stars are found in hierarchical triples or higher multiplicity systems, in which a close inner binary is orbited by one or more distant companions. Here, we present a new triple stellar evolution code, `TSE`, which simultaneously takes into account the physics of the stars and their gravitational interaction. `TSE` is used to simulate the evolution of massive stellar triples in the galactic field from the zero-age-main-sequence until they form compact objects. To this end, we implement initial conditions that incorporate the observed high correlation between the orbital parameters of early-type stars. We show that the interaction with a tertiary companion can significantly impact the evolution of the inner binary. For instance, high eccentricities can be induced by the third-body dynamical effects, leading to a Roche-lobe overflow or even to a stellar merger from initial inner binary separations $10^3 - 10^5\,\mathrm{R}_\odot$.

Focusing on the evolution subsequent to a stellar merger, we find that binaries composed of the merger product star and the tertiary companion provide a new source to form binary black hole mergers in the Galactic field. By means of a population synthesis, we estimate their contribution to the total black hole merger rate to be $\mathcal{R}(z=0) = 0.3 - 25.2\,\mathrm{Gpc}^{-3}\,\mathrm{yr}^{-1}$. Merging binary black holes that form from stellar post-merger binaries have exceptionally low mass ratios. We identify a critical mass ratio $q \simeq 0.5$ below which they could dominate the total black hole merger rate in the field.

Lastly, we study the dynamical evolution of the spin vector of a massive donor star that stably transfers mass to a binary companion. Assuming that the donor star loses its mass along the instantaneous interstellar axis, we find that the ejection of $\gtrsim 30$ per cent of the donor's initial mass causes its spin to nearly flip onto the orbital plane of the binary, independently of the initial spin-orbit alignment.

Publications

First Author Publications

Stegmann & Vermeulen (2023)

Stegmann et al. (2022b)

Stegmann et al. (2022a)

Stegmann & Antonini (2021)

Stegmann et al. (2020)

List of abbreviations

BH	Black hole
NS	Neutron star
BBH	Binary black hole
BNS	Binary neutron star
NSBH	Neutron star black hole binary
DCO	Double compact object
SN	Supernova
GW	Gravitational wave
LK	Lidov-Kozai
RLO	Roche-lobe overflow
CE	Common-envelope
MS	Main-sequence
ZAMS	Zero-age-main-sequence
HG	Hertzsprung gap

Contents

Acknowledgements

I would like to express my sincere gratitude to my thesis advisor Fabio Antonini, for his invaluable guidance, unwavering support, and encouragement throughout my doctoral journey. His expertise, knowledge, patience, and mentorship have been instrumental in shaping my research and professional development.
I am also grateful to the members of my thesis committee, Vivien Raymond and Wolfgang Langbein, for their insightful feedback, constructive criticism, and valuable suggestions. Their expertise and diverse perspectives have enriched my research and contributed to the quality of my thesis.
I would like to thank my colleagues at Cardiff University, especially Sander Vermeulen, Jordan Barber, Debatri Chattopadhyay, Aldo Ejlli, Lorenzo Aiello, Michael Norman, William Griffiths, Philip Relton, Panagiota Kolitsidou, Alasdair James, Charlie Hoy, Virginia D'Emilio, and Cameron Mills for their intellectual stimulation, support, and camaraderie. Their friendship and encouragement have made my PhD experience enjoyable and memorable.
Last but not least, I would like to express my deepest appreciation to my family and friends for their support and encouragement. Their unwavering belief in me and my abilities has been a source of strength and inspiration throughout my PhD journey.

Chapter 1

Introduction

Stars are the fundamental building block of our Universe. Whereas our own sun evolves in isolation, many stars in the Galactic field are born gravitationally bound to each other in so-called multiple systems, e.g., in binaries, triples, or higher-order configurations. Perhaps the most famous example of a stellar triple can be found in our own astronomical backyard. α Centauri which at a distance $d \approx 1.3\,\mathrm{pc}$ is the closest stellar system to our own Solar System consists of three stars that are bound to each other: The primary and secondary stars, α Cen A and B, are solar-like stars that form an inner binary system with an orbital period of about $P_{\mathrm{in}} = 80\,\mathrm{yr}$. The third star, Proxima Centauri, is a smaller and fainter red dwarf that orbits the binary system at a much longer period of approximately $P_{\mathrm{out}} = 5.5 \times 10^5\,\mathrm{yr}$ (Kervella et al., 2017).

From a statistical point of view, multiple systems and particularly triples are most common among stars that are more massive than those of α Centauri. Observational campaigns of massive stars exhibit a large fraction of binaries, triples, and higher-order multiples (Mason et al., 1998; Preibisch et al., 1999; Mason et al., 2009; Duchêne & Kraus, 2013; Sana et al., 2014). For instance, Preibisch et al. (1999); Mason et al. (2009); GRAVITY Collaboration et al. (2018) find that each massive O and B-type member of the Orion Nebula cluster has at least 1.5 companions on average (see Fig. 1.1). Likewise, more than 200 O-type stars of the "Southern Massive Stars at High Angular Resolution Survey" (SMASH+) exhibit an average companion frequency of 2.2 ± 0.3 (Sana et al., 2014). This demonstrates that most massive stars are formed in multiple systems (Moe & Di Stefano, 2017).

It is a well-established fact that stellar multiplicity affects the way how massive stars evolve. For example, if two massive stars are placed in a binary they are prone to interact with each other (Sana et al., 2012), e.g., by torquing each other's rotational angular momentum through tidal forces (Hut, 1981; Zahn, 1989; Eggleton et al., 1998; Hurley et al., 2002), transferring mass from one to another (Paczyński, 1971; Eggleton, 1983; Eldridge et al., 2008; Sana et al.,

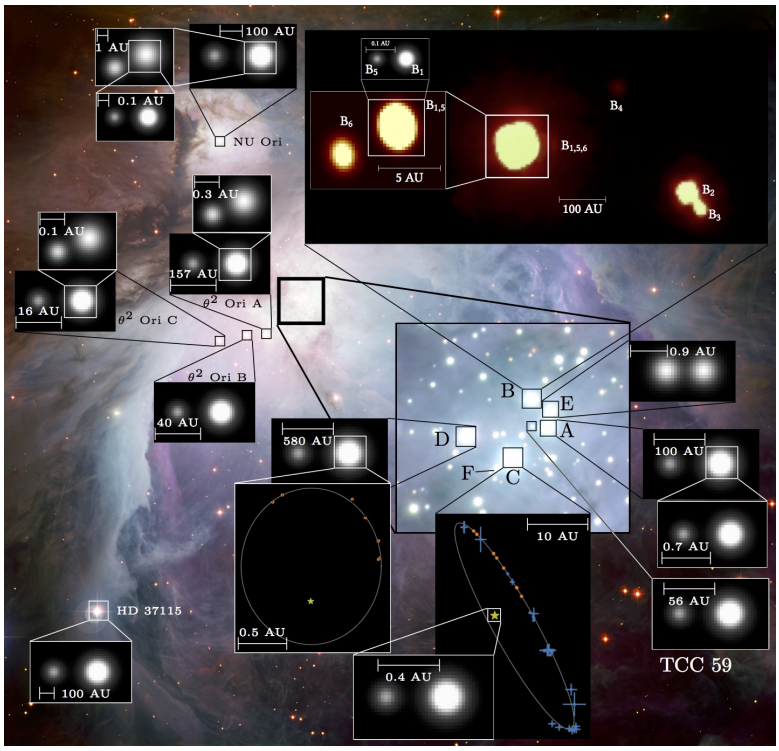

Figure 1.1. Orion's Trapezium Cluster in which 11 of 16 observed systems are confirmed multiples, with a total number of 22 companion stars. Credit: GRAVITY Collaboration et al. (2018).

2012; Schneider et al., 2021), engulfing each other in a common-envelope (CE) (Paczynski, 1976; Ivanova et al., 2013), or forming a bigger star through a stellar merger (Bonnell & Bate, 2005; Schneider et al., 2019). Moreover, the evolution of massive binary stars could lead to the formation of merging binary black holes (BBHs) and neutron stars (BNSs) (Belczynski et al., 2016a, 2020) whose gravitational-wave (GW) emission was recently directly detected for the first time (Abbott et al., 2016, 2017; The LIGO Scientific Collaboration et al., 2021).

What makes triples special is their dynamical evolution which can significantly differ from that of isolated binaries. In certain regions of parameters space the secular gravitational perturbation from the tertiary companion leads to large-amplitude oscillations of the inner binary eccentricity and orbital direction which are often referred to as Lidov-Kozai (LK) (Kozai, 1962; Lidov, 1962) or von Zeipel-Lidov-Kozai oscillations (Ito & Ohtsuka, 2019). This phenomenon has been studied in a wide range of astrophysical contexts from planetary and stellar systems to super-massive black holes (BHs) at the centres of galaxies (Naoz, 2016). For instance, LK oscillations have been attributed to the formation of Hot Jupiters which are giant planets observed on very close orbits around their host star (Naoz et al., 2011, 2012; Dong et al., 2014; Storch et al., 2014; Antonini et al., 2016a; Muñoz et al., 2016; Hamers & Lai, 2017; Storch et al., 2017; Stephan et al., 2018; Grishin et al., 2018; Vick et al., 2019). In this situation the Jovian planet is presumably formed

from a protoplanetary disk at much wider distance. The gravitational perturbation from a tertiary companion, e.g., an additional planet, could cause an inward-migration of the Jovian planet. By promoting a close pericentre passage during an LK cycle tidal dissipation of the planetary orbit becomes efficient and effectively captures the planet on a close circularising orbit (Naoz et al., 2011).

Applied to massive stars, one can expect a tertiary companion to enrich the variety of evolutionary pathways of the stellar system. A tertiary companion could facilitate the stellar interactions between the inner binary stars via the LK mechanism by effectively reducing the minimum periapsis. Previous studies of stellar triples have shown that these may give rise to X-ray binaries (Naoz et al., 2016) or even trigger a stellar merger (Perets & Kratter, 2012; Stegmann et al., 2022a; Vigna-Gómez et al., 2022) leading to the formation of Blue stragglers (Perets & Fabrycky, 2009; Naoz & Fabrycky, 2014; Antonini et al., 2016b) and type Ia SN (Iben & Tutukov, 1999; Thompson, 2011). A merger taking place in a triple or a higher-order configuration also opens up the possibility for sequential mergers (Hamers & Safarzadeh, 2020; Vigna-Gómez et al., 2021; Stegmann et al., 2022a). Moreover, an expanded tertiary star could itself overflow its Roche-lobe (RLO) and initiate a mass transfer phase onto the inner binary (de Vries et al., 2014; Portegies Zwart & Leigh, 2019; Di Stefano, 2020a,b; Hamers et al., 2021).

Modelling massive stellar triples will also help to understand the astrophysical origin of the binary mergers detected by the GW detectors LIGO and Virgo (Abbott et al., 2019, 2021a,b; The LIGO Scientific Collaboration et al., 2021). It is unknown whether they resulted from isolated binary stellar evolution in which the binary stars harden during a CE or stable mass transfer phase (Dominik et al., 2012; Belczynski et al., 2016a; Hoang et al., 2018; Giacobbo & Mapelli, 2018; Olejak et al., 2021; van Son et al., 2022) or via three-body interaction with a bound hierarchical companion (Silsbee & Tremaine, 2017; Antonini et al., 2017, 2018; Liu & Lai, 2018; Rodriguez & Antonini, 2018; Fragione & Kocsis, 2020; Martinez et al., 2022), or if they were driven by some dynamical interaction within a dense stellar environment, e.g., the dense cores of globular clusters (Rodriguez et al., 2016a; Park et al., 2017; Rodriguez & Loeb, 2018; Antonini & Gieles, 2020), massive young clusters (Banerjee et al., 2010; Ziosi et al., 2014; Di Carlo et al., 2019; Fragione & Banerjee, 2021), and galactic nuclei (Antonini & Perets, 2012; Prodan et al., 2015; Antonini & Rasio, 2016; Petrovich & Antonini, 2017; Hamilton & Rafikov, 2019; Bub & Petrovich, 2020; Wang et al., 2021), or if the merger population formed in a combination of these channels (Zevin et al., 2021).

The main scientific goal of this thesis is to study the evolution of massive triples in order to address some of these problems. In this chapter, we begin to introduce the dynamics of hierarchical three-body systems and outline the key topics which are addressed in this thesis.

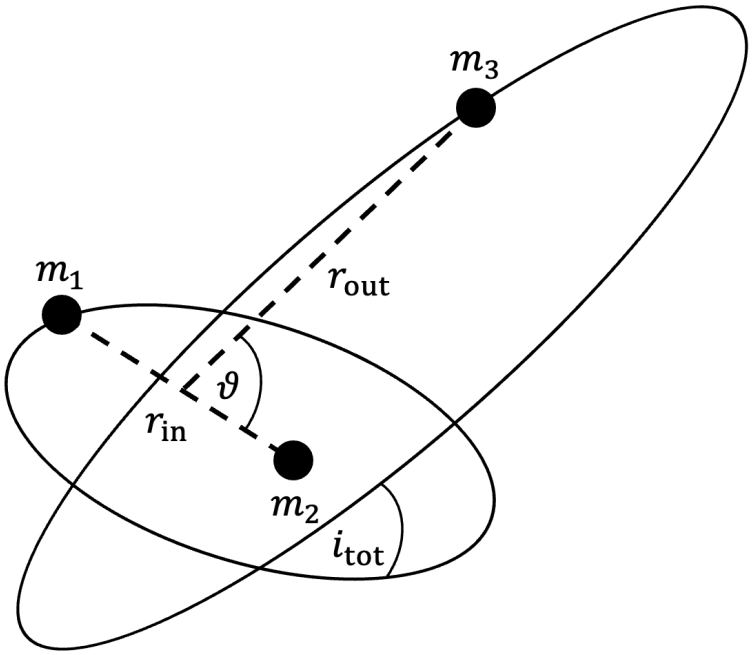

Figure 1.2. Schematic representation of a hierarchical triple of point masses. The inner orbit consists of the two masses m_1 and m_2 whose centre of mass is orbited by another much more distant tertiary companion (outer orbit). Both orbital planes are inclined w.r.t. each other by some relative inclination angle i_{tot} and ϑ is the angle between the instantaneous position vectors $\mathbf{r}_{\mathrm{in}}$ and $\mathbf{r}_{\mathrm{out}}$.

1.1 Secular dynamics of three-body systems

Determining the motion of three point masses (or celestial bodies) that interact with each other through Newtonian gravity has been a long-standing challenge in physics known as the three-body problem. It can be dated back to work by, e.g., Newton, Euler, Laplace, Lagrange, and Poincairé. Despite its apparent simplicity and similarity to the two-body (Kepler) problem the general three-body problem has no closed-form solution. Yet, in the early 20-th century Finnish mathematician Karl Sundman proved the existence of a convergent infinite series that solves the general problem, but due to its slow convergence it is of no practical use (Gowers et al., 2008).

The three-body problem simplifies in certain special configurations that are relevant to celestical mechanics. For instance, the restricted three-body problem applies if one of the celestial bodies has a negligible mass, e.g., in the case of moons, planetoids, or satellites, while the other bodies with non-negligible mass essentially move around each other on a Keplerian orbit. Thus, the orbit of the massless component can be found using perturbation theory (Gowers et al., 2008).

In addition, most of the triples in our Universe are stable over a long timescale due to some hierarchy (Hayashi et al., 2023), in which the centre of mass of a close inner binary is orbited by

another distant tertiary companion (see Fig. 1.2). Hierarchical triples are the primary subject of this work. Their dynamical evolution can be written in terms of two Keplerian orbits: the inner orbit (denoted by the subscript in) described by the relative position vector $\mathbf{r}_{\mathrm{in}}$ between the inner binary masses m_1 and m_2, and the outer orbit (subscript out) described by the relative position vector $\mathbf{r}_{\mathrm{out}}$ between the inner binary centre of mass and m_3. Both orbits carry some orbital angular momentum

$$\mathbf{G}_{\mathrm{in(out)}} = \mu_{\mathrm{in(out)}}\mathbf{r}_{\mathrm{in(out)}} \times \frac{\mathrm{d}\mathbf{r}_{\mathrm{in(out)}}}{\mathrm{d}t} = L_{\mathrm{in(out)}}\mathbf{j}_{\mathrm{in(out)}}, \tag{1.1}$$

where

$$L_{\mathrm{in(out)}} = \mu_{\mathrm{in(out)}}\sqrt{G m_{\mathrm{in(out)}} a_{\mathrm{in(out)}}} \tag{1.2}$$

denote the circular angular momenta. Furthermore, $m_{\mathrm{in}} = m_1 + m_2$ and $m_{\mathrm{out}} = m_1 + m_2 + m_3$ are the total masses of the inner and outer binary, $\mu_{\mathrm{in}} = m_1 m_2/m_{\mathrm{in}}$ and $\mu_{\mathrm{out}} = m_{\mathrm{in}} m_3/m_{\mathrm{out}}$ their reduced masses, and $a_{\mathrm{in(out)}}$ their semi-major axes. The directions of $\mathbf{G}_{\mathrm{in(out)}}$ are specified by the dimensionless angular momentum vectors $\mathbf{j}_{\mathrm{in(out)}} = [1 - e^2_{\mathrm{in(out)}}]^{1/2}\hat{\mathbf{j}}_{\mathrm{in(out)}}$ which point along the orbit axes with $e_{\mathrm{in(out)}}$ denoting the eccentricities of the orbits. A summary of common variables which are used throughout this work is given in Table 1.1.

As we will see, in this hierarchical configuration, the inner and outer binary can torque each other by exchanging angular momentum which changes the shape of each orbit over long-term secular timescales. Meanwhile, the total angular momentum vector must be a constant defined as

$$\mathbf{G}_{\mathrm{tot}} = \mathbf{G}_{\mathrm{in}} + \mathbf{G}_{\mathrm{out}} = \mathrm{const.} \tag{1.3}$$

We may denote the inclination angle between the total angular momentum vector and the orbital axes as $i_{\mathrm{in(out)}}$ and their relative inclination $i_{\mathrm{tot}} = i_{\mathrm{in}} + i_{\mathrm{out}}$ is given by the geometry of the system as

$$\cos(i_{\mathrm{tot}}) = \frac{G^2_{\mathrm{tot}} - G^2_{\mathrm{in}} - G^2_{\mathrm{out}}}{2G_{\mathrm{in}}G_{\mathrm{in}}}. \tag{1.4}$$

One of the most important dynamical relations can be qualitatively understood by considering the construction of the constant total angular momentum vector from Eq. (1.3). If we allow both orbits to torque each other by changing either one of the eccentricities $e_{\mathrm{in(out)}}$, the lengths of the orbital angular momenta $G_{\mathrm{in(out)}} \propto [1 - e^2_{\mathrm{in(out)}}]^{1/2}$ get rescaled. Consequently, it must also affect the relative inclination i_{tot} of the two orbits in order to conserve the total orbital angular momentum vector (cf., Fig. 1.3). Thus, the *simultaneous* change of the orbital eccentricities and relative inclination follows from simple geometric considerations, and, as we will see below, are described by the LK oscillations.

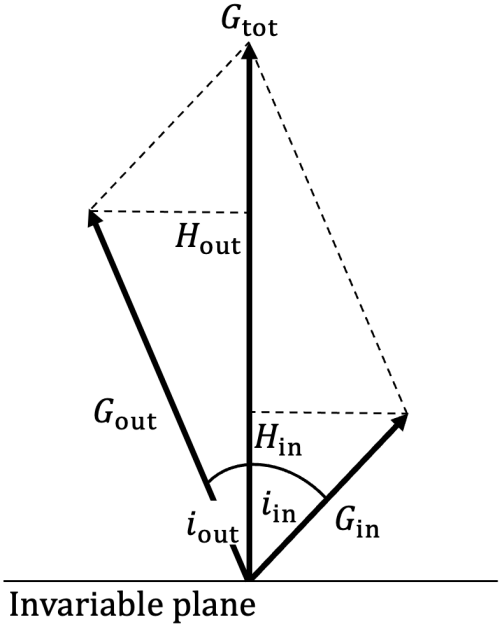

Figure 1.3. Schematic representation of the invariable plane which is perpendicular to the conserved total angular momentum vector $\mathbf{G}_{\rm tot} = \mathbf{G}_{\rm in} + \mathbf{G}_{\rm out}$. The inclinations $i_{\rm in(out)}$ are defined as the angles between $\mathbf{G}_{\rm in(out)}$ and $\mathbf{G}_{\rm tot}$, and $\mathbf{H}_{\rm in(out)}$ are the projections (i.e., z-components) of $\mathbf{G}_{\rm in(out)}$ onto the latter.

In the remainder of this section, we will derive the general equations of motion for the long-term evolution of hierarchical triples from their Hamiltonian (following Tremaine et al., 2009; Naoz et al., 2013a; Tremaine & Yavetz, 2014; Liu et al., 2015; Naoz, 2016) and discuss key aspects of their dynamics. For this purpose, it is instructive to make use of the conservation of $\mathbf{G}_{\rm tot}$ by introducing some fixed inertial frame in which the z axis is parallel to the latter. The $x-y$ plane which is perpendicular to the total angular momentum vector is often referred to as invariable plane.

In this frame, it is convenient to describe the orbital dynamics of the inner and outer orbit in terms of action-angle variables, the Delaunay elements (e.g., Merritt, 2013). Thus, we associate with each of the inner and outer orbits three actions: the magnitudes of the orbital angular momenta $G_{\rm in(out)}$, their z-components $H_{\rm in(out)} = G_{\rm in(out)}\cos(i_{\rm in(out)})$, and the circular angular momenta $L_{\rm in(out)}$. The corresponding angles, i.e., conjugate momenta, are the arguments of the periapses $g_{\rm in(out)}$, the longitudes of the ascending nodes $h_{\rm in(out)}$, and the mean anomalies $l_{\rm in(out)}$, respectively, which are commonly used in celestial mechanics to parameterise the orbital motion.

The Delaunay elements relate to the components of the instantaneous position vectors of the

inner and outer orbit as (e.g., Merritt, 2013)

$$\mathbf{r}_{\mathrm{in(out)}} = r_{\mathrm{in(out)}} \times \begin{pmatrix} \cos(h_{\mathrm{in(out)}})\cos(f_{\mathrm{in(out)}}+g_{\mathrm{in(out)}}) - \cos(i_{\mathrm{in(out)}})\sin(h_{\mathrm{in(out)}})\sin(f_{\mathrm{in(out)}}+g_{\mathrm{in(out)}}) \\ \sin(h_{\mathrm{in(out)}})\cos(f_{\mathrm{in(out)}}+g_{\mathrm{in(out)}}) + \cos(i_{\mathrm{in(out)}})\cos(h_{\mathrm{in(out)}})\sin(f_{\mathrm{in(out)}}+g_{\mathrm{in(out)}}) \\ \sin(i_{\mathrm{in(out)}})\sin(f_{\mathrm{in(out)}}+g_{\mathrm{in(out)}}) \end{pmatrix}, \tag{1.5}$$

where the true anomalies $f_{\mathrm{in(out)}}$ are connected to the mean anomalies by the Kepler relation

$$\frac{\mathrm{d}l_{\mathrm{in(out)}}}{\mathrm{d}f_{\mathrm{in(out)}}} = \frac{1}{\sqrt{1-e_{\mathrm{in(out)}}^2}} \left[\frac{r_{\mathrm{in(out)}}}{a_{\mathrm{in(out)}}}\right]^2, \tag{1.6}$$

and where the instantaneous separations are given by

$$r_{\mathrm{in(out)}} = \frac{a_{\mathrm{in(out)}}(1-e_{\mathrm{in(out)}}^2)}{1+e_{\mathrm{in(out)}}\cos(f_{\mathrm{in(out)}})}. \tag{1.7}$$

Table 1.1. Common variables which are used throughout this work. Variables associated with the inner and outer orbit are denoted by subscripts in and out, respectively.

Symbol	Description	Formula
m_1	Primary mass of the inner binary	
m_2	Secondary mass of the inner binary	
m_3	Mass of the tertiary companion	
$m_{\rm in}$	Total mass of the inner binary	$m_{\rm in} = m_1 + m_2$
$m_{\rm out}$	Total mass of the outer binary	$m_{\rm out} = m_{\rm in} + m_3$
$\mu_{\rm in}$	Reduced mass of the inner binary	$\mu_{\rm in} = m_1 m_2 / m_{\rm in}$
$\mu_{\rm out}$	Reduced mass of the outer binary	$\mu_{\rm out} = m_{\rm in} m_3 / m_{\rm out}$
$a_{\rm in(out)}$	Semi-major axis of the inner (outer) orbit	
$e_{\rm in(out)}$	Eccentricity of the inner (outer) orbit	
$P_{\rm in(out)}$	Inner (outer) orbital period	$P_{\rm in(out)} = 2\pi[a^3_{\rm in(out)}/(G m_{\rm in(out)})]^{1/2}$
$\mathbf{r}_{\rm in}$	Relative position vector between the inner binary masses	
$\mathbf{r}_{\rm out}$	Relative position vector between the inner binary centre of mass and tertiary companion	
$\mathbf{e}_{\rm in(out)}$	Eccentricity vector of the inner (outer) orbit	$\mathbf{e}_{\rm in(out)} = e_{\rm in(out)} \hat{\mathbf{e}}_{\rm in(out)}$
$\mathbf{j}_{\rm in(out)}$	Dimensionless angular momentum vector of the inner (outer) orbit	$\mathbf{j}_{\rm in(out)} = [1 - e^2_{\rm in(out)}]^{1/2} \hat{\mathbf{j}}_{\rm in(out)}$
$L_{\rm in(out)}$	Circular angular momentum of the inner (outer) orbit	$L_{\rm in(out)} = \mu_{\rm in(out)} [G m_{\rm in(out)} a_{\rm in(out)}]^{1/2}$
$\mathbf{G}_{\rm in(out)}$	Angular momentum vector of the inner (outer) orbit	$\mathbf{G}_{\rm in(out)} = \mu_{\rm in(out)} \mathbf{r} \times \dot{\mathbf{r}} = L_{\rm in(out)} \mathbf{j}_{\rm in(out)}$
$H_{\rm in(out)}$	z-component of the inner (outer) orbital angular momentum in the invariable frame	$H_{\rm in(out)} = G_{\rm in(out)} \cos(i_{\rm in(out)})$

1.1.1 Hamiltonian model

Writing the orbital configuration of the inner and outer orbit in terms of the Delaunay variables w.r.t. the invariable plane, we can simply derive the equations of motion from the Hamiltonian $\mathcal{H}$ of the triple using the canonical relations

$$\frac{\mathrm{d}G_{\mathrm{in(out)}}}{\mathrm{d}t} = -\frac{\partial \mathcal{H}}{\partial g_{\mathrm{in(out)}}}, \qquad \frac{\mathrm{d}g_{\mathrm{in(out)}}}{\mathrm{d}t} = \frac{\partial \mathcal{H}}{\partial G_{\mathrm{in(out)}}}, \tag{1.8}$$

$$\frac{\mathrm{d}L_{\mathrm{in(out)}}}{\mathrm{d}t} = -\frac{\partial \mathcal{H}}{\partial l_{\mathrm{in(out)}}}, \qquad \frac{\mathrm{d}l_{\mathrm{in(out)}}}{\mathrm{d}t} = \frac{\partial \mathcal{H}}{\partial L_{\mathrm{in(out)}}}, \tag{1.9}$$

$$\frac{\mathrm{d}H_{\mathrm{in(out)}}}{\mathrm{d}t} = -\frac{\partial \mathcal{H}}{\partial h_{\mathrm{in(out)}}}, \qquad \frac{\mathrm{d}h_{\mathrm{in(out)}}}{\mathrm{d}t} = \frac{\partial \mathcal{H}}{\partial H_{\mathrm{in(out)}}} \tag{1.10}$$

For a hierarchical triple with a small semi-major axis ratio $\alpha \equiv a_{\mathrm{in}}/a_{\mathrm{out}} \ll 1$, the complete Hamiltonian of the three-body system can be expanded as a power series in α (Harrington, 1968)

$$\begin{aligned}\mathcal{H} =& \mathcal{H}_{\mathrm{in}} + \mathcal{H}_{\mathrm{out}} + \Phi \\ =& -\frac{Gm_1m_2}{2a_{\mathrm{in}}} - \frac{Gm_3m_{\mathrm{in}}}{2a_{\mathrm{out}}} - \frac{G}{a_{\mathrm{out}}}\sum_{l=2}^{\infty}\left(\frac{a_{\mathrm{in}}}{a_{\mathrm{out}}}\right)^l M_l \left(\frac{r_{\mathrm{in}}}{a_{\mathrm{in}}}\right)^l \left(\frac{a_{\mathrm{out}}}{r_{\mathrm{out}}}\right)^{l+1} P_l[\cos(\vartheta)],\end{aligned} \tag{1.11}$$

where $\mathcal{H}_{\mathrm{in}}$ and $\mathcal{H}_{\mathrm{out}}$ are the Kelperian Hamiltonians of the inner and outer orbit, respectively, and Φ describes the interaction between them. $P_l(\cos\vartheta)$ are Legendre polynomials with ϑ being the angle between $\mathbf{r}_{\mathrm{in}}$ and $\mathbf{r}_{\mathrm{out}}$, and

$$M_l = m_1m_2m_3\frac{m_1^{l-1} - (-m_2)^{l-1}}{m_{\mathrm{in}}^l}. \tag{1.12}$$

For a small $\alpha \ll 1$, the sum over l will be dominated by its lowest orders. In previous work, the three-body dynamics has been extensively studied to the quadrupole ($l = 2$) (e.g., Kozai, 1962; Lidov, 1962), octupole ($l = 3$) (e.g., Ford et al., 2000; Blaes et al., 2002; Naoz et al., 2013a; Liu et al., 2015; Antognini, 2015), and hexadecapole order ($l = 4$) (Will, 2017). Here, we consider only the lowest two orders by truncating the interaction term at $l = 3$, i.e., by writing $\Phi \approx \Phi_{\mathrm{quad}} + \Phi_{\mathrm{oct}}$ where (Liu et al., 2015)

$$\Phi_{\mathrm{quad}} = -\frac{Gm_1m_2m_3}{m_{\mathrm{in}}r_{\mathrm{out}}}\left[\frac{3}{2}\frac{(\mathbf{r}_{\mathrm{in}}\cdot\mathbf{r}_{\mathrm{out}})^2}{r_{\mathrm{out}}^4} - \frac{r_{\mathrm{in}}^2}{2r_{\mathrm{out}}^2}\right], \tag{1.13}$$

and

$$\Phi_{\mathrm{oct}} = -\frac{Gm_1m_2m_3(m_1-m_2)}{m_{\mathrm{in}}^2r_{\mathrm{out}}}\left[\frac{5}{2}\frac{(\mathbf{r}_{\mathrm{in}}\cdot\mathbf{r}_{\mathrm{out}})^3}{r_{\mathrm{out}}^6} - \frac{3}{2}\frac{r_{\mathrm{in}}^2(\mathbf{r}_{\mathrm{in}}\cdot\mathbf{r}_{\mathrm{out}})}{r_{\mathrm{out}}^4}\right]. \tag{1.14}$$

Furthermore, a small $\alpha \ll 1$ generally implies that the interaction term is weak so that the inner and outer orbits only change over long secular timescales (i.e., timescales which are much longer than the orbital periods). To determine the long-term evolution of the triple it is therefore, sufficient to consider the so-called double-averaged Hamiltonian for which we eliminate the short-timescale dependencies on $l_{\rm in(out)}$ by averaging Eq. 1.11 over the inner and outer orbital period.

The quadrupole contribution to the double-averaged Hamiltonian is given by (Naoz et al., 2013a)

$$\begin{aligned}\langle\Phi_{\rm quad}\rangle = -\frac{C_2}{8}\Bigg\{&[1+3\cos(2i_{\rm out})]\left[(2+3e_{\rm in}^2)(1+3\cos(2i_{\rm in}))+30e_{\rm in}^2\cos(2g_{\rm in})\sin^2(i_{\rm in})\right]\\&+3\cos(2\Delta h)\left[10e_{\rm in}^2\cos(2g_{\rm in})(3+\cos(2i_{\rm in}))+4(2+3e_{\rm in}^2)\sin^2(i_{\rm in})\right]\sin^2(i_{\rm out})\\&+12(2+3e_{\rm in}^2-5e_{\rm in}^2\cos(2g_{\rm in}))\cos(2\Delta h)\sin(2i_{\rm in})\sin(2i_{\rm out})\\&+120e_{\rm in}^2\sin(i_{\rm in})\sin(2i_{\rm out})\sin(2g_{\rm in})\sin(\Delta h)\\&-120e_{\rm in}^2\cos(i_{\rm in})\sin^2(i_{\rm out})\sin(2g_{\rm in})\sin(2\Delta h)\Bigg\},\end{aligned} \tag{1.15}$$

where the longitudes of the ascending nodes of the inner and outer orbit only enter the equation in terms of their difference $\Delta h = h_1 - h_2$ and the prefactor C_2 is given by

$$C_2 = \frac{G^2}{16}\frac{m_{\rm in}^7}{m_{\rm out}^3}\frac{m_3^7}{(m_1m_2)^3}\frac{L_{\rm in}^4}{L_{\rm out}^3G_{\rm out}^3}. \tag{1.16}$$

Using the canonical relations Eqs. (1.8) – (1.10) we get for the quadrupole equations of motion (Naoz et al., 2013a)

$$\left.\frac{{\rm d}G_{\rm in}}{{\rm d}t}\right|_{\rm quad} = -\frac{\partial\langle\Phi_{\rm quad}\rangle}{\partial g_{\rm in}} = -30C_2e_{\rm in}^2\sin^2(i_{\rm tot})\sin(2g_{\rm in}), \tag{1.17}$$

$$\left.\frac{{\rm d}H_{\rm in}}{{\rm d}t}\right|_{\rm quad} = -\frac{\partial\langle\Phi_{\rm quad}\rangle}{\partial h_{\rm in}} = -30C_2e_{\rm in}^2\sin(i_{\rm tot})\sin(i_{\rm out})\sin(2g_{\rm in}). \tag{1.18}$$

From Eq. (1.3) we have $H_{\rm in} + H_{\rm out} = G_{\rm tot} = {\rm const}$. For the outer orbit it follows that

$$\left.\frac{{\rm d}H_{\rm out}}{{\rm d}t}\right|_{\rm quad} = -\left.\frac{{\rm d}H_{\rm in}}{{\rm d}t}\right|_{\rm quad}. \tag{1.19}$$

Moreover, $G_{\rm out}$ and $L_{\rm in(out)}$ remain constant in the secular approximation because $\langle\Phi_{\rm quad}\rangle$ is independent of $g_{\rm out}$ and $l_{\rm in(out)}$, respectively. As a consequence of the conservation of $L_{\rm in(out)}$, the semi-major axes do not change and hence, the orbital energies of the inner and outer orbit are separately conserved.

The time evolution of the orbital angles of the inner orbit is given by (Naoz et al., 2013a)

$$\left.\frac{\mathrm{d}g_{\rm in}}{\mathrm{d}t}\right|_{\rm quad} = \frac{\partial\langle\Phi_{\rm quad}\rangle}{\partial G_{\rm in}} = 6C_2\Bigg\{\frac{1}{G_{\rm in}}\left[4\cos^2(i_{\rm tot}) + (5\cos(2g_{\rm in})-1)(1-e_{\rm in}^2-\cos^2(i_{\rm tot}))\right] + \frac{\cos(i_{\rm tot})}{G_{\rm out}}\left[2+e_{\rm in}^2(3-5\cos(2g_{\rm in}))\right]\Bigg\}, \tag{1.20}$$

$$\left.\frac{\mathrm{d}h_{\rm in}}{\mathrm{d}t}\right|_{\rm quad} = \frac{\partial\langle\Phi_{\rm quad}\rangle}{\partial H_{\rm in}} = -\frac{3C_2}{G_{\rm in}\sin(i_{\rm in})}\left[2+3e_{\rm in}^2-5e_{\rm in}^2\cos(2g_{\rm in})\right]\sin(2i_{\rm tot}). \tag{1.21}$$

Considering the outer orbit, the construction of the total angular momentum vector by Eq. (1.3) implies that $\Delta h = h_1 - h_2 = \pi$ and its conservation preserves this relation at all times, which is oftentimes referred to as "elimination of the nodes". Hence, we have for the longitude of the ascending node of the outer orbit

$$\left.\frac{\mathrm{d}h_{\rm out}}{\mathrm{d}t}\right|_{\rm quad} = \left.\frac{\mathrm{d}h_{\rm in}}{\mathrm{d}t}\right|_{\rm quad}, \tag{1.22}$$

while Eq. (1.8) yields for the argument of its periapsis (Naoz et al., 2013a)

$$\left.\frac{\mathrm{d}g_{\rm out}}{\mathrm{d}t}\right|_{\rm quad} = \frac{\partial\langle\Phi_{\rm quad}\rangle}{\partial G_{\rm in}} = 3C_2\Bigg\{\frac{2\cos(i_{\rm tot})}{G_{\rm in}}\left[2+e_{\rm in}^2(3-5\cos(2g_{\rm in}))\right] + \frac{1}{G_{\rm out}}\left[4+6e_{\rm in}^2+(5\cos^2(i_{\rm tot})-3)(2+e_{\rm in}^2[3-5\cos(2g_{\rm in})])\right]\Bigg\}. \tag{1.23}$$

In order to include the next-order octupole terms it is useful to simplify the double-averaged Hamiltonian by eliminating the nodes (given above) by explicitly substituting $\Delta h \to \pi$, i.e.,

$$\langle\Phi\rangle(\Delta h\to\pi) = \langle\Phi_{\rm quad}\rangle(\Delta h\to\pi) + \langle\Phi_{\rm oct}\rangle(\Delta h\to\pi), \tag{1.24}$$

where the node eliminated contributions to the Hamiltonian are (Naoz et al., 2013a)

$$\langle\Phi_{\rm quad}\rangle(\Delta h\to\pi) = -C_2\left\{\left(2+3e_{\rm in}^2\right)\left(3\cos^2(i_{\rm tot})-1\right)+15e_{\rm in}^2\sin^2(i_{\rm tot})\cos(2g_{\rm in})\right\}, \tag{1.25}$$

$$\langle\Phi_{\rm oct}\rangle(\Delta h\to\pi) = -C_3 e_{\rm in}e_{\rm out}\left\{A\cos(\phi)+10\cos(i_{\rm tot})\sin^2(i_{\rm tot})(1-e_{\rm in}^2)\sin(g_{\rm in})\sin(g_{\rm out})\right\}, \tag{1.26}$$

with

$$C_3 = -\frac{15}{16}\frac{G^2}{4}\frac{m_{\rm in}^9}{m_{\rm out}^4}\frac{m_3^9(m_1-m_2)}{(m_1m_2)^5}\frac{L_{\rm in}^6}{L_{\rm out}^3 G_{\rm out}^5}, \tag{1.27}$$

$$A = 4 + 3e_{\rm in}^2 - \frac{5}{2}B\sin^2(i_{\rm tot}), \tag{1.28}$$

$$B = 2 + 5e_{\rm in}^2 - 7e_{\rm in}^2\cos(2g_{\rm in}), \tag{1.29}$$

$$\cos(\phi) = -\cos(g_{\rm in})\cos(g_{\rm out}) - \cos(g_{\rm tot})\sin(g_{\rm in})\sin(g_{\rm out}). \tag{1.30}$$

Using the canonical relations we thus get for the evolution of orbital angular momenta (Naoz et al., 2013a)

$$\begin{aligned}\frac{{\rm d}G_{\rm in}}{{\rm d}t} &= -30C_2e_{\rm in}^2\sin(2g_{\rm in})\sin^2(i_{\rm tot}) + C_3e_{\rm in}e_{\rm out}\Big\{-35e_{\rm in}^2\sin^2(i_{\rm tot})\sin(g_{\rm tot})\cos(\phi)\\ &\quad + A\left[\sin(g_{\rm in})\cos(g_{\rm out}) - \cos(i_{\rm tot})\cos(g_{\rm in})\sin(g_{\rm out})\right]\\ &\quad + 10\cos(i_{\rm tot})\sin^2(i_{\rm tot})(1-e_{\rm in}^2)\cos(g_{\rm in})\sin(g_{\rm out})\Big\},\end{aligned} \tag{1.31}$$

$$\begin{aligned}\frac{{\rm d}G_{\rm out}}{{\rm d}t} &= C_3e_{\rm in}e_{\rm out}\Big\{A\left[\cos(g_{\rm in})\sin(g_{\rm out}) - \cos(i_{\rm tot})\sin(g_{\rm in})\cos(g_{\rm out})\right]\\ &\quad + 10\cos(i_{\rm tot})\sin^2(i_{\rm tot})(1-e_{\rm in}^2)\sin(g_{\rm in})\cos(g_{\rm out})\Big\},\end{aligned} \tag{1.32}$$

while the evolution of their z-components follow from

$$\frac{{\rm d}H_{\rm in}}{{\rm d}t} = \frac{G_{\rm in}}{G_{\rm tot}}\frac{{\rm d}G_{\rm in}}{{\rm d}t} - \frac{G_{\rm out}}{G_{\rm tot}}\frac{{\rm d}G_{\rm out}}{{\rm d}t}, \tag{1.33}$$

$$\frac{{\rm d}H_{\rm out}}{{\rm d}t} = -\frac{{\rm d}H_{\rm in}}{{\rm d}t} = \frac{G_{\rm out}}{G_{\rm tot}}\frac{{\rm d}G_{\rm out}}{{\rm d}t} - \frac{G_{\rm in}}{G_{\rm tot}}\frac{{\rm d}G_{\rm in}}{{\rm d}t}. \tag{1.34}$$

Meanwhile, the arguments of periapse of the inner and outer orbits evolve as (Naoz et al., 2013a;

Liu et al., 2015)

$$\begin{aligned}
\frac{\mathrm{d}g_{\rm in}}{\mathrm{d}t} &= 6C_2\Bigg\{\frac{1}{G_{\rm in}}\Big[4\cos^2(i_{\rm tot})+(5\cos(2g_{\rm in})-1)(1-e_{\rm in}^2-\cos^2(i_{\rm tot}))\Big]\\
&+\frac{\cos(i_{\rm tot})}{G_{\rm out}}\Big[2+e_{\rm in}^2(3-5\cos(2g_{\rm in}))\Big]\Bigg\}\\
&-C_3e_{\rm out}\Bigg\{e_{\rm in}\left(\frac{1}{G_{\rm out}}+\frac{\cos(i_{\rm tot})}{G_{\rm in}}\right)\\
&\times\Bigg[\sin(g_{\rm in})\sin(g_{\rm out})\Big[10(3\cos^2(i_{\rm tot})-1)(1-e_{\rm in}^2)+A\Big]-5B\cos(i_{\rm tot})\cos(\phi)\Bigg]\\
&-\frac{1-e_{\rm in}^2}{e_{\rm in}G_{\rm in}}\Big[10\sin(g_{\rm in})\sin(g_{\rm out})\cos(i_{\rm tot})\sin^2(i_{\rm tot})(1-3e_{\rm in}^2)\\
&+\cos(\phi)(3A-10\cos^2(i_{\rm tot})+2)\Big]\Bigg\},
\end{aligned}\tag{1.35}$$

$$\begin{aligned}
\frac{\mathrm{d}g_{\rm out}}{\mathrm{d}t} &= 3C_2\Bigg\{\frac{2\cos(i_{\rm tot})}{G_{\rm in}}\Big[2+e_{\rm in}(3-5\cos 2g_{\rm in})\Big]\\
&+\frac{1}{G_{\rm out}}\Bigg[4+6e_{\rm in}^2+(5\cos^2(i_{\rm tot})-3)\Big[2+e_{\rm in}^2(3-5\cos 2g_{\rm in})\Big]\Bigg]\Bigg\}\\
&+C_3e_{\rm in}\Bigg\{\sin(g_{\rm in})\sin(g_{\rm out})\Bigg[\frac{4e_{\rm out}^2+1}{e_{\rm out}G_{\rm out}}10\cos(i_{\rm tot})\sin^2(i_{\rm tot})(1-e_{\rm in}^2)\\
&-e_{\rm out}\left(\frac{1}{G_{\rm in}}+\frac{\cos(i_{\rm tot})}{G_{\rm out}}\right)\Big[A+10(3\cos^2(i_{\rm tot})-1)(1-e_{\rm in}^2)\Big]\Bigg]\\
&+\cos(\phi)\Bigg[5B\cos(i_{\rm tot})e_{\rm out}\left(\frac{1}{G_{\rm in}}+\frac{\cos(i_{\rm tot})}{G_{\rm out}}\right)+\frac{4e_{\rm out}^2+1}{e_{\rm out}G_{\rm out}}A\Bigg]\Bigg\}
\end{aligned}\tag{1.36}$$

The evolution of the longitude of the ascending node of the inner orbit is given by (Naoz et al., 2013a; Liu et al., 2015)

$$\begin{aligned}
\frac{\mathrm{d}h_{\rm in}}{\mathrm{d}t} &= -\frac{3C_2}{G_{\rm in}\sin(i_{\rm in})}\left[2+3e_{\rm in}^2-5e_{\rm in}^2\cos(2g_{\rm in})\right]\sin(2i_{\rm tot})\\
&-C_3e_{\rm in}e_{\rm out}\Bigg[5B\cos(i_{\rm tot})\cos(\phi)-A\sin(g_{\rm in})\sin(g_{\rm out})\\
&+10(1-3\cos^2(i_{\rm tot}))(1-e_{\rm in}^2)\sin(g_{\rm in})\sin(g_{\rm out})\Bigg]\frac{\sin(i_{\rm tot})}{G_{\rm in}\sin(i_{\rm in})},
\end{aligned}\tag{1.37}$$

and the longitude of the ascending node of the outer orbit evolves equally $\mathrm{d}h_{\rm out}/\mathrm{d}t=\mathrm{d}h_{\rm in}/\mathrm{d}t$ due to the conservation of the total angular momentum vector (as discussed above).

Finally, it is instructive also to consider the evolution of the orbital eccentricities and inclinations of the orbital axes w.r.t. to the total angular momentum vector which can be calculated from the Delaunay elements as (Naoz et al., 2013a)

$$\frac{\mathrm{d}e_{\mathrm{in(out)}}}{\mathrm{d}t} = -\frac{\partial e_{\mathrm{in(out)}}}{\partial G_{\mathrm{in(out)}}}\frac{\partial \mathcal{H}}{\partial g_{\mathrm{in(out)}}}, \tag{1.38}$$

$$\frac{\mathrm{d}i_{\mathrm{in(out)}}}{\mathrm{d}t} = \frac{1}{G_{\mathrm{in(out)}}}\left[\frac{1}{\tan(i_{\mathrm{in(out)}})}\frac{\mathrm{d}G_{\mathrm{in(out)}}}{\mathrm{d}t} - \frac{1}{\sin(i_{\mathrm{in(out)}})}\frac{\mathrm{d}H_{\mathrm{in(out)}}}{\mathrm{d}t}\right], \tag{1.39}$$

so that the evolution of the relative inclination is given by $\mathrm{d}i_{\mathrm{tot}}/\mathrm{d}t = \mathrm{d}i_{\mathrm{in}}/\mathrm{d}t + \mathrm{d}i_{\mathrm{out}}/\mathrm{d}t$.

1.1.2 Quadrupole dynamics

The secular dynamics of a hierarchical triple simplifies if the octupole terms are negligible. By inspection of Eqs. (1.26) and (1.27) we see that this is the case when the two inner binary components have comparable masses ($m_1 \approx m_2$) or when the outer orbit is circular ($e_{\mathrm{out}} \approx 0$), i.e., when the potential of the outer orbit is axisymmetric.

Neglecting the octupole contribution the magnitude of the outer orbital angular momentum is constant ($G_{\mathrm{out}} = \mathrm{const.}$) because then $\partial\mathcal{H}/\partial g_{\mathrm{out}} = 0$. By Eq. (1.38) this also implies that the eccentricity of the outer orbit remains constant as $\mathrm{d}e_{\mathrm{out}}/\mathrm{d}t = 0$. However, the eccentricity of the inner orbit and the relative inclination by Eqs. (1.38) and (1.39) evolve as (Naoz et al., 2013a; Liu et al., 2015)

$$\frac{\mathrm{d}e_{\mathrm{in}}}{\mathrm{d}t} = 30C_2\frac{1-e_{\mathrm{in}}^2}{G_{\mathrm{in}}}e_{\mathrm{in}}\sin^2(i_{\mathrm{tot}})\sin(2g_{\mathrm{in}}), \tag{1.40}$$

$$\frac{\mathrm{d}i_{\mathrm{tot}}}{\mathrm{d}t} = \frac{\mathrm{d}i_{\mathrm{in}}}{\mathrm{d}t} + \frac{\mathrm{d}i_{\mathrm{out}}}{\mathrm{d}t}, \tag{1.41}$$

where

$$\frac{\mathrm{d}i_{\mathrm{in}}}{\mathrm{d}t} = -\frac{15e_{\mathrm{in}}^2}{16t_{\mathrm{LK}}\sqrt{1-e_{\mathrm{in}}^2}}\sin(2i_{\mathrm{tot}})\sin(2g_{\mathrm{in}}), \tag{1.42}$$

$$\frac{\mathrm{d}i_{\mathrm{out}}}{\mathrm{d}t} = -\frac{15e_{\mathrm{in}}^2 L_{\mathrm{in}}}{8t_{\mathrm{LK}}\sqrt{1-e_{\mathrm{out}}^2}L_{\mathrm{out}}}\sin(2i_{\mathrm{tot}})\sin(2g_{\mathrm{in}}), \tag{1.43}$$

and

$$t_{\mathrm{LK}} = \left(\frac{a_{\mathrm{in}}^3}{Gm_{\mathrm{in}}}\right)^{1/2}\left(\frac{m_{\mathrm{in}}}{m_3}\right)\left(\frac{a_{\mathrm{out}}}{a_{\mathrm{in}}}\right)^3\left(1-e_{\mathrm{out}}^2\right)^{3/2}. \tag{1.44}$$

Thus, the evolution of e_{in} and i_{tot} admit well-defined extrema which occur at $g_{\mathrm{in}} = n\pi/2$ ($n \in \mathbb{Z}$).

As an example, we show in Fig. 1.4 the numerical integration of fiducial systems with a circular outer orbit. It can be seen that the eccentricity of the inner orbit and the relative inclination can undergo large-amplitude oscillations. The oscillations are particularly large if the orbits are initialised highly inclined to one another, i.e., close to $\cos^2(i_{\rm tot}) = 0$. The trajectories shown in Fig. 1.4 are initialised at $g_{\rm in} = 0$ and are so-called circulating modes, i.e., the angle argument of the inner periapse moves over the entire circle where $e_{\rm in}$ and $\cos^2(i_{\rm tot})$ attain their maxima at $g_{\rm in} = \pi/2$ and $3\pi/2$ and minima at $g_{\rm in} = 0$ and π.

Fig. 1.5 and 1.6 show that different classes of trajectories are possible if they are initialised at a non-zero $g_{\rm in}$. In that case, librating modes are possible which oscillate around $\pi/2$ (or integer-multiples thereof) where $e_{\rm in}$ and $\cos^2(i_{\rm tot})$ attain their extrema.

Whether a given system is circulating or librating can be found by checking if Eq. (1.25) admits a physical solution at $g_{\rm in} = 0$. If this is not the case, i.e., if Eq. (1.25) can only be solved for a negative, unphysical eccentricity of the inner binary, then the trajectory must be librating as it could never reach $g_{\rm in} = 0$. In turn, the trajectory is circulating if the solution is physical. In order to identify the limiting trajectory which separates both types of modes and which has $e_{\rm in}(g_{\rm in} = 0) = 0$ we rewrite Eq. (1.4) in terms of the initial variables with subscript 0 as (Hamers, 2021)

$$\cos(i_{\rm tot}) = \frac{\Theta}{\sqrt{1-e_{\rm in}^2}} - \gamma\sqrt{1-e_{\rm in}^2}, \tag{1.45}$$

where

$$\gamma = \frac{L_{\rm in}}{2G_{\rm out}}, \qquad \Theta = \sqrt{1-e_{\rm in,0}^2}\cos(i_{\rm tot,0}) + \gamma(1-e_{\rm in,0}^2). \tag{1.46}$$

Then we observe that Eq. (1.25) simplifies to

$$\frac{\langle\Phi_{\rm quad}\rangle}{C_2} = 6(\Theta-\gamma)^2 - 2. \tag{1.47}$$

Thus, it is instructive to introduce the quantity

$$\varepsilon = \frac{1}{12}\left[\frac{\langle\Phi_{\rm quad}\rangle}{C_2} - 6(\Theta-\gamma)^2 + 2\right], \tag{1.48}$$

which is positive ($\varepsilon > 0$) if the trajectory circulates, and negative ($\varepsilon < 0$) if the trajectory librates. The prefactor $1/12$ is chosen to agree with the original derivation of Lidov (1962).

The maximum and minimum eccentricity of the inner orbit can be found by substituting the appropriate $g_{\rm in}$ and $\cos(i_{\rm tot})$ described by Eq. (1.45) to Eq. (1.25) and solving for $e_{\rm in}$. This way

Hamers (2021) finds for the maximum eccentricity on librating as well as circulating modes

$$j^2_{\rm in,min} = \frac{1}{12\gamma^2} \times \begin{cases} 3+5\gamma^2+8\gamma\Theta-2\sqrt{A}\sin\left(\frac{\phi}{3}+\frac{\pi}{6}\right), & \text{if } A^3+K_2^2 \geq 0; \\ 3+5\gamma^2+8\gamma\Theta-\frac{A}{k_1}-k_1, & \text{if } A^3+K_2^2<0 \text{ and } K_2+\sqrt{K_2^2-A^3}<0; \\ 3+5\gamma^2+8\gamma\Theta-\frac{A}{k_2}+k_2, & \text{if } A^3+K_2^2<0 \text{ and } K_2+\sqrt{K_2^2-A^3}>0; \end{cases} \tag{1.49}$$

where

$$K_1 = 13\gamma^4-16\gamma^3\Theta+48\gamma\Theta+\gamma^2\left(-23\varepsilon+4\Theta^2-6\right)+9, \tag{1.50}$$

$$K_2 = 35\gamma^6-264\gamma^5\Theta+216\gamma\Theta-3\gamma^4\left(60\varepsilon-146\Theta^2+33\right)-16\gamma^3\Theta\left(18\varepsilon+13\Theta^2+9\right) - 9\gamma^2\left(12\varepsilon-34\Theta^2+3\right)+27, \tag{1.51}$$

$$k_1 = \left(-K_2-\sqrt{K_2^2-K_1^3}\right)^{1/3}, \tag{1.52}$$

$$k_2 = \left(K_2+\sqrt{K_2^2-K_1^3}\right)^{1/3}, \tag{1.53}$$

and with the 2-argument acrtangent function $\phi = \arctan2(\sqrt{K_1^3-K_2^2}, K_2)$. The minimum eccentricity on librating orbits ($\varepsilon < 0$) is given by (Hamers, 2021)

$$j^2_{\rm in,max} = \frac{1}{12\gamma^2}\left[3+5\gamma^2+8\gamma\Theta+2\sqrt{K_1}\sin\left(\frac{\phi}{3}-\frac{\pi}{6}\right)\right], \tag{1.54}$$

while for circulating modes ($\varepsilon > 0$) we have

$$j^2_{\rm in,max} = \frac{1}{\gamma^2}\left[1+\gamma\Theta-\sqrt{1+2\gamma\Theta-2\gamma^2+2\gamma^2\varepsilon+\gamma^2(\Theta-\gamma)^2}\right]. \tag{1.55}$$

A special case of the equations above applies to the so-called (restricted) test particle limit in which the secondary mass m_2 is set to zero. This case has been originally studied by Kozai (1962) and Lidov (1962) and provides an adequate prescription of, e.g., planets orbiting either one of the stars of a stellar binary. In that case, $\gamma = 0$ and all the angular momentum of the system is contained in the outer orbit. Eqs. (1.45) and (1.46) yield

$$\sqrt{1-e^2_{\rm in,0}}\cos\left(i_{\rm tot,0}\right) = \sqrt{1-e^2_{\rm in}}\cos\left(i_{\rm tot}\right) = \text{const.}, \tag{1.56}$$

i.e., the z-component of the specific angular momentum of the inner orbit is a constant. In order to find the maximum eccentricity the orbit of the test particle we can repeat the steps above and substitute an appropriate $g_{\rm in}$ to Eq. (1.25) and solve for $e_{\rm in}$. In particular, let us assume that the orbit is initially circular, i.e., $e_{\rm in,0} = 0$ at $g_{\rm in,0} = 0$. Then it is straightforward to evaluate

$\langle\Phi_{\rm quad}\rangle(e = e_{\rm in,0}, g_{\rm in} = g_{\rm in,0}) = \langle\Phi_{\rm quad}\rangle(e = e_{\rm in,max}, g_{\rm in} = \pi/2)$ which yields two physically possible solutions for the maximum eccentricity

$$j^2_{\rm in,min} = 1 - e^2_{\rm in,max} = \frac{5}{3}\cos^2(i_{\rm tot,0}), \tag{1.57}$$

and $e^2_{\rm in,max} = 0$ where the orbit stays circular. Since $j^2_{\rm in,min}$ must be between zero and one, Eq. (1.57) is only an applicable solution if $\cos^2(i_{\rm tot,0}) < 3/5$, i.e., $i_{\rm tot,0}$ must be within the canonical range of $39.2°$ and $140.8°$ which are referred to as Kozai angles. Thus, in the test-particle limit eccentricity oscillations of an initially circular orbit are only possible if the inclination is within the given range of angles.

If the test particle starts on a non-circular orbit $e_{\rm in,0} \neq 0$, we can solve

$$\langle\Phi_{\rm quad}\rangle(e = e_{\rm in,0}, g_{\rm in} = g_{\rm in,0}) = \langle\Phi_{\rm quad}\rangle(e = e_{\rm in,min}, g_{\rm in} = 0), \tag{1.58}$$

$$\langle\Phi_{\rm quad}\rangle(e = e_{\rm in,0}, g_{\rm in} = g_{\rm in,0}) = \langle\Phi_{\rm quad}\rangle(e = e_{\rm in,max}, g_{\rm in} = \pi/2), \tag{1.59}$$

for $e_{\rm in,min}$ and $e_{\rm in,max}$, respectively, to get (Antognini, 2015)

$$j^2_{\rm in,min} = \frac{1}{6}\left(\zeta - \sqrt{\zeta^2 - 60\Theta^2}\right) \tag{1.60}$$

for librating and circulating modes and where $\zeta = 3 + 5\Theta^2 + 2\varepsilon$. Meanwhile, the minimum eccentricity on librating trajectories ($\varepsilon < 0$) is given by

$$j^2_{\rm in,max} = \frac{1}{6}\left(\zeta + \sqrt{\zeta^2 - 60\Theta^2}\right), \tag{1.61}$$

while

$$j^2_{\rm in,max} = 1 - \varepsilon \tag{1.62}$$

on circulating trajectories.

1.1.3 Octupole dynamics

The octupole terms can become important for the dynamics of a triple if the inner binary masses significantly differ from each other and if the outer orbit is eccentric. This applies to a large number of planetary and stellar orbits which are observed to be eccentric (e.g., Naoz et al., 2011; Moe & Di Stefano, 2017). The dynamical behaviour of a triple due to the octupole terms becomes more complex and qualitatively different from the quadrupole approximation. In general, it is chaotic and does no longer exhibit well-defined extrema of the eccentricity evolution. Here,

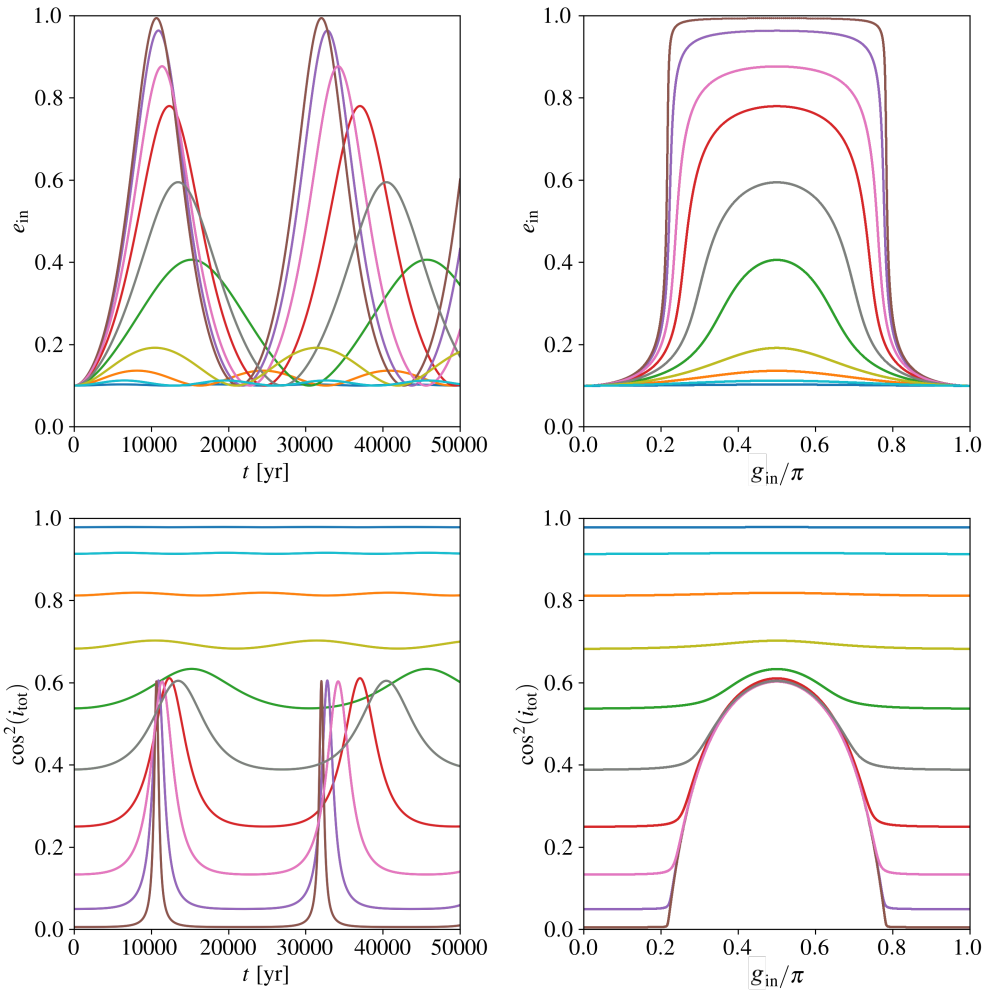

Figure 1.4. Quadrupole-order oscillations of the inner orbital eccentricity (upper panels) and relative inclination (lower panels) as functions of time (left panels) and of inner argument of the periapse (right panels). The triples have individual masses $m_1 = m_2 = 1\,\mathrm{M}_\odot$ and $m_3 = 10\,\mathrm{M}_\odot$, semi-major axes $a_{\rm in,0} = 10\,\mathrm{AU}$ and $a_{\rm out,0} = 200\,\mathrm{AU}$, and initial eccentricities $e_{\rm in,0} = 0.1$ and $e_{\rm out,0} = 0$. Furthermore, the systems are initialised at $g_{\rm in,0} = 0$ and we vary for each color the initial relative inclination between $\cos^2(i_{\rm tot,0}) = 0$ and 1, which can be read off the lower left panel at $t = 0\,\mathrm{yr}$. The triple dynamics is numerically integrated with an explicit Runge-Kutta method of order 5(4) (Dormand & Prince, 1978).

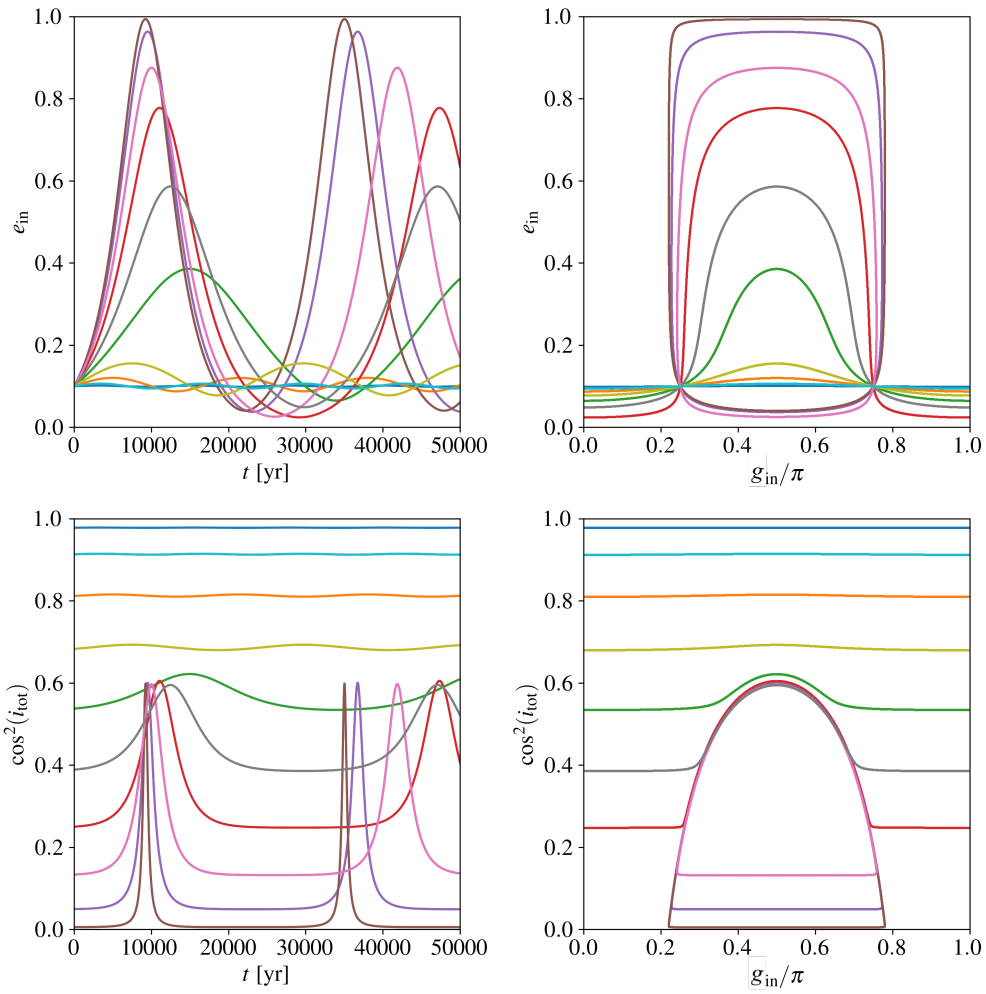

Figure 1.5. Same as Fig. 1.4 but initialised at $g_{\rm in,0} = \pi/4$.

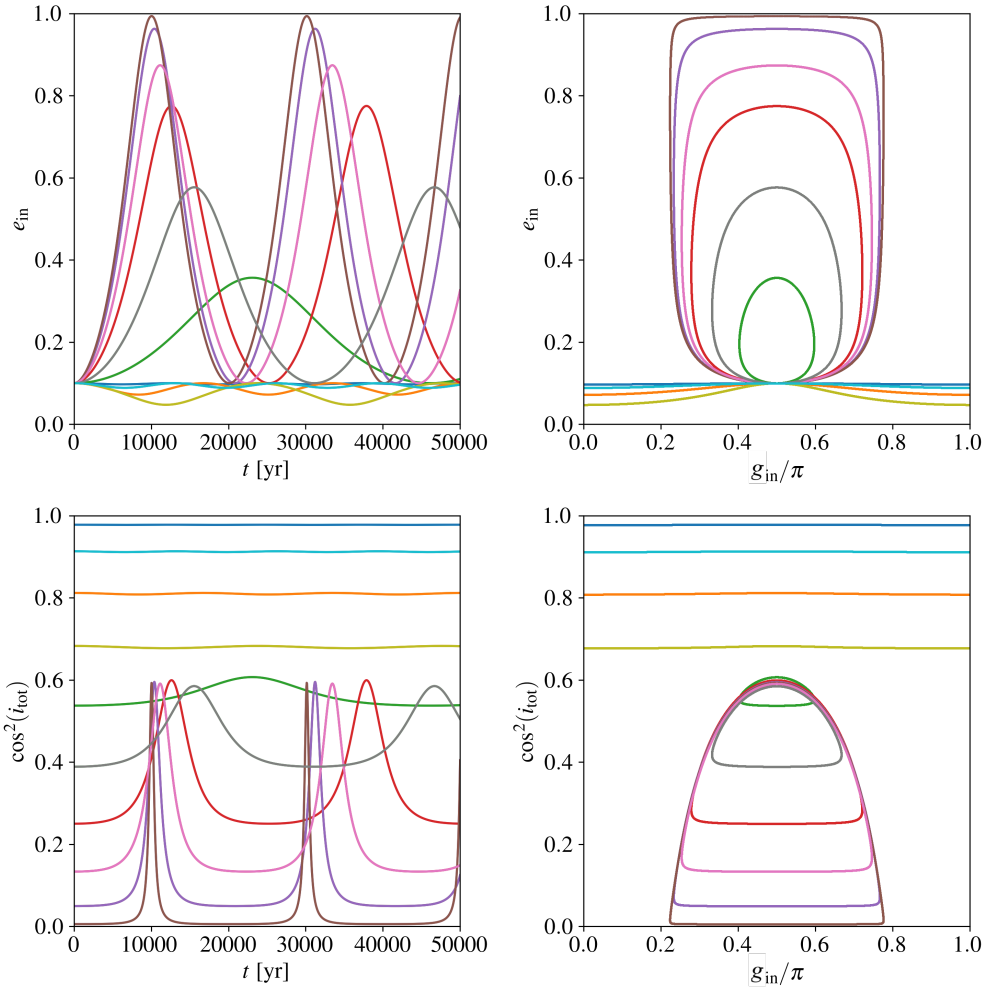

Figure 1.6. Same as Fig. 1.4 but initialised at $g_{\rm in,0} = \pi/2$.

we focus on two key properties of the octupole dynamics which are important for massive stellar triple evolution and refer the reader to Ford et al. (2000); Lithwick & Naoz (2011); Naoz et al. (2013a); Antognini (2015); Will (2017) for a more detailed analysis.

Firstly, the octupole terms can cause much higher eccentricity values of the inner orbit than in the quadrupole approximation. This is demonstrated in Fig. 1.7 where we compare the dynamical evolution of an exemplary stellar-mass triple due to the quadrupole terms (left column) with the more general case where also the octupole terms are taken into account (right column). We can see that the former evolution admits eccentricities $1 - e_{\rm in} \sim \mathcal{O}(10^{-3})$, whereas in the latter case it can be as large as $1 - e_{\rm in} \sim \mathcal{O}(10^{-8})$. These high-eccentricity excursions are accompanied by orbital flips where the relative inclination changes from prograde to retrograde (and vice versa) (Naoz et al., 2011, 2013a).

Secondly, the octupole terms tap a larger parameter space (compared to the quadrupole approximation) at which significant LK oscillations can occur. In Fig. 1.8 we recover results from Liu et al. (2015) for a stellar-mass triple and show the maximum inner eccentricity $e_{\rm in,max}$ which an exemplary triple attains as a function of the initial relative inclination $i_{\rm tot,0}$. If only quadrupole terms are taken into account, the largest eccentricities are achieved if the orbits are initialised nearly perpendicular to each other, i.e., $\cos(i_{\rm tot,0}) \approx 0$. Note that if we were to consider the test-particle case with an initially circular inner orbit ($e_{\rm in,0} = 0$) as done at the end of Section 1.1.2 Eq. (1.57) implies that the inner eccentricity gets the largest if the orbits are initialised strictly perpendicular to each other, i.e., $\cos(i_{\rm tot,0}) = 0$. Dropping the assumption of a test particle but allowing for a non-negligible mass m_2 (but with $e_{\rm in,0} = 0$) Liu et al. (2015) find that the tertiary companion induces the largest inner eccentricity if $\cos(i_{\rm tot,0}) = -\gamma$ (which reduces to the test particle result if $\gamma = 0$). We can see that this analytic result (dashed vertical line in Fig. 1.8) agrees well with the location of the maximum of $e_{\rm in,max}$ from the numerical integration (of the triple which is initialised on a nearly circular inner orbit $e_{\rm in,0} = 0.001$, see Figure caption).

Whereas in the quadrupole approximation large inner eccentricities are only achieved within a narrow window around $\cos(i_{\rm tot,0}) \approx 0$, Fig. 1.8 shows that the eccentricity can take extreme values for a much wider range of initial relative inclinations if the octupole terms are included. For this particular triple, we can see that it is the case if $|\cos(i_{\rm tot,0})| \lesssim 0.7$. This is in particular important for a realistic population of massive stellar triples which we will consider in the following chapter. For those we will assume that the initial relative inclination is drawn from an isotropic probability density function (Section 2.2). Thus, including the octupole terms increases the fraction of triples that undergo significant LK oscillations.

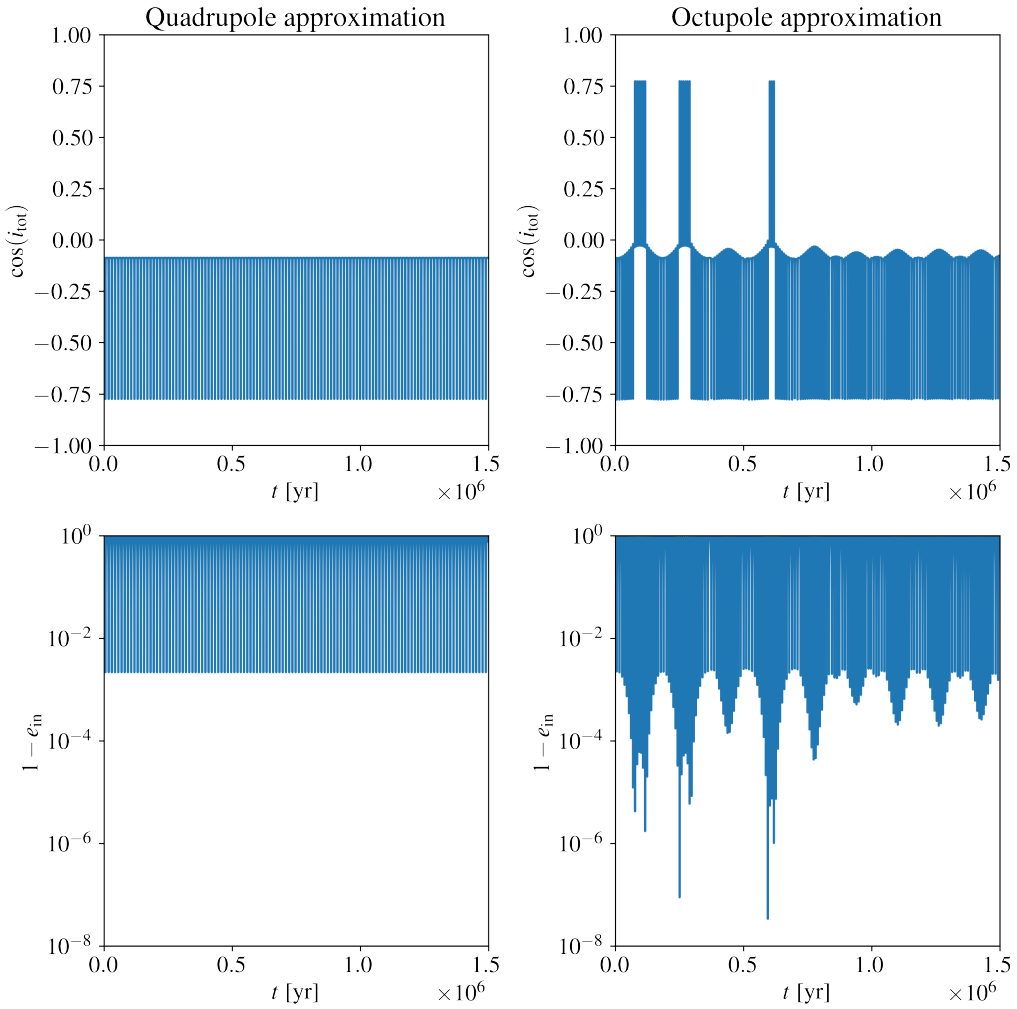

Figure 1.7. Exemplary triple evolution. The left column shows the evolution of the relative inclination and inner eccentricity if only quadrupole terms are included. The right columns shows the evolution if also the octupole terms are included. The triple is initialised with masses $m_1 = 10\,\mathrm{M}_\odot$, $m_2 = 8\,\mathrm{M}_\odot$, and $m_3 = 32\,\mathrm{M}_\odot$, eccentricities $e_{\rm in,0} = 0.01$ and $e_{\rm out,0} = 0.7$, semi-major axes $a_{\rm in,0} = 10\,\mathrm{AU}$ and $a_{\rm out,0} = 200\,\mathrm{AU}$, and orbital angles $g_{\rm in,0} = g_{\rm out,0} = 200°$, $h_{\rm in,0} = 180°$, $h_{\rm out,0} = 0$, and $i_{\rm tot,0} = 95°$.

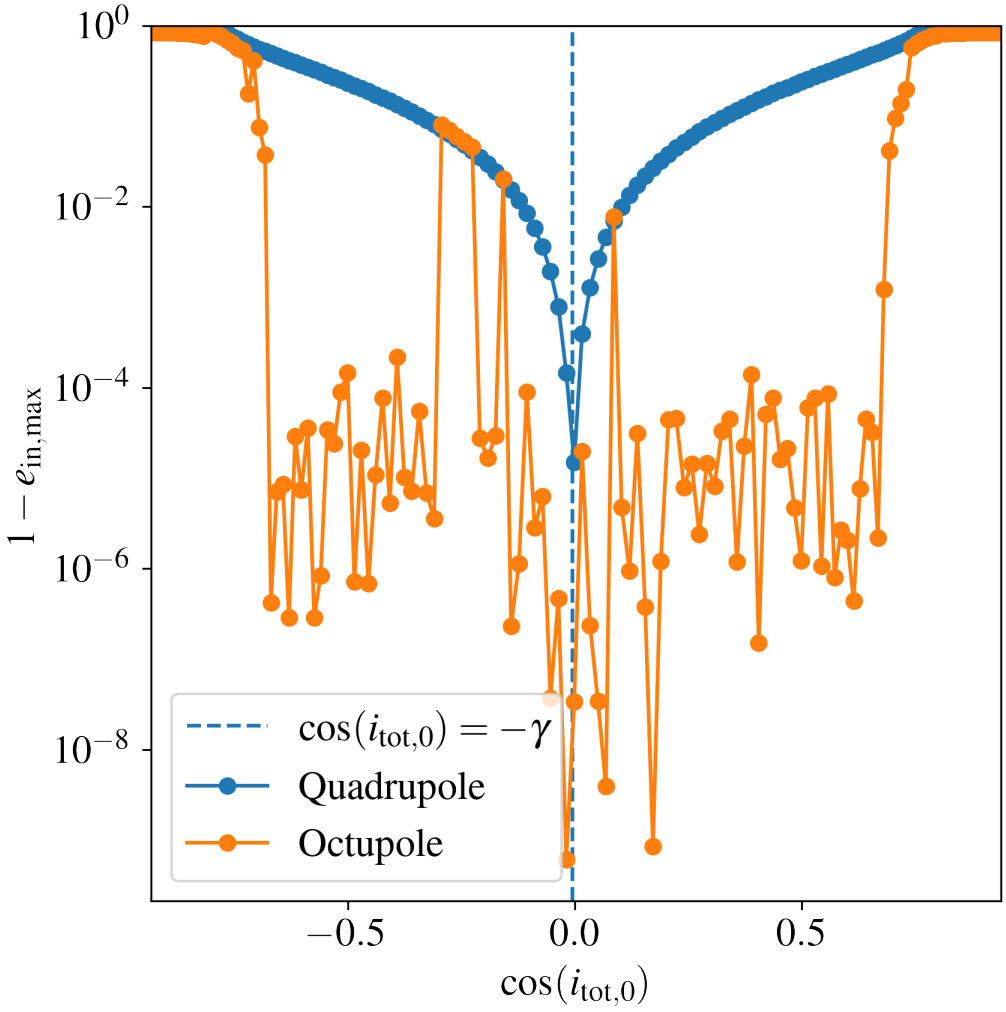

Figure 1.8. Maximum eccentricity $e_{\mathrm{in,max}}$ as a function of the initial relative inclination $i_{\mathrm{tot},0}$ for an exemplary triple. For the blue line only the quadrupole terms are included, for the orange line also the octupole terms are taken into account. Whereas the relative inclination is varied incrementally by steps of $1°$, the triple is always initialised with fixed masses $m_1 = 20\,\mathrm{M}_\odot$, $m_2 = 1\,\mathrm{M}_\odot$, and $m_3 = 50\,\mathrm{M}_\odot$, eccentricities $e_{\mathrm{in},0} = 0.001$ and $e_{\mathrm{out},0} = 0.6$, semi-major axes $a_{\mathrm{in},0} = 6\,\mathrm{AU}$ and $a_{\mathrm{out},0} = 80\,\mathrm{AU}$, and orbital angles $g_{\mathrm{in},0} = 45°$ and $g_{\mathrm{out},0} = 0°$, $h_{\mathrm{in},0} = 180°$, and $h_{\mathrm{out},0} = 0°$. The maximum eccentricity is recorded over an integration time of $1\,\mathrm{Myr}$.

1.2 Suppression by short-range forces and gravitational-wave emission

In the previous sections, we derived and investigated the dynamics of hierarchical triples which are only subject to Newtonian gravity. In a realistic astrophysical triple additional effects may become important and perturb the "clean" LK dynamics. For stellar triples these effects include tidal interactions between the inner binary stars, torques between them which arise from their rotation-induced oblateness, as well as relativistic corrections to the orbital evolution. These effects are described in more detail in Chapter 2. Here, we discuss how orbital precession induced by these effects can alter the dynamical evolution of a triple (Section 1.2.1), and investigate how LK oscillations may drive a merger of compact objects in the inner binary if GW emission is taken into account (Section 1.2.2). Since these effects become important if the binary is relatively close we can ignore them for the evolution of the outer orbit.

1.2.1 Precession due to short-range forces

Torques between the inner binary stars that arise from tidal interarctions and their rotation-induced oblateness cause their periapsis to precess about their orbital axis, i.e., there are finite extra terms $\dot{g}_{\rm in,extra} \neq 0$ that add up to the time derivative $\dot{g}_{\rm in}$ of the argument of the inner periapsis described by Eq. (1.35). Likewise, relativistic corrections of the inner orbit referred to as Schwarzschild precession advance the periapsis further.

If the precession of the inner orbit due to these additional effects is much faster than the timescale of LK oscillations (cf., Eq. (1.44)), the inner binary gets effectively shielded against the perturbation from the tertiary companion. As a consequence, the LK effect can get quenched and oscillations of the eccentricity and relative inclination become suppressed (Fabrycky & Tremaine, 2007; Naoz et al., 2013b; Liu et al., 2015).

As an example, we consider the relativistic Schwarzschild precession which can be written as

$$\left.\frac{{\rm d}g_{\rm in}}{{\rm d}t}\right|_{\rm 1PN} = \frac{3G^{3/2}m_{\rm in}^{3/2}}{a_{\rm in}^{5/2}c^2(1-e_{\rm in}^2)}. \tag{1.63}$$

In Fig. 1.9, we compare the maximum inner eccentricity of a triple when only the triple dynamics up to the octupole terms are taken into account with its evolution when also Schwarzschild precession is included. Clearly, the latter drastically suppresses the maxmimum eccentricity that the inner binary could attain. Due to the strong dependence of Eq. (1.63) on the inner semi-major axis $a_{\rm in}$ the quenching of the LK oscillations by the Schwarzschild precession can become

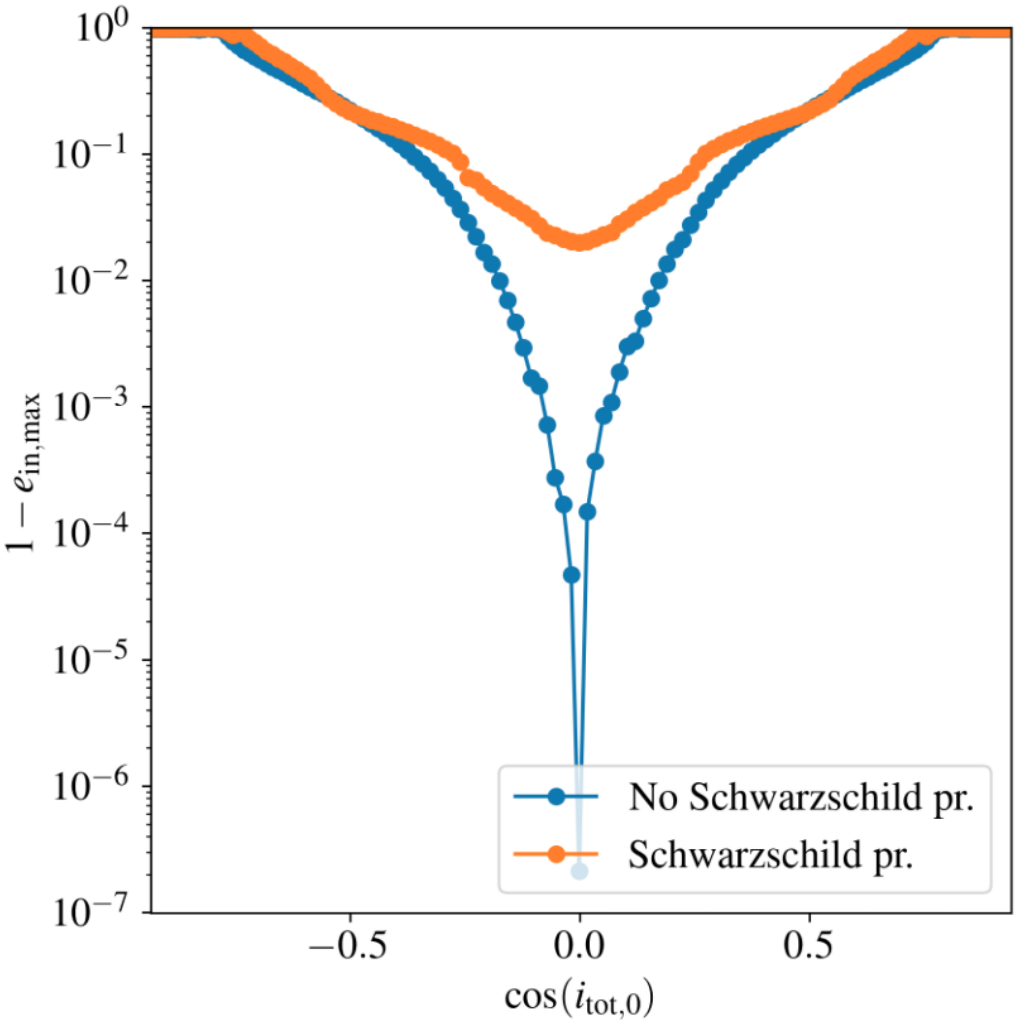

Figure 1.9. Suppression of the maximum eccentricity $e_{\mathrm{in,max}}$ by the relativistic Schwarzschild precession for an exemplary triple. For the blue line only the octupole evolution of the triple is taken into account, for the orange line also the Schwarzschild precession is considered. The triple parameters and total integration time are as in Fig. 1.8 except for $a_{\mathrm{in},0} = 0.5\,\mathrm{AU}$ and $a_{\mathrm{out},0} = 50\,\mathrm{AU}$.

important only when the inner binary is relatively tight. Similar findings hold for precession induced by tidal interactions and quadrupolar deformation of the stars (see Chapter 2).

1.2.2 Gravitational-wave emission from the inner binary

In general relativity, two masses that orbit each other as a binary emit GWs (Einstein, 1918) which carry away orbital energy and angular momentum. As a consequence, the semi-major axis a and eccentricity e of the binary orbit decay, i.e., the orbit inspirals and circularises, respectively, at

rates that can be written as (Peters, 1964)

$$\left.\frac{\mathrm{d}a}{\mathrm{d}t}\right|_{\mathrm{GW}} = -\frac{64}{5}\frac{G^3\mu m^2}{c^5 a^3(1-e^2)^{7/2}}\left(1+\frac{73}{24}e^2+\frac{37}{96}e^4\right), \tag{1.64}$$

$$\left.\frac{\mathrm{d}e}{\mathrm{d}t}\right|_{\mathrm{GW}} = -\frac{304}{15}\frac{G^3\mu m^2 e}{c^5 a^4(1-e^2)^{5/2}}\left(1+\frac{121}{304}e^2\right), \tag{1.65}$$

where m and μ are the total mass and reduced mass of the binary, respectively. If the binary is in isolation and other effects could be neglected it would thus coalesce after a finite time τ_{coal} which can be found by integrating Eqs. (1.64) and (1.65) yielding

$$\tau_{\mathrm{coal}} = 3.211\times10^{17}\,\mathrm{yr}\left(\frac{a}{\mathrm{AU}}\right)^4\left(\frac{\mathrm{M}_\odot}{m}\right)^2\left(\frac{\mathrm{M}_\odot}{\mu}\right)F(e), \tag{1.66}$$

where

$$F(e) = \frac{48}{19}\frac{1}{g^4(e)}\int_0^e \frac{g^4(e')(1-e^2)^{5/2}}{e'(1+\frac{121}{304}e'^2)}\,\mathrm{d}e' \tag{1.67}$$

can be evaluated numerically using $g(e) = e^{12/19}(1-e^2)^{-1}(1+121e^2/304)^{870/229}$. For instance, an equal-mass mass binary with $m_1 = m_2 = 30\,\mathrm{M}_\odot$ would only merge within $\tau_{\mathrm{coal}} < 10\,\mathrm{Gyr}$ if it is initially closer than $a_{\mathrm{in},0} \lesssim 0.1\,\mathrm{AU}$.

The r.h.s. of Eqs. (1.64) and (1.65) strongly depend on the eccentricity of the orbit and diverge for $e \to 1$. If the binary is not in isolation but perturbed by a distant tertiary companion, the high-eccentricity excursions in the LK mechanism can therefore effectively reduce the merger time compared to Eq. (1.66). Equivalently, a binary that gets significantly perturbed by a tertiary companion could merge within a given time even if starts from larger values of the initial semi-major axis. As an example, we show in Fig. 1.10 the evolution of exemplary binaries with and without tertiary companion. Within the given integration time of $5\times10^7\,\mathrm{yr}$ only the binary starting with an initial semi-major axis $a_0 = 10^{-2}\,\mathrm{AU}$ merges in the isolated case. Yet, placing the binaries in a triple allows the two systems with the largest initial semi-major axis ratios $\alpha = a_{\mathrm{in},0}/a_{\mathrm{out},0}$, i.e, those with $a_{\mathrm{in},0} = 10^1$ (orange) and $a_{\mathrm{in},0} = 10^2\,\mathrm{AU}$ (blue), to merge as well. Their evolution is characteristic for two classes of tertiary-driven mergers. In the former case, mild eccentricity excitations one after another gradually decrease the semi-major axis until the inner binary enters a regime (after $t \simeq 2-3\times10^7\,\mathrm{yr}$) where further perturbation from the tertiary companion is suppressed by the Schwarzschild precession and the binary merges due to GW emission. In contrast, the latter case exhibits much higher eccentricity excitations. As a consequence, the GW emission during one or a few high-eccentricity excursions is strong enough to promote a quick merger, which is oftentimes referred to as a "one-shot merger". Meanwhile, the binaries with initial semi-major axes of 10^{-1} and $10^0\,\mathrm{AU}$ are neither tight enough to merge within the

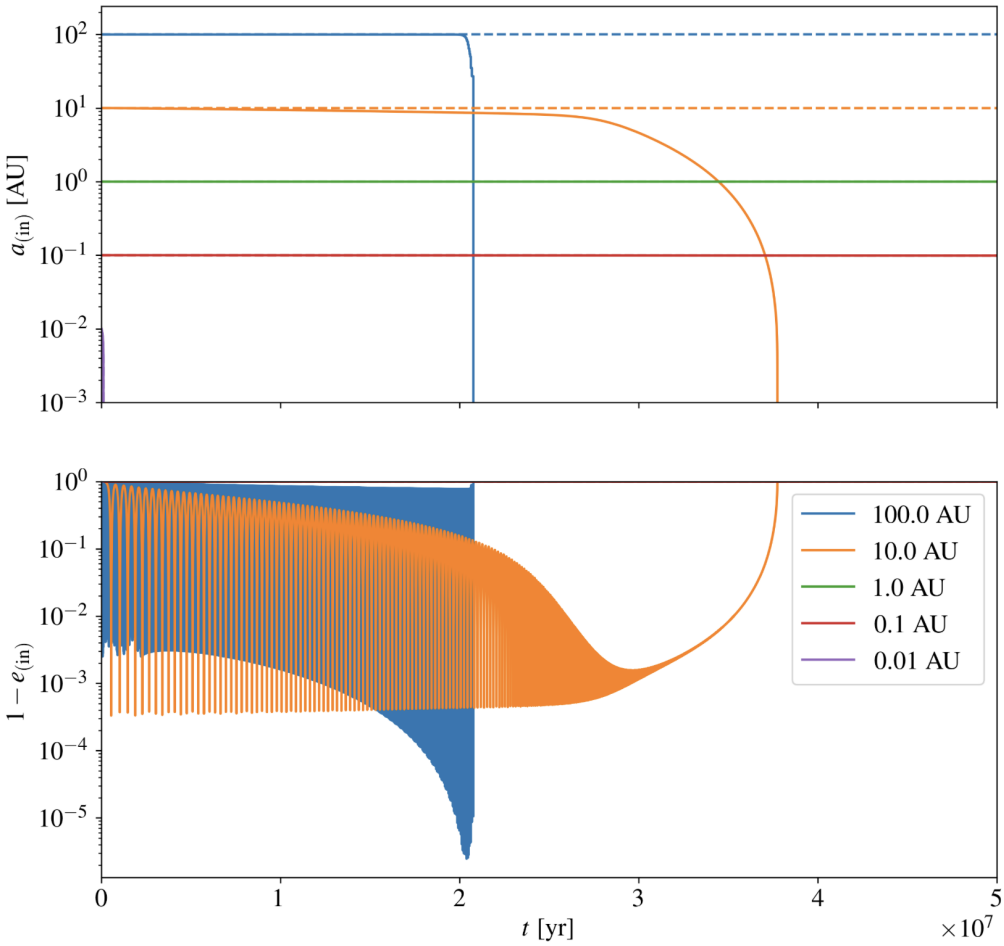

Figure 1.10. Binary evolution towards a merger. These simulations include Schwarzschild precession and GW emission (dashed lines). Solid lines also take the octupole perturbation from a tertiary companion into account. Between different colours we vary the initial semi-major axis of the binary from 10^{-2} to $10^{2}\,\mathrm{AU}$. The other parameters are the same in each simulation: fixed masses $m_1 = 30\,\mathrm{M}_\odot$, $m_2 = 20\,\mathrm{M}_\odot$, and $m_3 = 30\,\mathrm{M}_\odot$, initial eccentricities $e_{\mathrm{in},0} = 0.001$ and $e_{\mathrm{out},0} = 0.3$, outer semi-major axis $a_{\mathrm{out},0} = 500\,\mathrm{AU}$, and orbital angles $g_{\mathrm{in},0} = 45°$ and $g_{\mathrm{out},0} = 0°$, $h_{\mathrm{in},0} = 180°$, and $h_{\mathrm{out},0} = 0°$.

integration time due to GW emission in isolation nor is their semi-major axis ratio α large enough to experience significant LK oscillations that could promote a merger.

The evolution in which a binary undergoes a tertiary-driven merger is referred to as the triple (formation) channel and has been studied in the context of double compact objects (DCO), i.e., BBHs, BNSs, or neutron star black hole binaries (NSBHs), which are accompanied by another stellar component or that orbit a super-massive BH perturber (e.g., Blaes et al., 2002; Thompson, 2011; Antonini & Perets, 2012; Antonini et al., 2014; Prodan et al., 2015; Bonetti et al., 2016; Silsbee & Tremaine, 2017; Liu & Lai, 2017, 2018; Antonini et al., 2018; Rodriguez & Antonini, 2018; Grishin et al., 2018; Hoang et al., 2018, this work).

1.3 Thesis structure

The main goal of this thesis is to combine the gravitational dynamics of hierarchical triples with stellar physics to study the evolution of massive stellar triples. For this purpose, we introduce a numerical framework which simultaneously takes into account the gravitational triple dynamics and relevant aspects of the evolution of massive stars, such as stellar winds, supernova (SN) kicks, binary mass transfer, and tidal interactions. This framework allows us to rapidly evolve a population of massive stellar triples from birth until they possibly form DCOs and subsequently merge leading to a GW event.

In Chapter 2, we describe in detail the numerical framework which has been implemented as a Triple Stellar Evolution code `TSE`*. We explain all dynamical and stellar physical effects that are taken into account. We use this code to evolve a population of massive stellar triples and study their various evolutionary pathways. Thus, the focus of Chapter 2 will be the stellar evolution of the triples, i.e., the time from the zero-age-main-sequence (ZAMS) until the possible formation of compact objects or an otherwise terminating event.

In Chapter 3, we focus on stellar triples in which the inner binary stars merge before they could form any compact object. We carefully consider the subsequent post-merger evolution of the merger product stars and the tertiary companions. We find that these two stars can lead to the formation of merging BBHs. We investigate the properties of the merging BBHs which are formed via this newly proposed formation channel and compare them with the parameter distributions inferred from GW observations.

In Chapter 4, we are considering a topic which is not exclusively relevant to stellar triples, but to the evolution of massive multiple stars in general. Here, we are investigating the dynamical evolution of the rotational angular momentum vectors (spins) of massive stars which are transferring mass to their binary companion. We find that, in some models, the spin vector of the mass loosing star becomes smaller in magnitude and is flipping onto the orbital plane of the binary. We are discussing the significance of this effect in light of competing effects such as tides and investigate implications for the formation of BBHs.

Finally, we summarise and discuss the findings of this thesis in Chapter 5.

Large parts of this thesis, especially Chapters 2 – 5 have been to a great extent adopted word-by-word from published work, Stegmann et al. (2022b), Stegmann et al. (2022a), and Stegmann & Antonini (2021), respectively, which were devised, conducted, and written by the author of this thesis.

*Publicly available at: `https://github.com/stegmaja/TSE`

If not stated differently, the magnitude, unit vector, and time derivative of some vector $\boldsymbol{V}$ are written as $V = |\boldsymbol{V}|$, $\hat{\boldsymbol{V}} = \boldsymbol{V}/V$, and $\dot{\boldsymbol{V}} = \mathrm{d}\boldsymbol{V}/\mathrm{d}t$, respectively. G and c refer to the gravitational constant and the speed of light, respectively. The value of solar metallicity is set to $Z_\odot = 0.02$.

Chapter 2

Evolution of massive stellar triples

In the previous chapter, we have considered the dynamics of three hierarchical point masses which are subject to Newtonian gravity. We have seen that the mutual gravitational interaction can lead to large-amplitude LK oscillations of the eccentricities and relative inclination of the inner and outer orbit of the triple. As a consequence, the periapsis $a_{\rm in}(1-e_{\rm in})$ of the inner binary can assume very small values so that the two inner binary masses approach each other very closely.

Considering massive stellar triples, the tertiary companion could enrich the variety of evolutionary pathways in the inner binary by driving it to close stellar interactions (Toonen et al., 2016, 2020). Yet, simulating the evolution of massive stellar triples poses a difficult challenge since the stellar physics of each individual star and the gravitational three-body dynamics have to be combined in a self-consistent way. For massive stars both of these aspects are closely intertwined. For instance, kicks experienced in the SN explosions modify and potentially disrupt the three-body configuration. Likewise, massive stars at high metallicity suffer significant mass loss through stellar winds that loosen the inner and outer orbits (Castor et al., 1975; Vanbeveren, 1991; Vink et al., 2001; Schneider et al., 2015; Mapelli, 2016). It has been shown that mass loss in the inner binary due to winds or at compact object formation could induce or strengthen the LK effect (Shappee & Thompson, 2013; Michaely & Perets, 2014). In addition, massive stars attain large radii as they evolve off the main-sequence (MS) and beyond, so that RLO and mergers are expected to occur frequently in isolated massive binaries (Bonnell & Bate, 2005; Eldridge et al., 2008; Sana et al., 2012; Schneider et al., 2021). For example, more than $70\,\%$ of Galactic massive O-type stars are expected to undergo at least one mass transfer episode with their binary companion (Sana et al., 2012).

In this chapter, we introduce the code `TSE` that follows the secular evolution of hierarchical stellar triples from the ZAMS until they possibly form compact objects. `TSE` builds upon the most updated prescriptions of the widely-adopted single and binary evolution codes `SSE` (Hurley et al.,

2000) and BSE (Hurley et al., 2002), respectively, and employs the secular three-body equations of motion up to the octupole order with relativistic corrections up to the 2.5 post-Newtonian order. Thus, TSE complements previous population synthesis codes which are designed to evolve stellar triples or higher-order configurations, e.g., MSE (Hamers et al., 2021) and TrES (Toonen et al., 2016). TSE provides an evolution scheme for the stellar masses, radii, orbital elements, and spin vectors. Here, we apply this code to a population of massive stellar triples to study their evolution until they form a DCO in the inner binary.

2.1 Methods

2.1.1 Triple dynamics

In this section, we describe the numerical method we use to study the long-term evolution of hierarchical stellar triples. Compared to the triple dynamics discussed in Chapter 1, we modifiy the description in two ways.

At first, the triples are no longer treated as a collection of three point masses. Instead, we associate with each of the stars a finite radius $R_{1(2)(3)}$. The evolution of each individual star makes $R_{1(2)(3)} = R_{1(2)(3)}(t)$ functions of time which, in the case of massive stars, typically span several orders of magnitude over a timescale of a few $\sim \mathrm{Myr}$. Furthermore, a star with a finite radius can carry some rotational angular momentum (spin) vector $\boldsymbol{S}_{1(2)}$ with magnitude

$$S_{1(2)} = \kappa m_{1(2)} R_{1(2)}^2 \Omega_{1(2)}, \tag{2.1}$$

where $\Omega_{1(2)}$ is the angular velocity of the rotating star and we set $\kappa = 0.1$ (Motz, 1952). As we will see below, taking finite stellar radii and spins into account does affect the stellar evolution and gravitational dynamics of the triples. For instance, a star with an expanded radius may start to transfer mass to the binary companion, or in the case of an expanded tertiary companion, to the inner binary. Additionally, introducing a spin angular momentum to the inner binary stars affects the way how they could torque each other and their orbit via tidal interactions. Since tidal interactions are ineffective between stars at a large distance, we do not consider the effect of the spin of the distant tertiary companion $\mathbf{S}_3$.

Secondly, we opt to describe the orbital evolution in terms of the dimensionless orbital angular momentum vector $\boldsymbol{j}_{\mathrm{in(out)}}$ and eccentricity vector $\boldsymbol{e}_{\mathrm{in(out)}}$ instead of the Delaunay elements. They

are defined as (e.g., Tremaine et al., 2009)

$$\boldsymbol{j}_{\rm in(out)} = \sqrt{1-e_{\rm in(out)}^2}\hat{\boldsymbol{j}}_{\rm in(out)}, \tag{2.2}$$

$$\boldsymbol{e}_{\rm in(out)} = e_{\rm in(out)}\hat{\boldsymbol{e}}_{\rm in(out)}, \tag{2.3}$$

where $\hat{\boldsymbol{j}}_{\rm in(out)}$ and $\hat{\boldsymbol{e}}_{\rm in(out)}$ are orthogonal unit vectors pointing along the orbital angular momentum $\boldsymbol{G}_{\rm in(out)}$ and the pericentre, respectively. In Chapter 1 it was instructive to consider the orbital evolution of the three hierarchical point masses in terms of their Delaunay elements because then, the LK oscillations take a relatively simple form. This simplicity relies on the fact that the total angular momentum vector $\mathbf{G}_{\rm tot}$ is constant in the case of Newtonian point masses. In the case of stellar triples $\mathbf{G}_{\rm tot}$ is in general not conserved. As we will see, a large variety of additional effects can alter $\mathbf{G}_{\rm in(out)}$ independently from each other so that $\mathbf{G}_{\rm tot} \neq \rm const.$ For example, the masses of the three stars are neither constant as they suffer mass loss through stellar winds or transfer mass from one to another, and a star could receive strong natal kicks in the event of a core-collapse SN.

While it is possible to transform the equations of motion of the Delaunay elements to the non-inertial frame that is defined by a rotating $\mathbf{G}_{\rm tot}$ (e.g., Blaes et al., 2002), we find it more convenient to equivalently express the stellar triple dynamics in terms of the dimensionless orbital angular momentum vector $\boldsymbol{j}_{\rm in(out)}$ and eccentricity vector $\boldsymbol{e}_{\rm in(out)}$.

In this formalism, the secular equations of motion for the inner orbit, $\boldsymbol{j}_{\rm in}$ and $\boldsymbol{e}_{\rm in}$, its semi-major axis $a_{\rm in}$, and the spin vectors $\boldsymbol{S}_{1(2)}$ can be written as (e.g., Anderson et al., 2016)

$$\frac{{\rm d}\boldsymbol{j}_{\rm in}}{{\rm d}t} = \left.\frac{{\rm d}\boldsymbol{j}_{\rm in}}{{\rm d}t}\right|_{\rm LK,Quad} + \left.\frac{{\rm d}\boldsymbol{j}_{\rm in}}{{\rm d}t}\right|_{\rm LK,Oct} + \left.\frac{{\rm d}\boldsymbol{j}_{\rm in}}{{\rm d}t}\right|_{\rm Tide} + \left.\frac{{\rm d}\boldsymbol{j}_{\rm in}}{{\rm d}t}\right|_{\rm Rot} + \left.\frac{{\rm d}\boldsymbol{j}_{\rm in}}{{\rm d}t}\right|_{\rm 1.5PN} + \left.\frac{{\rm d}\boldsymbol{j}_{\rm in}}{{\rm d}t}\right|_{\rm GW}, \tag{2.4}$$

$$\begin{aligned}\frac{{\rm d}\boldsymbol{e}_{\rm in}}{{\rm d}t} = &\left.\frac{{\rm d}\boldsymbol{e}_{\rm in}}{{\rm d}t}\right|_{\rm LK,Quad} + \left.\frac{{\rm d}\boldsymbol{e}_{\rm in}}{{\rm d}t}\right|_{\rm LK,Oct} + \left.\frac{{\rm d}\boldsymbol{e}_{\rm in}}{{\rm d}t}\right|_{\rm Tide} \\ &+ \left.\frac{{\rm d}\boldsymbol{e}_{\rm in}}{{\rm d}t}\right|_{\rm Rot} + \left.\frac{{\rm d}\boldsymbol{e}_{\rm in}}{{\rm d}t}\right|_{\rm 1PN} + \left.\frac{{\rm d}\boldsymbol{e}_{\rm in}}{{\rm d}t}\right|_{\rm 1.5PN} + \left.\frac{{\rm d}\boldsymbol{e}_{\rm in}}{{\rm d}t}\right|_{\rm GW},\end{aligned} \tag{2.5}$$

$$\frac{{\rm d}a_{\rm in}}{{\rm d}t} = \left.\frac{{\rm d}a_{\rm in}}{{\rm d}t}\right|_{\rm Tide} + \left.\frac{{\rm d}a_{\rm in}}{{\rm d}t}\right|_{\rm Mass} + \left.\frac{{\rm d}a_{\rm in}}{{\rm d}t}\right|_{\rm GW}, \tag{2.6}$$

$$\frac{{\rm d}\boldsymbol{S}_{1(2)}}{{\rm d}t} = \left.\frac{{\rm d}\boldsymbol{S}_{1(2)}}{{\rm d}t}\right|_{\rm Tide} + \left.\frac{{\rm d}\boldsymbol{S}_{1(2)}}{{\rm d}t}\right|_{\rm Rot} + \left.\frac{{\rm d}\boldsymbol{S}_{1(2)}}{{\rm d}t}\right|_{\rm Mass} + \left.\frac{{\rm d}\boldsymbol{S}_{1(2)}}{{\rm d}t}\right|_{\rm 1PN}, \tag{2.7}$$

where the quadrupole $(\rm LK, Quad)$ and octupole $(\rm LK, Quad)$ contributions to the LK effect have been discussed in Chapter 1 and in its vectorial form are given by Eqs. (17) – (20) of Liu et al. (2015). The remaining terms on the r.h.s. are described in the following subsections. Treating the spins of the inner binary stars as vector quantities and including a vectorial prescription of

tides, de Sitter precession, and Lense-Thirring precession (see below) is one main difference of TSE compared to previous population synthesis codes.

Tidal interaction (Tide)

In close binaries, the mutual gravitational interaction between the stars raises tidal bulges on their surfaces (e.g., Hut, 1981; Zahn, 1989; Eggleton et al., 1998). The viscosity of the internal motion within the stars prevents these bulges to instantaneously align with the interstellar axis while dissipating kinetic energy into heat. Thus, the tilted tidally deformed stars torque each other leading to an exchange of rotational and orbital angular momentum. Generally, the strength of this interaction can be quantified in terms of a small lag time constant τ by which the tidal bulges lag behind or lead ahead the interstellar axis (Hut, 1981). In this work, τ is set to $1\,\mathrm{s}$ (Anderson et al., 2016). The full equations of motion for $\boldsymbol{e}_{\rm in}$, $\boldsymbol{S}_{1(2)}$, $a_{\rm in}$, and $\boldsymbol{j}_{\rm in}$ in Eqs. (2.4) – (2.7) (Tide) are adopted from Eqs. (21), (22), and (56) of Correia et al. (2011). Accordingly, the direction of the angular momentum flow and consequently the change of $e_{\rm in}$ and $a_{\rm in}$ depend on the ratio between orbital mean motion $n_{\rm in} = 2\pi/P_{\rm in}$ and the spin rotation rate along the orbital normal $\Omega_{1(2)} \cdot \hat{\boldsymbol{j}}_{\rm in}$ (Correia et al., 2011)

$$\dot{L}_{\rm in} \propto \sum_{i=1,2} \left[\frac{f_5(e_{\rm in})}{j_{\rm in}^9} \frac{\boldsymbol{\Omega}_i \cdot \hat{\boldsymbol{j}}_{\rm in}}{n_{\rm in}} - \frac{f_2(e_{\rm in})}{j_{\rm in}^{12}} \right], \tag{2.8}$$

$$\frac{\dot{e}_{\rm in}}{e_{\rm in}} \propto \sum_{i=1,2} \left[\frac{11}{18} \frac{f_4(e_{\rm in})}{j_{\rm in}^{10}} \frac{\boldsymbol{\Omega}_i \cdot \hat{\boldsymbol{j}}_{\rm in}}{n_{\rm in}} - \frac{f_3(e_{\rm in})}{j_{\rm in}^{13}} \right], \tag{2.9}$$

$$\frac{\dot{a}_{\rm in}}{a_{\rm in}} \propto \sum_{i=1,2} \left[\frac{f_2(e_{\rm in})}{j_{\rm in}^{12}} \frac{\boldsymbol{\Omega}_i \cdot \hat{\boldsymbol{j}}_{\rm in}}{n_{\rm in}} - \frac{f_1(e_{\rm in})}{j_{\rm in}^{15}} \right], \tag{2.10}$$

where the polynomials $f_{1,2,\ldots,5}(e_{\rm in})$ are given in Appendix A.1. In our simulation, the initial rotational periods of the stars are typically a few days long, $1/\Omega_{1(2)} \sim \mathcal{O}(\mathrm{days})$, which is much shorter or, at most, roughly equal to the initial orbital period (see Section 2.2). Unless the stellar spins are retrograde ($\hat{\boldsymbol{\Omega}}_{1(2)} \cdot \hat{\boldsymbol{j}}_{\rm in} < 0$), we can therefore expect that tides cause angular momentum to initially flow from the stellar rotation to the inner orbital motion and the eccentricity and semi-major axis to increase. Tides operate to circularise and contract the orbit only after the angular momentum flow peters out around $\boldsymbol{\Omega}_i \cdot \hat{\boldsymbol{j}}_{\rm in}/n_{\rm in} = f_2/f_5 j_{\rm in}^3$ for which the r.h.s. of Eq. (2.8) becomes zero and of Eqs. (2.9) and (2.10) negative for any eccentricity value $0 < e_{\rm in} < 1$ (Correia et al., 2011).

Furthermore, the torques exerted on the static tidal bulges induce a precession of $\boldsymbol{e}_{\rm in}$ about $\hat{\boldsymbol{j}}_{\rm in}$

on a timescale

$$t_{\rm Tide} = 1 \Big/ \sum_{i=1,2} 15 k_{\rm A} n_{\rm in} \frac{m_{(i-1)}}{m_i} \left(\frac{R_i}{a_{\rm in}}\right)^5 \frac{f_4(e_{\rm in})}{j_{\rm in}^{10}}, \tag{2.11}$$

where $k_{\rm A} = 0.014$ is the classical apsidal motion constant (Fabrycky & Tremaine, 2007) and which is usually much shorter than the time by which tides could circularise the orbit.

The tidal description outlined above is more appropriate for stars with deep convective envelopes. Following Hurley et al. (2002), we include in TSE a different tidal mechanism for stars which have a radiative envelope. In this case, the dominant tidal forces are dynamical and emerge from stellar oscillations which are excited by the binary companion (Zahn, 1975, 1977). In that case, we parameterise the tidal strength by the lag time (Hut, 1981)

$$\tau_{1(2)} = \frac{R_{1(2)}}{G m_{1(2)} T_{1(2)}}, \tag{2.12}$$

where

$$\frac{k_A}{T_{1(2)}} = 1.9782 \times 10^4 \left(\frac{m_{1(2)}}{\rm M_\odot}\right) \left(\frac{R_{1(2)}}{\rm R_\odot}\right)^2 \left(\frac{\rm R_\odot}{a_{\rm in}}\right)^5 \left(1 + \frac{m_{2(1)}}{m_{1(2)}}\right)^{5/6} \frac{E_{2,1(2)}}{\rm yr} \tag{2.13}$$

and

$$E_{2,1(2)} \simeq 10^{-9} \left(\frac{m_{1(2)}}{\rm M_\odot}\right)^{2.84}. \tag{2.14}$$

Following Hurley et al. (2002) the code applies dynamical tides for all MS stars with a mass greater than $1.25\ \rm M_\odot$, core Helium Burning stars, and naked helium MS stars.

The coefficient E_2 is related to the structure of the star and refers to the coupling between the tidal potential and gravity mode oscillations. Its value is difficult to estimate since it is very sensitive to the structure of the star and therefore to the exact treatment of stellar evolution. Importantly, the equations of motion (2.11) were developed in Hut (1981) under the assumption that the tides reach an equilibrium shape with a constant time lag. These equations hold for very small deviations in position and amplitude with respect to the equipotential surfaces. Thus, we caution that dynamical tides, where the stars oscillates radially, are not properly described by the constant time-lag model. At every periastron passage, tidal stretching and compression can force the star to oscillate in a variety of eigenmodes. The excitation and damping of these eigenmodes can significantly affect the secular evolution of a binary orbit (Wu, 2018; Vick & Lai, 2019; Vick et al., 2019).

Because the physics of stellar tides is much uncertain and the efficiency of tides itself is debated, in the simulations presented here we consider two choices. In our fiducial models we opt for a simplified approach in which we employ the equilibrium tide equations for all stars with a constant

$\tau = 1\,\mathrm{s}$, thus encapsulating all the uncertainties related to tides in this constant factor. In another set of models (`Incl. dyn. tides`), we follow the approach of Hurley et al. (2002) and use either equilibrium or dynamical tides depending on the stellar mass and type as described above.

We find that our main results are not significantly affected by the implementation of dynamical tides in the code. In Section 3.2, we will therefore primarily focus on our fiducial choice with constant $\tau = 1\,\mathrm{s}$.

Rotational distortion (Rot)

The rotation of each star distorts its shape from spherical symmetry which induces a quadrupole moment. As a result, the binary stars torque each other yielding (e.g., Eggleton & Kiseleva-Eggleton, 2001)

$$\left.\frac{\mathrm{d}\boldsymbol{e}_{\mathrm{in}}}{\mathrm{d}t}\right|_{\mathrm{Rot}} = \sum_{i=1,2} \frac{k_{\mathrm{A}} m_{(i-1)} R_i^5}{2 n_{\mathrm{in}} \mu_{\mathrm{in}} a_{\mathrm{in}}^5} \frac{e_{\mathrm{in}}}{j_{\mathrm{in}}^4} \left\{ \left[2\left(\boldsymbol{\Omega}_i \cdot \hat{\boldsymbol{j}}_{\mathrm{in}}\right)^2 - (\boldsymbol{\Omega}_i \cdot \hat{\boldsymbol{q}}_{\mathrm{in}})^2 - (\boldsymbol{\Omega}_i \cdot \hat{\boldsymbol{e}}_{\mathrm{in}})^2 \right] \hat{\boldsymbol{q}}_{\mathrm{in}} + 2\left(\boldsymbol{\Omega}_i \cdot \hat{\boldsymbol{q}}_{\mathrm{in}}\right)\left(\boldsymbol{\Omega}_i \cdot \hat{\boldsymbol{j}}_{\mathrm{in}}\right) \hat{\boldsymbol{j}}_{\mathrm{in}} \right\}, \tag{2.15}$$

$$\left.\frac{\mathrm{d}\boldsymbol{S}_{1(2)}}{\mathrm{d}t}\right|_{\mathrm{Rot}} = \sum_{i=1,2} \frac{k_{\mathrm{A}} m_{(i-1)} R_i^5}{n_{\mathrm{in}} \mu_{\mathrm{in}} a_{\mathrm{in}}^5} \frac{L_{\mathrm{in}}}{j_{\mathrm{in}}^4} \left(\boldsymbol{\Omega}_i \cdot \hat{\boldsymbol{j}}_{\mathrm{in}}\right) \left[\left(\boldsymbol{\Omega}_i \cdot \hat{\boldsymbol{q}}_{\mathrm{in}}\right) \hat{\boldsymbol{e}}_{\mathrm{in}} - \left(\boldsymbol{\Omega}_i \cdot \hat{\boldsymbol{e}}_{\mathrm{in}}\right) \hat{\boldsymbol{q}}_{\mathrm{in}} \right], \tag{2.16}$$

$$\left.\frac{\mathrm{d}\boldsymbol{j}_{\mathrm{in}}}{\mathrm{d}t}\right|_{\mathrm{Rot}} = -\frac{j_{\mathrm{in}}}{L_{\mathrm{in}}} \sum_{i=1,2} \left.\frac{\mathrm{d}\boldsymbol{S}_{\mathrm{i}}}{\mathrm{d}t}\right|_{\mathrm{Rot}}, \tag{2.17}$$

where $\hat{\boldsymbol{q}}_{\mathrm{in}} = \hat{\boldsymbol{j}}_{\mathrm{in}} \times \hat{\boldsymbol{e}}_{\mathrm{in}}$. Analogously to the tidal torques, the first term in the bracket of Eq. (2.15) causes the inner orbit's periapsis to precess about $\hat{\boldsymbol{j}}_{\mathrm{in}}$ on a timescale

$$t_{\mathrm{Rot}} = 1 \Big/ \sum_{i=1,2} \frac{k_{\mathrm{A}} m_{(i-1)} R_i^5}{2 n_{\mathrm{in}} \mu_{\mathrm{in}} a_{\mathrm{in}}^5 j_{\mathrm{in}}^4}. \tag{2.18}$$

Mass-loss (Mass)

During its lifetime, the mass of a star can substantially decrease as a result of, e.g., stellar winds (Hurley et al., 2000) and the explosive mass loss in a SN (Blaauw, 1961). If the mass loss of the star is isotropic its spin simply changes as (cf., Eq. (2.1))

$$\left.\frac{\mathrm{d}\boldsymbol{S}_{1(2)}}{\mathrm{d}t}\right|_{\mathrm{Mass}} = \boldsymbol{S}_{1(2)} \frac{\dot{m}_{1(2)}}{m_{1(2)}}, \tag{2.19}$$

where $\dot{m}_{1(2)} = \mathrm{d}m_{1(2)}/\mathrm{d}t \leq 0$ is the mass loss rate. While the stars lose mass, the specific orbital angular momentum $G_{\rm in}/\mu_{\rm in}$ is conserved. Hence, the semi-major axis of the inner orbit changes as (cf., Eq. (1.1))

$$\left.\frac{\mathrm{d}a_{\rm in}}{\mathrm{d}t}\right|_{\rm Mass} = -a_{\rm in}\frac{\dot{m}_{\rm in}}{m_{\rm in}}, \tag{2.20}$$

where $\dot{m}_{\rm in} = \dot{m}_1 + \dot{m}_2$, i.e., mass loss loosens the binary since $\dot{m}_{\rm in} < 0$ implies $\mathrm{d}a_{\rm in}/\mathrm{d}t > 0$.

Schwarzschild and de Sitter precession (1PN)

At first post-Newtonian order relativistic effects cause the eccentricity vector $\boldsymbol{e}_{\rm in}$ of the inner orbit to precess about the orbital axis $\hat{\boldsymbol{j}}_{\rm in}$ as

$$\left.\frac{\mathrm{d}\boldsymbol{e}_{\rm in}}{\mathrm{d}t}\right|_{\rm 1PN} = \frac{e_{\rm in}}{t_{\rm 1PN}}\hat{\boldsymbol{q}}_{\rm in}, \tag{2.21}$$

where we defined the associated timescale

$$t_{\rm 1PN} = \frac{c^2 a_{\rm in}^{5/2} j_{\rm in}^2}{3G^{3/2} m_{\rm in}^{3/2}}. \tag{2.22}$$

This apsidal precession is referred to as Schwarzschild (1916) precession. Also at first post-Newtonian order, we have the de Sitter precession of the stellar spins $\boldsymbol{S}_{1(2)}$ that are parallel-transported along the orbit

$$\left.\frac{\mathrm{d}\boldsymbol{S}_{1(2)}}{\mathrm{d}t}\right|_{\rm 1PN} = \frac{S_{1(2)}}{t_{\boldsymbol{S}_{1(2)}}}\hat{\boldsymbol{j}}_{\rm in} \times \hat{\boldsymbol{S}}_{1(2)}, \tag{2.23}$$

where

$$t_{\boldsymbol{S}_{1(2)}} = \frac{c^2 a_{\rm in} j_{\rm in}^2}{2G\mu_{\rm in} n_{\rm in}}\left[1 + \frac{3m_{2(1)}}{4m_{1(2)}}\right]^{-1}. \tag{2.24}$$

Lense-Thirring precession (1.5PN)

At 1.5 post-Newtonian order, the spins of the inner binary members back-react on the orbit inducing a frame-dragging effect. As a result, the orbit changes as (Barker & O'Connell, 1975;

Rodriguez & Antonini, 2018)

$$\left.\frac{\mathrm{d}\boldsymbol{e}_{\rm in}}{\mathrm{d}t}\right|_{\rm 1.5PN} = \frac{2G}{c^2}\sum_{i=1,2}\frac{S_i e_{\rm in}}{a_{\rm in}^3 j_{\rm in}^3}\left(1+\frac{3m_{(i-1)}}{4m_i}\right) \times\left[\hat{\boldsymbol{S}}_i - 3(\hat{\boldsymbol{S}}_i\cdot\hat{\boldsymbol{j}}_{\rm in})\right]\hat{\boldsymbol{e}}_{\rm in}, \tag{2.25}$$

$$\left.\frac{\mathrm{d}\boldsymbol{j}_{\rm in}}{\mathrm{d}t}\right|_{\rm 1.5PN} = \frac{2G}{c^2}\sum_{i=1,2}\frac{S_i}{a_{\rm in}^3 j_{\rm in}^2}\left(1+\frac{3m_{(i-1)}}{4m_i}\right)\hat{\boldsymbol{S}}_i\times\hat{\boldsymbol{j}}_{\rm in}. \tag{2.26}$$

The precessional term on the r.h.s. of Eq. (2.21) is larger than that of Eq. (2.25) by a factor $\sim L_{12}/S_{1(2)} > 1$ for the stellar systems we are interested in.

Gravitational waves (GW)

As described in Chapter 1, GW emission from the inner binary carry away orbital energy and angular momentum. As a consequence, the inner orbit decays and circularises. This dissipation effect can be included in the vectorial Eqs. (2.4) and (2.5) as (Rodriguez & Antonini, 2018)

$$\left.\frac{\mathrm{d}\boldsymbol{e}_{\rm in}}{\mathrm{d}t}\right|_{\rm GW} = \left.\frac{\mathrm{d}e_{\rm in}}{\mathrm{d}t}\right|_{\rm GW}\boldsymbol{e}_{\rm in}, \tag{2.27}$$

$$\left.\frac{\mathrm{d}\boldsymbol{j}_{\rm in}}{\mathrm{d}t}\right|_{\rm GW} = -\left.\frac{\mathrm{d}e_{\rm in}}{\mathrm{d}t}\right|_{\rm GW}\frac{e_{\rm in}}{j_{\rm in}}\hat{\boldsymbol{j}}_{\rm in}, \tag{2.28}$$

where $\mathrm{d}e_{\rm in}/\mathrm{d}t|_{\rm GW}$ is given by Eq. (1.65) and the inner semi-major axis changes according to Eq. (1.64).

Outer orbit evolution

For the evolution of the outer orbit we can safely neglect the relativistic effects and the torques emerging from the tides and stellar rotations since they are suppressed by the larger semi-major axis $a_{\rm out}$. The evolution is thus solely given by

$$\frac{\mathrm{d}\boldsymbol{j}_{\rm out}}{\mathrm{d}t} = \left.\frac{\mathrm{d}\boldsymbol{j}_{\rm out}}{\mathrm{d}t}\right|_{\rm LK,Quad} + \left.\frac{\mathrm{d}\boldsymbol{j}_{\rm out}}{\mathrm{d}t}\right|_{\rm LK,Oct}, \tag{2.29}$$

$$\frac{\mathrm{d}\boldsymbol{e}_{\rm out}}{\mathrm{d}t} = \left.\frac{\mathrm{d}\boldsymbol{e}_{\rm out}}{\mathrm{d}t}\right|_{\rm LK,Quad} + \left.\frac{\mathrm{d}\boldsymbol{e}_{\rm out}}{\mathrm{d}t}\right|_{\rm LK,Oct}, \tag{2.30}$$

$$\frac{\mathrm{d}a_{\rm out}}{\mathrm{d}t} = \left.\frac{\mathrm{d}a_{\rm out}}{\mathrm{d}t}\right|_{\rm Mass}, \tag{2.31}$$

where the LK terms are given by Eqs. (17) – (20) of Liu et al. (2015) and the mass loss term is, analogously to Eq. (2.20), given by

$$\left.\frac{\mathrm{d}a_{\mathrm{out}}}{\mathrm{d}t}\right|_{\mathrm{Mass}} = -a_{\mathrm{out}}\frac{\dot{m}_{\mathrm{out}}}{m_{\mathrm{out}}}, \tag{2.32}$$

Thus, we also do not follow the spin evolution of the outer companion. Together, Eqs. (2.4) – (2.7) and (2.29) – (2.31) constitute a coupled set of twenty differential equations (vectorial quantities counting thrice) which we numerically integrate forward in time. Simultaneously, we keep track of the evolution of the stellar masses and radii, $m_{1(2)(3)} = m_{1(2)(3)}(t)$ and $R_{1(2)} = R_{1(2)}(t)$, respectively. This is governed by the rich stellar physics describing the coevolution of the three massive stars that we implement as described in the following section.

2.1.2 Stellar evolution

In the following, we describe our treatment of stellar evolution. By default, the stars are evolved using the public stellar evolution code `Single Stellar Evolution` (`SSE`, Hurley et al., 2000). We modified this code to include up-to-date prescriptions for stellar winds, BH formation, and SN kicks and we couple it to the equations above to account for the dynamical evolution of the system.

We use metallicity-dependent stellar wind prescriptions (Vink et al., 2001). These are the same stellar evolution subroutines currently employed in other binary population synthesis codes (e.g., Belczynski et al., 2016c; Breivik et al., 2020). With these modifications, `TSE` reproduces the mass distribution for single BHs adopted in recent studies of compact object binary formation from field binaries and clusters (e.g., Belczynski et al., 2020; Rodriguez et al., 2016a; Banerjee et al., 2020; Antonini & Gieles, 2020). Optionally, `TSE` takes a mass loss dependency on the electron-scattering Eddington factor into account (Gräfener & Hamann, 2008; Gräfener et al., 2011; Vink et al., 2011; Vink, 2017; Giacobbo et al., 2018).

In `TSE`, the initial radius of each star is given by `SSE` where it is calculated from the initial mass and metallicity as in Hurley et al. (2000). By default, the initial spin for each star is taken also to be consistent with the adopted value in `SSE` where the equatorial speed of ZAMS stars is set equal to (Lang, 1992)

$$v_{\mathrm{rot},1(2)} = 330\mathrm{km\ s^{-1}}\left(\frac{m_{1(2)}}{M_\odot}\right)^{3.3}\left[15+\left(\frac{m_{1(2)}}{M_\odot}\right)^{3.45}\right]^{-1}, \tag{2.33}$$

so that the initial spin frequency becomes $\Omega_i = v_{\mathrm{rot},1(2)}/R_{1(2)}$. For this work, the spins are

assumed to be initially aligned with the orbital angular momentum of the binary.

When a star evolves to become a NS or a BH, the remnant radius is set to zero, and its mass is immediately updated. In `TSE`, the model adopted for the remnant masses is set by the code parameter `nsflag`. If `nsflag` $= 1$ the BH and NS masses are computed as in Belczynski et al. (2002); if `nsflag` $= 2$ the BH and NS masses are computed as in Belczynski et al. (2008); if `nsflag` $= 3$ they are given by the "rapid" SN prescription described in Fryer et al. (2012); and if `nsflag` $= 4$ they are described by the "delayed" SN prescription also from Fryer et al. (2012).

Given the large uncertainties in the natal kick velocities of BHs, we adopt three different models for their distributions. We assume that kick velocities are randomly oriented, then the assumed model for the BH kick velocity magnitude is set by the code parameter `bhflag`. If `bhflag` $= 0$ the natal kicks of all BHs and NSs are set to zero. In any other case we assume that NS kicks follow a Maxwellian distribution with dispersion $\sigma = 265\mathrm{km\ s^{-1}}$ (Hobbs et al., 2005). If `bhflag` $= 1$, the BHs receive the same momentum kick as NSs, i.e., the BH kick velocities are lowered by the ratio of NS mass (set to $1.5\,\mathrm{M}_\odot$) to BH mass. We will refer to them as "proportional" kicks. If `bhflag` $= 2$ we assume that the BH kicks are lowered by the mass that falls back into the compact object according to

$$v_\mathrm{k} = v_\mathrm{k,natal}(1 - f_\mathrm{fb}), \tag{2.34}$$

where f_fb is the fraction of the ejected SN mass that falls back onto the newly formed proto-compact object, which is given by the assumed SN mechanism set by the parameter `nsflag`.

What we are interested in is the change to the orbital elements due to the mass loss and natal kicks as the stars evolve towards their final states. When a remnant is formed, we extract the velocity of the natal kick from the adopted prescription. The kick is then self-consistently applied to the orbital elements of the system following Pijloo et al. (2012). Briefly, we draw a random phase from the mean anomaly and then apply the instantaneous kick, $\boldsymbol{v}_\mathrm{k}$, to the initial velocity vector of that component, $\boldsymbol{v}_0$. Thus, the new angular momentum and eccentricity vectors (using the new orbital velocity vector and the same orbital position vector) are given by

$$\boldsymbol{j}_\mathrm{new} = \frac{\mathbf{r}_\mathrm{in} \times \boldsymbol{v}_\mathrm{new}}{\sqrt{m_\mathrm{new} a_\mathrm{new}}} \tag{2.35}$$

and

$$\boldsymbol{e}_\mathrm{new} = \frac{1}{G m_\mathrm{new}} \left(\boldsymbol{v}_\mathrm{new} \times \boldsymbol{j}_\mathrm{new}\right) - \frac{\boldsymbol{r}_\mathrm{in}}{r_\mathrm{in}}, \tag{2.36}$$

where $m_{\rm new}$ is the new total mass of the binary and $\boldsymbol{v}_{\rm new} = \boldsymbol{v}_0 + \boldsymbol{v}_{\rm k}$. The new semi-major axis is

$$a_{\rm new} = \left(\frac{2}{r_{\rm in}} - \frac{v_{\rm new}^2}{G m_{\rm new}} \right)^{-1} . \tag{2.37}$$

If the kicks occur in one of the inner binary components, we must also take care of the kick imparted on the centre of mass of the binary. Thus, the change in the centre of mass velocity of the inner binary is explicitly calculated. This change is then added to the velocity arising from the BH natal kick, and applied as $\boldsymbol{v}_{\rm new}$ to the outer binary (e.g., Lu & Naoz, 2019). As a result, the orientation of the orbital plane changes. Meanwhile, it is uncertain if the spin orientation of the compact remnants changes as well. For young pulsars, Noutsos et al. (2012, 2013) found evidence that the spins align with their proper motion which could be explained by NS natal kicks defining a preferred direction for the subsequent angular momentum accretion of fallback material (Janka et al., 2022). Thus, the spin-kick correlation is expected to be stronger for higher natal kicks. Here we adopt the assumption made in the literature that natal kicks leave the spin orientations unchanged (e.g., Pijloo et al., 2012; Rodriguez et al., 2016b; Rodriguez & Antonini, 2018; Lu & Naoz, 2019).

2.1.3 Mass transfer

If a star is bound to a close companion, it can experience a set of binary interactions, including accretion of mass. Accretion onto a companion star can occur during either RLO or when material is accreted from a stellar wind. We describe below our simplified treatment of these two possible modes of accretion.

Wind accretion

The material ejected as a wind can be partly accreted by the companion star, or self-accreted by the donor star itself. Because of gravitational focusing, the accretion cross-section is generally much larger than the geometric cross-section of the accretor and it is often expressed by the Bondi-Hoyle accretion radius (Bondi & Hoyle, 1944)

$$R_{\rm acc} = \frac{2 G m_{\rm acc}}{v^2} \tag{2.38}$$

with $m_{\rm acc}$ the accretor mass and v the relative velocity between the wind and the accretor star. For a mass loss rate $\dot{m}_{\rm wind}$ and a spherically symmetric wind, the accretion rate is given by (Boffin,

2015)

$$\dot{m}_{\rm acc} = -\dot{m}_{\rm wind} \left(\frac{m_{\rm acc}}{m_{\rm don} + m_{\rm acc}} \right)^2 \left(\frac{v_{\rm orb}}{v_{\rm wind}} \right)^4 \tag{2.39}$$

where $m_{\rm don}$ is the donor mass, $v_{\rm orb}$ is the orbital velocity, and $v_{\rm wind}$ is the wind velocity.

The accretion process will affect the mass and spin of the stars, as well as the orbital parameters of the triple, e.g., Eqs. (2.20) and (2.32). However, its formulation presents a number of difficulties. First, when the wind mass losing star is the tertiary we should take into account that accretion occurs onto a binary rather than a single object, and there is no simple prescription to describe this (cf., Antoni et al., 2019). Moreover, there are major uncertainties in modeling the evolution of the binary orbit and stellar spins due to wind accretion, which would require careful geometrical considerations of how the mass flow is ultimately accreted onto the star surface (Mastrodemos & Morris, 1998; de Val-Borro et al., 2009; Perets & Kenyon, 2013). Fortunately, massive stars are characterised by high wind velocities, typically a few thousand $\rm km\ s^{-1}$ (Prinja, 1992; Crowther, 2001). Moreover, both the inner and outer orbit of the progenitors of compact object triples tend to be relatively wide – in order to avoid a merger of the inner binary during an episode of unstable mass transfer and to guarantee dynamical stability. Thus, the last factor in Eq. (2.39) generally makes the accretion rate several orders of magnitude smaller than the mass loss rate. Because in the systems we consider, wind-accretion tends to be of secondary importance and much less important than accretion by atmospheric RLO, we proceed in what follows with the assumption that changes in mass and angular momentum from material gained by a wind can be ignored, i.e., we set $\dot{m}_{\rm acc} = 0$. We redirect the reader to Hamers et al. (2021) for an approximate treatment of wind accretion in triples and higher multiplicity systems.

Roche-lobe overflow

If one of the stars in the inner binary overflows its Roche-lobe, matter can move through the first Lagrangian point and be accreted by the companion star. We assume that RLO begins when the stellar radius of an inner binary component satisfies (Eggleton, 1983)

$$R_{1(2)} > \frac{0.49 \left[m_{1(2)}/m_{2(1)} \right]^{2/3} a_{\rm in}(1-e_{\rm in})}{0.6 \left[m_{1(2)}/m_{2(1)} \right]^{2/3} + \ln \left\{ 1 + \left[m_{1(2)}/m_{2(1)} \right]^{1/3} \right\}}. \tag{2.40}$$

The theory of RLO is based on two stars in a circular orbit in which complete corotation has been achieved (Eggleton, 1983). The modelling of mass transfer in eccentric orbits is the subject of ongoing research (Dosopoulou & Kalogera, 2016b; Hamers & Dosopoulou, 2019), but remains an

elusive subject overall. For want of a more detailed treatment, when condition (2.40) is met we evolve the binary using the binary stellar evolution analogous to SSE, the code Binary Stellar Evolution (BSE, Hurley et al., 2002). Here, the binary is subject to instant synchronisation and circularises on the tidal friction timescale. The various parameters that enter in the equations of motion of the binary (e.g., K, $k_{\rm A}$, τ) are chosen to be consistent with those used in Eqs. (2.4) – (2.7). During the entire episode of mass transfer we neglect the dynamical influence of the tertiary.

Although necessarily approximate, our approach is in most cases adequate because tides generally act on a time-scale shorter than the secular evolution time-scale of the triple, quenching the dynamical influence of the tertiary star. For example, using Eq. (1.44) it is easy to show that for equal mass components, the precession of the inner binary periapsis due to tidal bulges will fully quench the LK oscillations for any $a_{\rm out}j_{\rm out}/a_{\rm in} \gtrsim 10j_{\rm in}^3/\left[f_4(1-e_{\rm in})^5\right]^{1/3}$, where $f_4 = f_4(e_{\rm in})$ is a polynomial given in Appendix A.1. Moreover, when mass transfer begins at high eccentricities, dissipative tides can become dominant very quickly, circularising the orbit and thereby reducing the dynamical effect of the tertiary.

Finally, we assume that the tertiary star overfills its Roche-lobe when (cf., Eq. (2.40))

$$R_3 > \frac{0.49{q_{\rm out}}^{2/3}}{0.6{q_{\rm out}}^{2/3} + \ln\left\{1+{q_{\rm out}}^{1/3}\right\}} a_{\rm out}(1-e_{\rm out}). \tag{2.41}$$

Currently, we do not try to model mass transfer from the tertiary to the inner binary. Thus, if the previous condition is satisfied, we simply stop the integration.

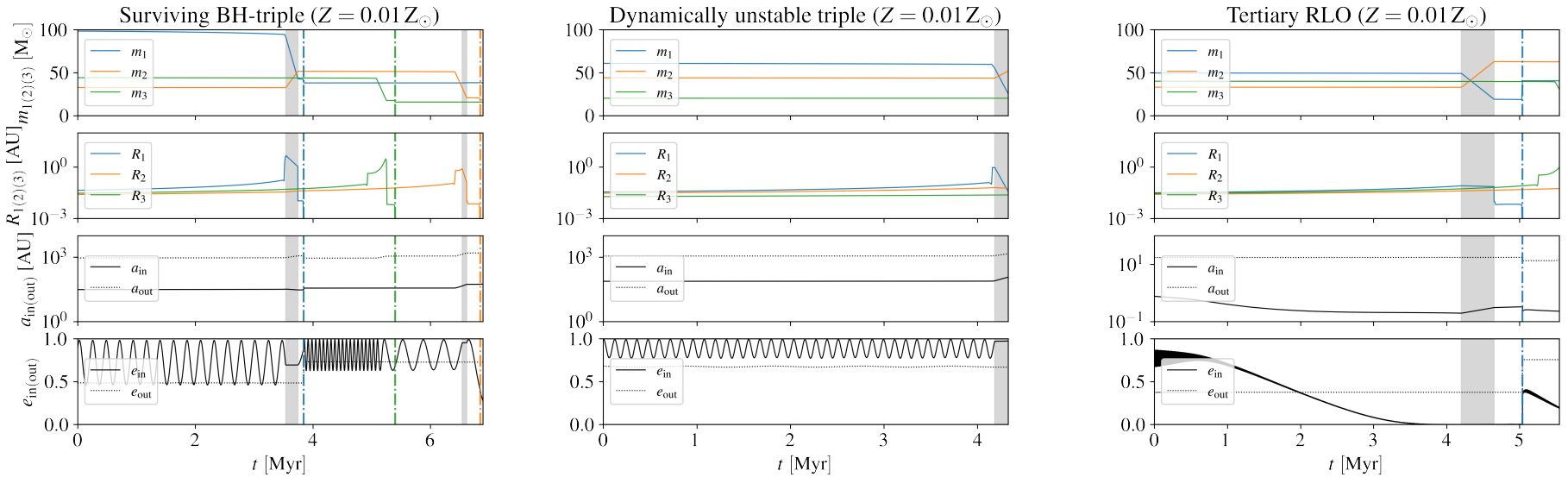

Figure 2.1. Examples of the evolution of three stellar triples. Vertical dashed lines and grey shaded regions indicate the time of compact object formation and episodes of mass transfer in the inner binary, respectively. The initial parameters of the three triples are given in Appendix A.2.

2.1.4 Coupling stellar evolution and dynamics

In the code presented in this work, stellar evolution and dynamics are coupled by using the following numerical treatment.

Because we neglect wind mass accretion, the mass and radius of each star will evolve as if they were isolated, at least until the next RLO episode occurs. Thus, we start by setting a final integration time and compute the evolution of the stellar masses and radii using SSE until this final time is reached. Simultaneously, we use these masses and radii as a function of time in Eqs. (2.4) – (2.7) to determine the evolution of the stellar orbits and spins. During the integration of the equations of motion we check whether any of the stars forms a compact object. If they do, we calculate the natal kick according to the adopted prescriptions and compute the effect of the kick on the inner and outer orbits.

Due to its lower binding energy the outer orbit is more vulnerable to disruptions than the inner one. As a consequence, there are some SN kicks which destroy the outer orbit while leaving the inner orbit intact, i.e., the inner binary loses its tertiary companion. In this case, we continue the evolution of the remaining orbit with BSE.

During the evolution, we check whether the system undergoes a phase of RLO. If mass transfer does not occur at any point during the evolution, the dynamical equations of motion are simply integrated until the required final time is reached.

If a phase of RLO occurs in the outer binary, we stop the simulation. If the mass transfer phase occurs in the inner binary instead, we pass the required stellar and orbital parameters to BSE and continue evolving the binary until the end of the mass transfer phase. During the BSE integration, appropriate prescriptions from Hurley et al. (2002) are used to identify whether the stars come into contact and coalesce, if the binary reaches a CE state, or if the mass transfer is stable. When a merger occurs, we terminate the simulation. In particular, we assume that any CE evolution that is initiated by a donor star in the Hertzsprung gap (HG) leads to a stellar merger because it is questionable whether they already developed a well-defined core-envelope structure (Belczynski et al., 2007). In the absence of a stellar core no stable binary configuration could result from a CE evolution. If the binary survives the mass transfer phase, we keep evolving the two inner stars with SSE from the end of the mass transfer phase until the final integration time, and obtain new $m_{1(2)}(t)$ and $R_{1(2)}(t)$. In this latter case, we store the orbital and stellar parameters at the time the mass transfer phase terminates and integrate Eqs. (2.4) – (2.7) from that moment on, but using the newly computed $m_{1(2)}(t)$ and $R_{1(2)}(t)$. Note that the stellar spins, $S_{1(2)}$, at the end of the mass transfer phase are assumed to be synchronised with the orbit, which is consistent with the treatment in BSE. Moreover, during the BSE integration we use Eq. (2.32) to keep track of the

evolution of $a_{\rm out}$ due to mass loss from the system.

Stopping conditions

In summary, the simulation is terminated before the final integration time in one of the following events:

1. The tertiary star initiates a mass transfer episode onto the inner binary once it fills its Roche-lobe according to Eq. (2.41).
2. The inner binary stars merge after an unstable mass transfer phase or an eccentric encounter.
3. The triple becomes dynamically unstable (see Section 2.2.6).
4. The inner orbit is disrupted due to a SN.

Either of these events leads to very different evolutionary outcomes. A tertiary RLO (i) may occur stably or initiate a CE engulfing all three stars in which a merger of two stars, chaotic ejection of one of them, or of the envelope is possible (Di Stefano, 2020a,b; Glanz & Perets, 2021; Hamers et al., 2022). Yet, modelling tertiary RLO is less understood than RLO in isolated binaries due to the additional complexity of the inner binary motion.

If the inner binary merges before the formation of compact objects (ii), a post-merger binary can form which consists of a massive post-merger star and the tertiary companion (Schneider et al., 2019, 2020; Hirai et al., 2021). If the initial triple was sufficiently compact a merging BBH might eventually from from the stellar post-merger binary (Stegmann et al., 2022a, Chapter 3).

Triples that become dynamically unstable (iii) can no longer be described by our secular approach, but enter a chaotic regime in which the ejection of one star or the merger of two become likely (Mardling & Aarseth, 2001; Petrovich, 2015; Toonen et al., 2022).

Lastly, if a SN disrupts the inner binary (iv), we expect that either the outer binary is also disrupted due to the kick imparted to the inner binary centre of mass, or the remaining inner binary star and tertiary companion subsequently evolve on a wide orbit.

2.1.5 Stellar evolution parameters

In this work, we investigate a set of different models whose parameters are summarised in Table 2.1. In any of our models we set the CE efficiency parameter $\alpha_{\rm CE}$ to 1 and the tidal lag

Table 2.1. Model parameters. In all models we also set `nsflag` $= 3$ (rapid SN prescription), $\alpha_{\rm CE} = 1$, and $\tau = 1$s.

Model	Metallicity Z $[Z_\odot]$	`bhflag`	τ [s]
`Fallback kicks`	0.01, 1.0	2	1.0
`Proportional kicks`	0.01, 1.0	1	1.0
`No kicks`	0.01, 1.0	0	1.0
`Incl. dyn. tides`	0.01, 1.0	2	See Sec. 2.1.1

time τ to $1\,\mathrm{s}$. The latter recovers well the observation of circularised inner binaries at short periods. The remnant masses prescription follows the "rapid" SN model (`nsflag` $= 3$, Fryer et al., 2012). We study the impact of natal kicks by adopting the three models `fallback kicks`, `proportional kicks`, and `no kicks` in which we set `bhflag` to 2, 1, and 0, respectively, and investigate the effect of metallicity by setting $Z = 0.01\,\mathrm{Z}_\odot$ (low metallicity) or $Z = 1.0\,\mathrm{Z}_\odot$ (high/solar metallicity). If not stated differently, the `fallback kicks` model is used as a default in the following sections.

2.1.6 Example cases

In Fig. 2.1, we show the evolution of three example systems at $Z = 0.01\,\mathrm{Z}_\odot$. The systems in the left and middle panels undergo LK oscillations, while in the right panel we see a system where the oscillations are quickly quenched by the tides acting between the inner binary stars. All three systems enter one or two phases of stable mass transfer, which are indicated by the vertical grey shaded regions. As a consequence of the mass and semi-major axes changes, the period and maximum eccentricity of the LK oscillations in the system of the left panel changes after the mass transfer episode, which produces the observed modulation. A similar effect can be seen after the formation of a BH as indicated by the vertical dashed lines.

The system in the left panel survives all peculiar steps during the stellar evolution and eventually ends up as a stable BH triple. This is not the case for the system shown in the middle panel. Here, the expansion of the inner binary during a mass transfer phase causes the triple to become dynamically unstable (see Section 2.2.6). In contrast, the system in the right panel starts relatively compact with an initial outer semi-major axis of only $a_{\rm out} \approx 17.2\,\mathrm{AU}$. This is small enough for the tertiary companion to fill its Roche-lobe during its giant phase. Then, we stop the integration for want of a more accurate treatment.

In Appendix A.2, we list the initial parameters of the three exemplary triples.

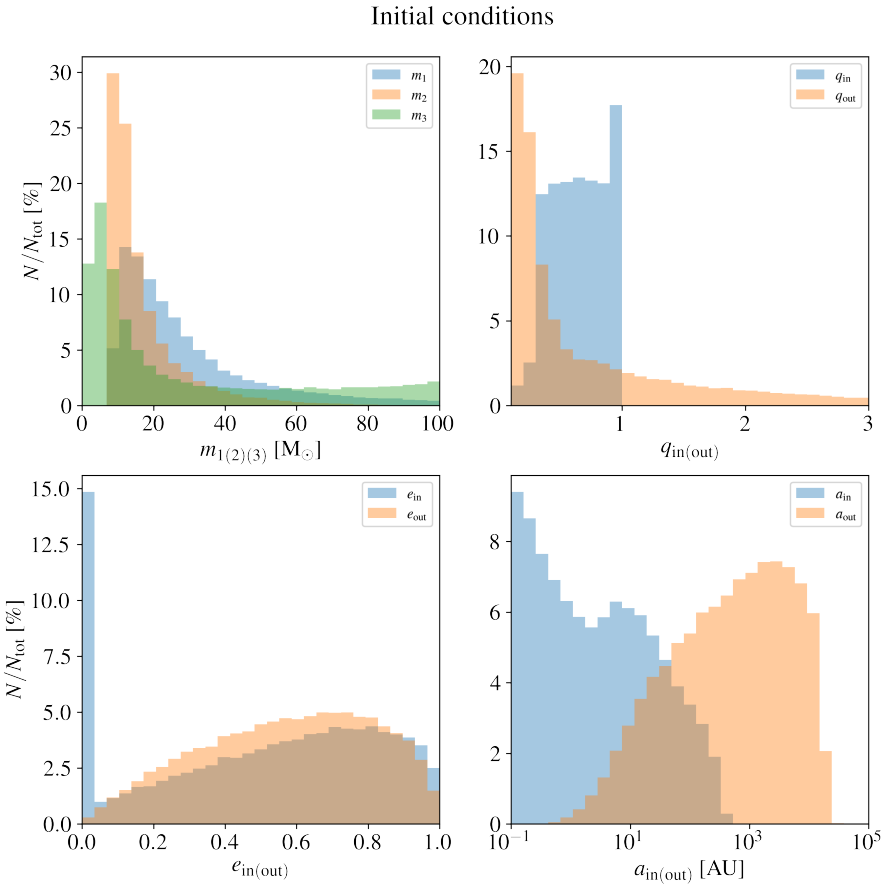

Figure 2.2. Initial conditions of the triple population. The counts N are normalised w.r.t. the total number of triples $N_{\rm tot}$ which are initially stable, detached, and whose inner binary members are massive enough to form compact objects.

2.2 Initial conditions

In the following, we describe the set-up of the initial parameter distribution of our massive stellar triple population. The initial time is chosen when the stars are on the ZAMS. Observationally, companions to massive, early-type stars were discovered by means of several techniques, e.g., radial velocity monitoring (e.g., García & Mermilliod, 2001; Sana et al., 2012; Kobulnicky et al., 2014), eclipses (e.g., Kirk et al., 2016; Soszyński et al., 2016; Pawlak et al., 2016; Moe & Di Stefano, 2015), proper motion (e.g., Lépine & Bongiorno, 2007), and interferometry (e.g., Rizzuto et al., 2013; Sana et al., 2014). For massive triples, it has been shown that the parameter distributions of early-type stars are a good indicator for the initial distribution at birth (Rose et al., 2019). For the initial parameter distribution of our population we follow Moe & Di Stefano (2017) who compiled a variety of previous surveys.

Accordingly, the masses and mass ratios, eccentricities, and orbital periods are not statistically independent from each other. Instead, they show important correlations across different periods,

e.g., an excess of nearly-equal mass ratios ("twins") and circularised orbits at short periods whereas the properties of two stars are more consistent with a random pairing process toward long periods.

Specifically, we adopt the following sampling procedure which results in the marginalised distributions shown in Fig. 2.2. At first, we propose an inner binary from the joint probability distribution

$$f(m_1, m_2, P_{\rm in}, e_{\rm in}) = f(m_1) f(P_{\rm in}|m_1) f(m_2|m_1, P_{\rm in}) f(e_{\rm in}|m_1, P_{\rm in}), . \tag{2.42}$$

Afterwards, an outer orbit is repeatedly drawn from the distribution

$$f(m_3, P_{\rm out}, e_{\rm out}|m_1) = f(P_{\rm out}|m_1) f(\tilde{q}_{\rm out}|m_1, P_{\rm out}) f(e_{\rm out}|m_1, P_{\rm out}), \tag{2.43}$$

with $\tilde{q}_{\rm out} = m_3/m_1$, until the triple system is hierarchically stable and detached (see below).

This procedure recovers the observed distributions of triples in which m_1 is the largest mass of the triple stars, i.e., where it is part of the inner binary. Unfortunately, triples where the tertiary companion is the most massive star completely elude detection since it is difficult to resolve additional companions to the less massive star of a wide orbit. In order to model those kind of systems we agnostically draw in every third system the tertiary mass from a uniform distribution with a lower limit of m_1 and the orbital parameters from

$$f(P_{\rm out}, e_{\rm out}|m_3) = f(P_{\rm out}|m_3) f(e_{\rm out}|m_3, P_{\rm out}). \tag{2.44}$$

The triples proposed in this way are only retained if they are hierarchically stable and detached which naturally skews the final inner and outer orbital distributions. The marginal distributions are as following (Moe & Di Stefano, 2017). For convenience we define $m_{\rm p} = \max(m_1, m_3)$ to be the largest mass of the triple.

2.2.1 Primary mass distribution $f(m_1)$

The primary star is initially the more massive component of the inner binary. We draw its mass between 8 and $100\,{\rm M}_\odot$ from the canonical initial mass function (Kroupa, 2001) which is described by a single power law $f(m_1){\rm d}m_1 \propto m_1^\alpha {\rm d}m_1$ with exponent $\alpha = -2.3$. In general, the canonical initial mass function describes the mass distribution of all stars that formed together in one star-forming event. Note that it does not necessarily coincide with the initial mass distribution of the primaries which is skewed towards larger masses. However, for the *massive* primaries under consideration both are approximately equal (Kroupa et al., 2013, Section 9).

2.2.2 Period distributions $f(P_{\rm in(out)}|m_{\rm p})$

The inner and outer periods $P_{\rm in(out)}$ are technically proposed from the same conditional distribution $f(P_{\rm in(out)}|m_{\rm p})$ in the range $0.2 \leq \log_{10}(P_{\rm in(out)}/{\rm day}) \leq 5.5\,(8.0)$. This distribution function is slightly bimodal with one dominant peak at short periods, $\log_{10}(P_{\rm in(out)}/{\rm day}) < 1$ (consistent with Sana et al., 2012), and another at $\log_{10}(P_{\rm in(out)}/{\rm day}) \approx 3.5$. Discarding hierarchically unstable triples (see Section 2.2.6), roughly 41% (0%) of the systems have inner (outer) periods below $10\,{\rm days}$, 86% (10%) below $10^3\,{\rm days}$, and 99% (48%) per cent below $10^5\,{\rm days}$. After specifying the mass ratios (see below), the resulting semi-major axis distributions are shown in the lower right panel of Fig. 2.2.

2.2.3 Inner (outer) mass ratio distribution $f(q_{\rm in}(\tilde{q}_{\rm out})|m_{\rm p}, P_{\rm in(out)})$

The mass ratio distributions are described by an underlying broken power-law with two slopes $\alpha = \alpha_{\rm smallq}(m_{\rm p}, P_{\rm in(out)})$ and $\alpha_{\rm largeq}(m_{\rm p}, P_{\rm in(out)})$ for $0.1 \leq q < 0.3$ and $q \geq 0.3$, respectively. This is shown in the upper right panel of Fig. 2.2. Small inner mass ratios are further reduced since we only retain secondary stars with a mass $m_2 \geq 8\,{\rm M}_\odot$. Moreover, observational surveys of massive primaries have discovered an excess fraction of twins (Tokovinin, 2000; Pinsonneault & Stanek, 2006), i.e., companions with a mass similar to their primary ($q_{\rm in} > 0.95$), if their orbital period is very short $\log_{10}(P_{\rm in}/{\rm day}) \lesssim 1$, which gives rise to the large peak in the rightmost bin of the inner mass ratio distribution. In turn, the outer companion masses at long orbital periods are more consistent with a random pairing from the initial mass function (Moe & Di Stefano, 2017).

Since we are interested in inner binary stars which could form compact objects, their masses are restricted to $m_{1,2} \geq 8\,{\rm M}_\odot$. This restriction does not apply to the tertiary companion. Instead, we take any mass down to $m_3 = 0.1\,{\rm M}_\odot$ into account.

2.2.4 Inner (Outer) eccentricity $f(e_{\rm in(out)}|m_{\rm p}, P_{\rm in(out)})$

The inner (outer) eccentricity $e_{\rm in(out)}$ is drawn from the conditional distribution $f(e_{\rm in(out)}|m_{\rm p}, P_{\rm in(out)})$ between 0 and 1. The distribution is fitted by an underlying power-law with exponent $\alpha = \alpha(P_{\rm in(out)})$ described as (Moe & Di Stefano, 2017)

$$\alpha = 0.9 - \frac{0.2}{\log_{10}(P_{\rm in}/{\rm day}) - 0.5}. \tag{2.45}$$

In general, a power-law diverges at the lower boundary $e_{\rm in(out)} = 0$ and cannot be interpreted as a probability density function if $\alpha \leq -1$. Here, this is the case if $\log_{10}(P_{\rm in}/{\rm day}) \lesssim 0.6$. For these

short periods it is reasonable to assume that all orbits were circularised due to tidal interactions (e.g., Hut, 1981; Zahn, 1989; Eggleton & Kiseleva-Eggleton, 2001).

For longer periods, the power-law exponent increases monotonically where there is a narrow window, $0.6 \lesssim \log_{10}(P_{\rm in}/{\rm day}) \lesssim 0.7$, for which $-1 < \alpha < 0$ (i.e., the eccentricity distribution is skewed towards small values) and $\alpha \geq 0$ for $\log_{10}(P_{\rm in}/{\rm day}) \gtrsim 0.7$ (i.e., skewed towards large values). For long periods, the power-law approaches a thermal distribution. Note that Moe & Di Stefano (2017) imposed an approximate upper limit $e_{\rm max}(P_{\rm in(out)}) < 1$ for the eccentricity above which a binary is semi-detached or in contact at periapsis. Here, we explicitly check for each system whether one of the three stars initially fills its Roche-lobe at periapsis and reject them as described below.

2.2.5 Orbital angles

We sample the initial values of the two arguments of periapsis of the inner and outer orbit and their relative inclination $i_{\rm tot}$ from isotropic distributions. The longitudes of the ascending nodes are "eliminated" by setting their difference to π (see Chapter 1, Naoz et al., 2013a).

Our assumption for the inclination distribution is uniformative since there exists no observational evidence about the mutual inclination $i_{\rm tot}$ for massive triples. Meanwhile, Borkovits et al. (2016) found all compact solar-type triples within $a_{\rm out} < 10\,{\rm AU}$ have $i < 60°$, and the majority had $i < 20°$. Similarly, Tokovinin (2017) found nearly all triples with $a_{\rm out} < 50\,{\rm AU}$ were prograde ($i < 90°$), and solar-type triples had random orientations only beyond $a_{\rm out} > 10^3\,{\rm AU}$. However, he did note that more massive triples may be more misaligned, i.e., A/early-F triples achieved random orientations beyond $a_{\rm out} > 100\,{\rm AU}$ (instead of $> 10^3\,{\rm AU}$). If the overall preference of close solar-type triples for prograde inclinations turns out to persist in future observations of massive triples our isotropic assumption must be skewed towards small angles beyond the Kozai regime (cf., Section 2.1.1).

2.2.6 Discarded systems

Triples that are proposed according to the sampling procedure described above are discarded if they are dynamically unstable, if at least one star fills its Roche-lobe, or if the inner binary members are not massive enough to form compact objects ($m_{1(2)} < 8\,{\rm M}_\odot$; see Toonen et al. (2020) for a study with less massive inner binaries). For the former two criteria we reject all

systems that initially satisfy either

$$\frac{a_{\rm out}(1-e_{\rm out})}{a_{\rm in}} < 2.8\left[\left(1+\frac{m_3}{m_{\rm in}}\right)\frac{1+e_{\rm out}}{\sqrt{1-e_{\rm out}}}\right]^{2/5}, \tag{2.46}$$

or Eqs. (2.40) and (2.41) (Mardling & Aarseth, 2001; Eggleton, 1983; Hamers & Dosopoulou, 2019).

2.2.7 Drawbacks in initial conditions

Most previous population synthesis studies assume (log-)uniform initial distributions of the inner and outer mass ratios, orbital periods, semi-major axes, or eccentricities (e.g., Antonini et al., 2017; Silsbee & Tremaine, 2017; Rodriguez & Antonini, 2018; Fragione & Kocsis, 2020; Hamers et al., 2022). Typically, a mutual dependency of the orbital parameters is introduced by discarding initially unstable or Roche-lobe filling systems, which, e.g., removes systems with relatively small inner semi-major axes and large inner eccentricities (Antonini et al., 2017; Toonen et al., 2020). The drawback of this procedure is that it fails at reproducing the known parameter distributions of the inner binaries. For example, consider a model in which the inner orbital periods are drawn from a given distribution that is inferred by observations (e.g., Sana et al., 2012), whereas the outer semi-major axis distribution is uninformative (e.g., log-uniform), reflecting our poor statistics on wide (outer) binaries. A large number of triples will be discarded based on Eq. (2.46) because they are dynamically unstable. As a consequence, the resulting orbital distribution of the inner binaries will deviate from the observationally motivated model that was assumed in the first place. Moreover, the adopted method does not take into account the observed correlation between the different orbital parameters of early-type stars.

The sampling procedure presented in this work aims to improve previous work by reproducing some of the statistical features identified by observations (Moe & Di Stefano, 2017). Thus, the novel feature of our method is that it takes into account the observed mutual correlation between orbital parameters. Moreover, the distributions of the inner binary properties in our triple systems are consistent with observations since for a given inner binary we propose a tertiary until the triple satisfies the stability criteria. But, we remain speculative regarding triples in which the most massive component is the tertiary star and for which there are no observations. Since the LK effect is stronger for larger tertiary masses (cf., Chapter 1), this introduces some uncertainty to the total fraction of systems in which a tertiary can dynamically perturb the inner binary.

Table 2.2. Upper half: Fraction of triple evolutionary outcomes for our different models at sub-solar and solar metallicity. The last three columns refer to the fraction of surviving systems that harbour a BBH ($\Gamma_{\rm BBH}$), NSBH ($\Gamma_{\rm NSBH}$), and BNS ($\Gamma_{\rm BNS}$) in the inner binary. For those and for the stellar mergers we provide the fraction of systems that retain their tertiary companion plus ("+") the systems that lose it in a SN explosion, i.e., keep evolving as isolated inner binaries. Lower half: Evolutionary outcomes of isolated inner binaries when no tertiary companion is included from the beginning of the simulation.

Z [$Z_\odot$]	Model	$N_{\rm tot}$	Fraction of evolutionary outcomes $N/N_{\rm tot}$ [%]						
			Orbital disruption	Stellar merger	Dynamically unstable	Tertiary RLO	$\Gamma_{\rm BBH}$	$\Gamma_{\rm NSBH}$	$\Gamma_{\rm BNS}$
0.01	Fallback kicks	71936	49.72	18.70 + 9.90	7.15	4.86	3.56 + 5.89	0.05 + 0.15	0.00 + 0.02
	Proportional kicks	65858	53.93	15.04 + 13.25	7.21	4.83	0.29 + 5.31	0.02 + 0.13	0.00 + 0.00
	No kicks	42891	9.57	28.81 + 23.89	9.93	5.04	5.27 + 7.68	1.14 + 7.34	0.10 + 1.25
	Incl. dyn. tides	9746	49.39	19.75 + 8.93	7.81	4.77	3.53 + 5.60	0.03 + 0.18	0.00 + 0.00
1.0	Fallback kicks	104643	57.92	17.19 + 9.09	9.45	5.52	0.26 + 0.54	0.00 + 0.03	0.00 + 0.00
	Proportional kicks	75607	59.64	15.77 + 9.96	9.05	5.53	0.00 + 0.04	0.00 + 0.00	0.00 + 0.00
	No kicks	59020	9.47	33.28 + 23.26	14.26	5.79	1.74 + 2.71	1.37 + 5.79	0.14 + 2.18
	Incl. dyn. tides	14973	55.77	19.66 + 8.06	10.50	5.20	0.29 + 0.51	0.00 + 0.02	0.01 + 0.00
0.01	Fallback kicks	49598	58.49	30.20			11.11	0.19	0.02
	Proportional kicks	49614	63.24	29.59			7.00	0.15	0.01
	No kicks	49705	11.33	62.88			14.89	9.34	1.56
1.0	Fallback kicks	47848	67.86	31.40			0.73	0.00	0.00
	Proportional kicks	47883	69.83	30.16			0.00	0.00	0.00
	No kicks	47789	9.75	74.35			4.54	8.83	2.53

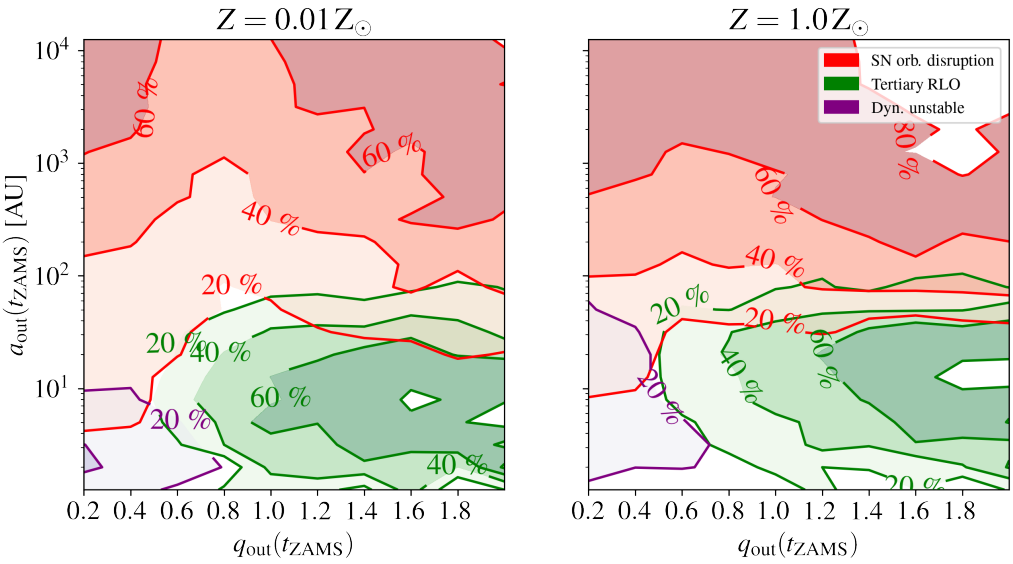

Figure 2.3. Probability for evolutionary outcomes as a function of the initial (ZAMS) outer mass ratio $q_{\rm out} = m_3/m_{\rm in}$ and outer semi-major axis $a_{\rm out}$ at $Z = 0.01\,{\rm Z}_\odot$ (left panel) and $Z = 1.0\,{\rm Z}_\odot$ (right panel) in the `fallback kicks` model. For a given $q_{\rm out}$ and $a_{\rm out}$, the contours correspond to the fraction of triples that achieve a particular outcome.

2.3 Results

2.3.1 Evolutionary outcomes

After generating our initial conditions as described above, we evolve the systems forward in time until one of the following outcomes is achieved:

(i) The inner orbit is disrupted due to a SN;

(ii) The system becomes dynamically unstable;

(iii) The tertiary companion fills its Roche-lobe (tertiary RLO);

(iv) The inner binary stars merge;

(v) The inner binary becomes a DCO and the tertiary is lost in a SN explosion;

(vi) The system becomes a stable triple in which the inner binary is a DCO. The tertiary companion can be either another compact object or a low mass star that will neither undergo a SN nor fill its Roche-lobe in its following evolution.

In Table 2.2 we provide the fractions of evolutionary outcomes for the different population models. In case (iv), we consider any merger that involves a stellar component, i.e., either mergers

of two stars or of a star and a compact object. In the latter case, the compact object enters the envelope of the companion star and sinks to its core before the envelope could be ejected. For case (v) and (vi), we distinguish between systems that end up harbouring a BBH, NSBH, or BNS in the inner binary. An example system of case (vi) is shown in the left panel of Fig. 2.1.

For comparison, Table 2.2 also provides the fractions of orbital disruptions, stellar mergers, and surviving systems when no tertiary companion was included at all. This isolated inner binary population is evolved with `BSE`. We will compare in more detail the results from the binary and the triple populations in Section 2.3.2.

In any of our models, we find that the majority of systems are either disrupted (case (i)) or that the inner binary components merge (case (iv)). Stellar mergers in triples have been extensively studied in previous work (Antonini & Perets, 2012; Prodan et al., 2015; Stephan et al., 2016; Toonen et al., 2018; Stephan et al., 2019; Toonen et al., 2022). For example, it has been suggested that the resulting merger product could explain the observation of blue straggler stars in globular clusters (Perets & Fabrycky, 2009; Naoz & Fabrycky, 2014; Antonini et al., 2016b). The merger process itself may give rise to a luminous red nova (e.g., Tylenda & Kamiński, 2016; MacLeod et al., 2017; Blagorodnova et al., 2017; Pastorello et al., 2019). It is expected that the merger star undergoes a brief phase with a bloated envelope (Suzuki et al., 2007; Schneider et al., 2020). If the outer orbit is sufficiently tight, it may be partially or entirely enclosed by the bloated star. This can lead to transient phenomena as the tertiary companion plunges into the enlarged envelope (Portegies Zwart & van den Heuvel, 2016; Hirai et al., 2021). Moreover, a sufficiently tight tertiary companion could co-evolve with the merger product star of the inner binary to form a bound (merging) BBH (Stegmann et al., 2022a).

The fraction of surviving systems (i.e., cases (v) and (vi)) depends on the kick prescription, metallicity, and the nature of the compact objects to be formed. It is the largest if `no kicks` are considered and the lowest for the `proportional kicks` which generally lead to the fastest kick velocities. Additionally, the number of surviving systems decreases toward solar metallicity where the stellar winds loosen the orbits and less massive remnants are formed which experience stronger natal kicks in the `fallback kicks` model. Lastly, NSs experience stronger natal kicks than BHs, making the NSBH and BNS a subdominant population in the kick models compared to BBHs. In all models, we find that the fraction of surviving DCOs that lost their tertiary companion (i.e., case (v)) is higher than those that retain it and end up as stable triples (i.e., case (vi)).

In Fig. 2.3, we plot the evolutionary outcomes of triples as a function of the initial values of $q_{\rm out}$ and $a_{\rm out}$, for the `fallback kicks` model. The contours correspond to the probability that: at least one member of the triple is ejected through a SN, case (i) or (v), the system becomes dynamically unstable, case (ii), or the tertiary undergoes RLO, case (iii), after they started from

a given point in the plane. Clearly, there is a well-defined mapping between the final evolutionary outcomes and the initial properties of the tertiary companion.

The red contours in Fig. 2.3 show that disruptions due to a SN occur mostly for systems with a large $a_{\rm out}$ since tertiaries on wider orbits are more easily unbound by a natal kick. Below $q_{\rm out} \approx 0.5$, we find that more than $50\,\%$ of the systems are disrupted if $a_{\rm out} \gtrsim 400\,{\rm AU}$. This primarily occurs due to a SN explosion in one of the inner binary components. At solar metallicity the kicks in these SNe are typically high enough to unbind both orbits. In contrast, if the inner SN occurs in a metal-poor and sufficiently hierarchical triple ($a_{\rm out}/a_{\rm in} \gtrsim 10^3$), it cannot easily disrupt the compact inner binary, but only the loosely bound outer orbits by sufficiently shifting the inner binary centre of mass. Above $q_{\rm out} \gtrsim 0.5$, disruptions occur primarily due to a SN explosion of the initially most massive tertiary companion which unbinds the outer orbit while leaving the inner orbit bound.

The purple contours in Fig. 2.3 represent systems that become dynamically unstable according to Eq. (2.46). While reaching this regime is achieved or facilitated by the expansion of the inner orbit due to stellar winds from metal-rich binary members or, more rarely, due to a non-disruptive SN, a large number of systems at both metallicities become unstable during a RLO in the inner binary. Typically, the first phase of RLO is initiated by the primary star which expands more rapidly than its secondary companion. During the subsequent mass transfer phase, the inner binary mass ratio inverts, allowing $a_{\rm in}$ to grow by a factor $\sim \mathcal{O}(1)$ (Eggleton, 2006). Thus, triples with a close tertiary companion (preferentially $a_{\rm out} \lesssim 10\,{\rm AU}$) become dynamically unstable, leading to a chaotic evolution in which the ejection or collision of the stars is likely. An example of this evolution is presented in the middle panel of Fig. 2.1.

The green contours in Fig. 2.3 represent systems in which the tertiary companion fills its Roche-lobe according to Eq. (2.41). An example case is shown in the right panel of Fig. 2.1. In general, this occurs when the tertiary companion is close ($a_{\rm out} \lesssim 10^2\ {\rm AU}$) and relatively massive ($q_{\rm out} \gtrsim 0.5$). Outside that parameter region, the radius of the tertiary star is either too small to fill its Roche-lobe, the inner binary becomes unstable, or undergoes a collision before the tertiary star fills its Roche-lobe. The subsequent evolution of the inner binaries might be significantly affected by the mass donated by the tertiary star. For instance, if the inner binary stars become compact objects, it is expected that accretion will increase and equalise the component masses leading to a reduced merger time and, if present, transforming a NS into a BH (Di Stefano, 2020b). If the tertiary mass transfer is unstable, a CE encompassing all three components will drain a large amount of energy and angular momentum of the orbits and allow for a diverse set of outcomes, including the merger of the inner binary and a chaotic evolution leading to the ejection of one component (Glanz & Perets, 2021). However, given the uncertainty related to mass transfer between just two stars, we opt for stopping the integration of systems when the

tertiary fills its Roche-lobe. For the `fallback kicks` model, we find that 5.5% (1.2%) of the inner binaries at low (high) metallicity develop a BH component before the tertiary fills its Roche-lobe. Those binaries may give rise to an X-ray signal as they accrete matter from the tertiary. Meanwhile, 0.3% (0.4%) developed a NS.

In summary, a stellar triple has to circumvent a number of defeating events in order to form a stable triple with an inner DCO. Those events demarcate distinct regions in the orbital parameter space. Most frequently, the triples are either disrupted by strong natal kicks or due to a stellar merger that takes place in the inner binary. In the following section, we will focus on the orbital properties of the surviving systems.

2.3.2 Orbital properties of the surviving systems

In this section, we investigate the properties of systems in which the inner binary becomes a DCO (case (v) and (vi) above).

In Table 2.3, we give the fraction of surviving triples which are accompanied by a low-mass star and those in which the tertiary is a compact object. In any model, the number of BBHs in the inner binary which are accompanied by another BH is roughly equal or dominate those with a low-mass star by a factor of four to five. No surviving triple was found with a NS in the outer orbit. Table 2.3 gives those systems in which the tertiary is still dynamically relevant at the end of the simulation and could possibly affect the following evolution of the inner DCO through the LK mechanism. At low metallicity, we find that the tertiary perturbation is suppressed by the inner binary's Schwarzschild precession, i.e., $\pi t_{\rm 1PN}/j_{\rm in} t_{\rm LK} \lesssim 1$, in a significant portion of the triples, e.g. $46\,\%$ in the `fallback kicks` model. At solar metallicity, almost all surviving triples ($88\,\%$ in the `fallback kicks` model) have a dynamically important tertiary. Interestingly, in the models in which we apply a finite kick to the compact objects we find no triples with an inner NS component and in which the tertiary is still dynamically relevant. We conclude that the LK mechanism is unlikely to produce any compact object binary merger in which one of the inner components is a NS.

In Figures 2.4 and 2.5, we plot the orbital parameters of the surviving systems in our models for $Z = 0.01\ \mathrm{Z}_\odot$ and $1.0\,\mathrm{Z}_\odot$ in the `fallback kicks` model, respectively. We distinguish between DCOs which are either still accompanied by a tertiary low mass star or compact object (orange histograms), or which end up isolated (blue histograms). In either case, the large majority of inner binaries are BBHs (see Table 2.2).

At $Z = 0.01\,\mathrm{Z}_\odot$, the mass distribution of the primary component of the inner binary (upper left panel) peaks at $\simeq 20\,\mathrm{M}_\odot$ and extends to $\simeq 40\,\mathrm{M}_\odot$. The cut-off at $\simeq 40\,\mathrm{M}_\odot$ is partly because

we adopted an initial maximum component mass of $100\,\mathrm{M}_\odot$. Extending the initial mass function above this mass value is unlikely to significantly change the overall shape of the mass distributions because such massive stars are very rare. Moreover, pair-instablity SN will suppress the formation of BHs more massive than $50^{+20}_{-10}\,\mathrm{M}_\odot$ (e.g., Belczynski et al., 2016b; Spera & Mapelli, 2017; Giacobbo et al., 2018).

At solar metallicity, $Z = 1.0\,\mathrm{Z}_\odot$, the primary mass distribution is significantly different. Stronger wind-mass loss prior to BH formation suppresses the formation of BHs with a mass above about $15\,\mathrm{M}_\odot$ (Fryer et al., 2012; Spera et al., 2015). The pronounced peak at $8\,\mathrm{M}_\odot$ primarily comes from BHs formed by 25 – $35\,\mathrm{M}_\odot$ stars and initially more massive stars (45 – $60\,\mathrm{M}_\odot$) which lost additional mass in some mass transfer episode. A secondary peak at $13\,\mathrm{M}_\odot$ relates to initially very massive stars ($\gtrsim 80\,\mathrm{M}_\odot$) which remain detached from their companion.

At both metallicities, the resulting mass ratio distribution shows a clear preference for equal masses, $q_\mathrm{in} \approx 1$, but otherwise differ significantly. At solar metallicity, the mass distribution of the secondary BH also shows two peaks at $8\,\mathrm{M}_\odot$ and $13\,\mathrm{M}_\odot$. Consequently, the mass ratio shows a secondary peak at $q \approx 8\,\mathrm{M}_\odot/13\,\mathrm{M}_\odot \approx 0.6$. In contrast, both BH component masses at low metallicity follow a much broader distribution leading to a smooth decrease of mass ratios down to $q_\mathrm{in} \approx 0.3$.

Compared to the parent distributions (see Fig. 2.2), the inner and outer semi-major axes of the surviving triples are significantly changed because of systems that become dynamically unstable or merge, and by inner binary interactions, and at high metallicity by stellar winds. At both metallicities, a large fraction of inner binaries are prone to merge during stellar evolution and, if they are accompanied by a nearby tertiary star, to be removed due to dynamical instability or a tertiary RLO. Nonetheless, small values $a_\mathrm{in} \lesssim 10^{-1}\,\mathrm{AU}$ are recovered in the metal-poor population because of systems in which the inner binary semi-major axis shrinks due to a CE phase, leading to a final distribution with approximately the same median value $\bar{a}_\mathrm{in} \approx 1$–$2\,\mathrm{AU}$ as the initial distribution. At solar metallicity instead, the vast majority of inner binaries that undergo a CE phase merge. Moreover, the orbital expansion driven by the stronger stellar winds shifts the inner semi-major axis of surviving systems to higher values, with a median $\bar{a}_\mathrm{in} \approx 200\,\mathrm{AU}$. Likewise, the final value of a_out is on average larger than its initial value due to the removal of close tertiaries which induce dynamical instability or fill their Roche-lobe and due to stellar winds of metal-rich stars. As a result, the medians of a_out increase from an initial $\sim 500\,\mathrm{AU}$ to $\sim 2\times10^3\,\mathrm{AU}$ and $\sim 2\times10^4\,\mathrm{AU}$ at $Z = 0.01\,\mathrm{Z}_\odot$ and $Z = 1.0\,\mathrm{Z}_\odot$, respectively.

We find that $21\,\%$ of the surviving triples at $Z = 0.01\,\mathrm{Z}_\odot$ experience a phase of CE evolution prior to the formation of the inner DCO. At solar metallicity this is the case for none of the survivors. The zero fraction of systems that survive a CE phase at high metallicity is caused by

the rapid expansion of metal-rich stars in the HG that initiate a CE, leading to stellar mergers due to the absence of a well-developed core-envelope structure. In contrast, metal-poor stars remain relatively compact in the HG but expand more significantly in the subsequent stellar evolution (Klencki et al., 2020). Consequently, a larger fraction of donor stars at lower metallicities initiate a CE during the post-HG evolution which allows for successful envelope ejection. The efficient inspiral and circularisation during a CE phase leads to low values of $a_{\rm in}$ and $e_{\rm in}$, although a small residual eccentricity can be attained during a second SN. This type of evolution produces two characteristic features in the distributions shown in Figures 2.4: the peak near $e_{\rm in} \approx 0$ seen in the bottom-left panel; and the presence of DCOs at relatively small semi-major axis value, $a_{\rm in} \lesssim 1{\rm AU}$. As a consequence of the decreasing $a_{\rm in}$, we find that $\pi t_{\rm 1PN}/j_{\rm in} t_{\rm LK} < 1$ for most of these triples, as shown in the bottom-right panel. Thus, the dynamical influence of the tertiary is expected to be fully negligible for the subsequent evolution of virtually all DCOs formed from binaries that experience a CE phase.

Regarding the DCOs that lost their tertiary companion (blue histograms in Figures 2.4 and 2.5), we find a much larger fraction that underwent a CE evolution and end up at relatively low values of $a_{\rm in}$ and $e_{\rm in}$ compared to the triples that retain their companion. We use Eq. (1.66) to compute the fraction of isolated DCO mergers. Based on the orbital properties at the time when the DCO is formed, we find $2.2\,\%$ ($0.16\,\%$) BBHs, $0.04\,\%$ ($0.03\,\%$) NSBHs, and $0.001\,\%$ ($0.01\,\%$) BNSs with $\tau_{\rm coal} < 10^{10}\,{\rm yr}$ at low (high) metallicity in the `fallback kicks` model. In the `no kicks` model we have $3.0\,\%$ ($0.24\,\%$) BBHs, $0.14\,\%$ ($0.04\,\%$) NSBHs, and $0.14\,\%$ ($0.4\,\%$) BNSs and in the `proportional kicks` $1.9\,\%$ ($0.14\,\%$) BBHs, $0.04\,\%$ ($0.006\,\%$) NSBHs, and $0.003\,\%$ ($0.017\,\%$) BNSs.

It is useful to compare the distribution of all DCOs formed in the triple population to those that formed from an equivalent isolated binary population, i.e., binaries that evolve without an outer companion from the beginning. To this end, we evolve the same inner binaries of our triple population with `BSE` and give the fractions of different evolutionary outcomes in Table 2.2. Figures 2.6 and 2.7 show the orbital properties of the DCOs in the two populations for the `fallback kicks` model. Overall, the number of surviving DCOs from the triple population is smaller due to systems that become dynamically unstable or whose integration is terminated due to a tertiary RLO. Yet, the overall shape of the parameter distributions is similar. Likewise, in the other kick models we find no significant differences between the shape of the parameter distributions between the binary and triple population models. This suggests that the presence of a tertiary companion does not significantly affect the final orbital distribution of the DCOs formed in our models.

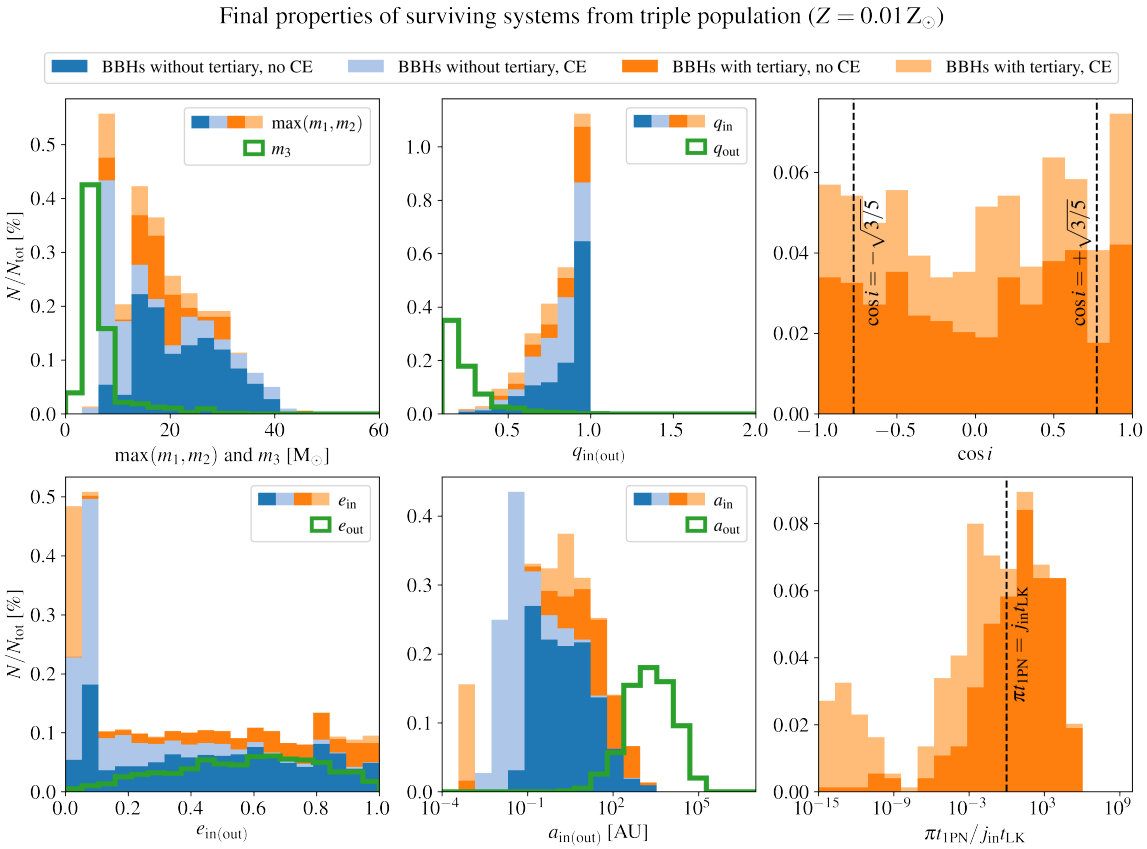

Figure 2.4. Final orbital properties of surviving systems after a BBH has formed in the inner binary in the `fallback kicks` model. By that time, the orange systems are still accompanied by a tertiary which is either a compact object or a low mass star and whose properties are shown in green. The blue BBHs have lost their tertiary companion. For both groups we show the inner binaries that undergo and survive a CE using light colours. Blue and orange contributions are stacked.

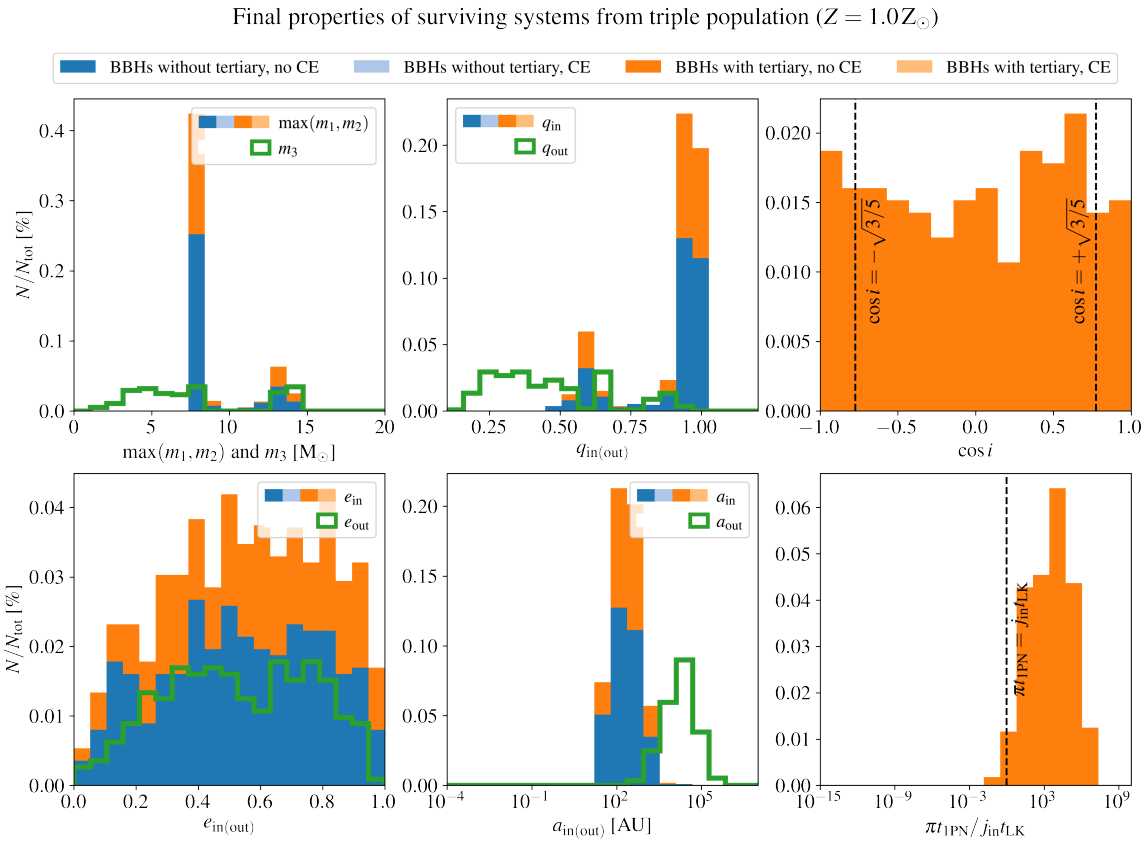

Figure 2.5. Same as Fig. 2.4 for $Z = 1.0\,Z_\odot$.

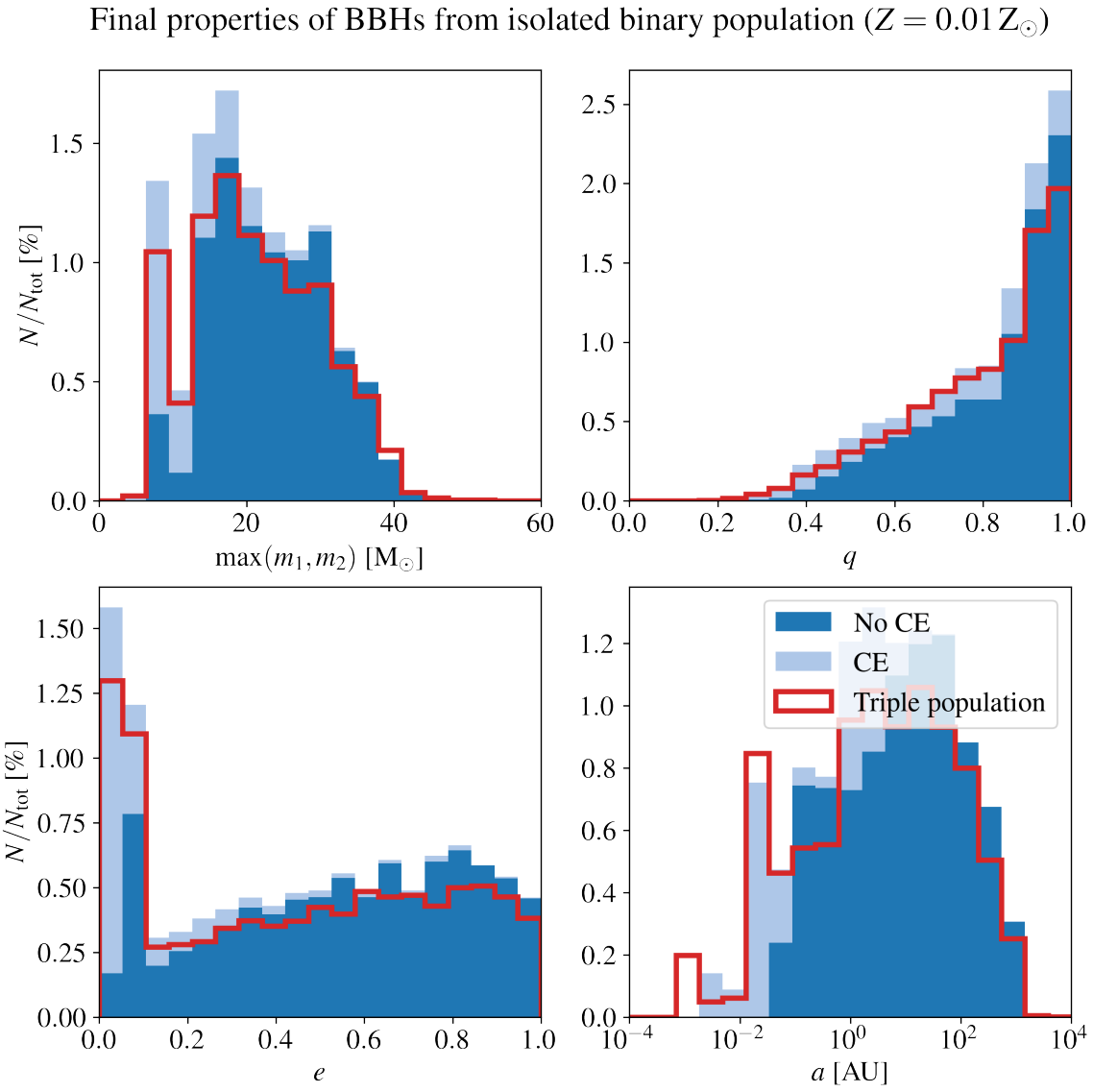

Figure 2.6. Final orbital properties of BBHs which are formed from an isolated binary population. The population is initially identical to the inner binaries of our triples. We distinguish between binaries that undergo and survive a CE evolution and those which do not (no CE). For comparision, we also show the distribution of the inner BBHs that form in the triple population in the `fallback kicks` model (red), cf., Fig. 2.4.

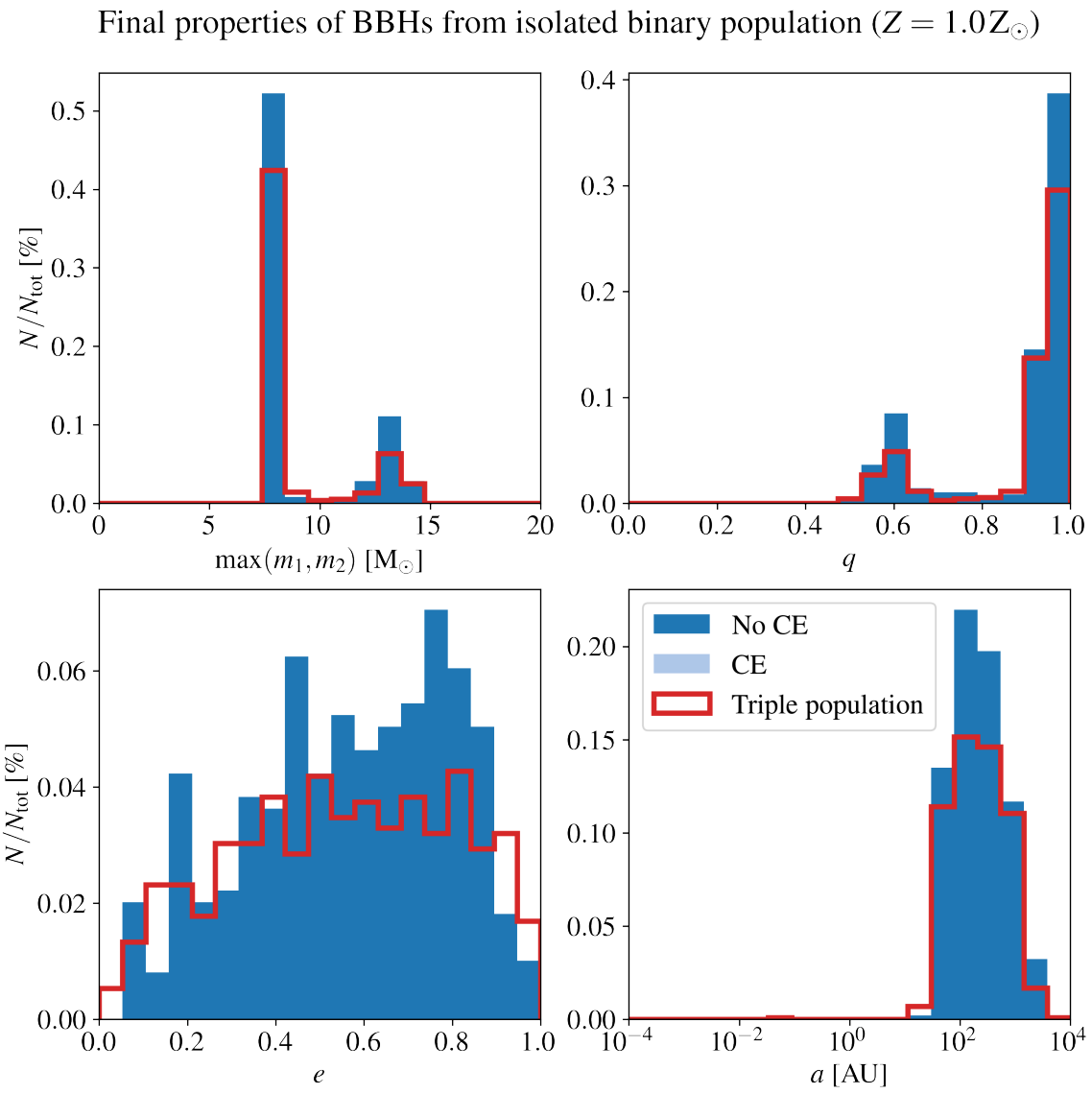

Figure 2.7. Same as Fig. 2.6 for $Z = 1.0\,Z_\odot$.

Table 2.3. Detailed fraction of surviving triples for our different models at sub-solar and solar metallicity. The number of systems harbouring a DCO in the inner binary as reported in Table 2.2 are further refined by distinguishing between triples in which the tertiary companion is a low-mass star ("+Star") and a BH ("+BH"). There is no surviving triple with a NS tertiary. The numbers in parentheses indicate the fractions of systems which are LK-possible in the sense that $\pi t_{\rm 1PN} > j_{\rm in} t_{\rm LK}$ at the end of the simulation.

Z [$Z_\odot$]	Model	Fraction of evolutionary outcomes $N/N_{\rm tot}$ [%]					
		$\Gamma_{\rm BBH+Star}$	$\Gamma_{\rm BBH+BH}$	$\Gamma_{\rm NSBH+Star}$	$\Gamma_{\rm NSBH+BH}$	$\Gamma_{\rm BNS+Star}$	$\Gamma_{\rm BNS+BH}$
0.01	Fallback kicks	0.72 (0.29)	2.84 (1.65)	0.03 (0.00)	0.02 (0.00)	0.00 (0.00)	0.00 (0.00)
	Proportional kicks	0.15 (0.01)	0.14 (0.03)	0.02 (0.00)	0.00 (0.00)	0.00 (0.00)	0.00 (0.00)
	No kicks	1.00 (0.45)	4.27 (2.57)	0.39 (0.27)	0.74 (0.59)	0.05 (0.00)	0.05 (0.02)
	Incl. dyn. tides	0.56 (0.27)	2.97 (1.74)	0.00 (0.00)	0.03 (0.01)	0.00 (0.00)	0.00 (0.00)
1.0	Fallback kicks	0.14 (0.13)	0.12 (0.10)	0.00 (0.00)	0.00 (0.00)	0.00 (0.00)	0.00 (0.00)
	Proportional kicks	0.00 (0.00)	0.00 (0.00)	0.00 (0.00)	0.00 (0.00)	0.00 (0.00)	0.00 (0.00)
	No kicks	0.34 (0.33)	1.40 (1.27)	0.72 (0.68)	0.66 (0.62)	0.08 (0.03)	0.06 (0.02)
	Incl. dyn. tides	0.13 (0.11)	0.16 (0.13)	0.00 (0.00)	0.00 (0.00)	0.01 (0.00)	0.00 (0.00)

2.3.3 Tertiary impact on inner binary interactions

We previously identified certain regions of parameter space where the tertiary companion induces dynamical instability, is ejected by a SN, or overflows its Roche-lobe. In this section, we investigate how the companion affects the evolution of the inner binary stars. It is well-known that massive stars in binaries are prone to closely interact and undergo one or more episodes of mass transfer (Paczyński, 1967b; Podsiadlowski et al., 1992; Sana et al., 2012; de Mink et al., 2013; Raucq et al., 2016; Stegmann & Antonini, 2021; Menon et al., 2021). Here, we determine whether the interaction with a tertiary companion changes the stellar evolution of the inner binary stars and the overall fraction of systems that experience a mass transfer phase.

In Fig. 2.8, we plot the initial distribution of the semi-major axis ratio $a_{\rm out}/a_{\rm in}$ and periapsis $a_{\rm in}(1-e_{\rm in})$ of triples in which the inner binaries undergo a phase of mass transfer (either stable or unstable). This is the case for $83\,\%$ ($87\,\%$) of all systems at $Z = 0.01\,{\rm Z}_\odot$ ($Z = 1.0\,{\rm Z}_\odot$). In the left panels, we highlight whether the initial relative inclination is in the Kozai angle regime ($\cos^2 i_{\rm tot} < 3/5$), where particularly strong LK oscillation are expected (see Chapter 1), and in the right panels, we show the differences between the initial eccentricity and its value at the onset of mass transfer.* We note that RLO outside the Kozai angle regime ($\cos^2 i_{\rm tot} \geq 3/5$) only occurs if the initial periapsis is below $a_{\rm in}(1-e_{\rm in}) \lesssim 10^3\,{\rm R}_\odot$ However, if the relative inclination is within the Kozai angles, RLO is possible in initially wider orbits and up to $\lesssim 10^5\,{\rm R}_\odot$. In these systems, the tertiary companion excites the inner eccentricity via LK oscillations and effectively reduces the periapsis so that the stars have to be less expanded in order to fill their Roche-lobe. RLO in those inner binaries is therefore induced by the perturbation from the tertiary companion.

In the right panels of Fig. 2.8 we show the change in eccentricity between the initial time and the onset of mass transfer. For $a_{\rm in}(1-e_{\rm in}) \gtrsim 10^3\,{\rm R}_\odot$ the binary eccentricity is higher than its initial value ($\Delta e_{\rm in} > 0$), demonstrating the impact of the LK mechanism. A considerable fraction of $16.4\,\%$ ($16.4\,\%$) of Roche-lobe overflowing systems at $a_{\rm in}(1-e_{\rm in}) < 10^3\,{\rm R}_\odot$, also have a higher eccentricity ($\Delta e_{\rm in} > 0.1$). Furthermore, these binaries are found to fill their Roche-lobe at an earlier evolutionary stage than in an equivalent run without tertiary companion. This shows that the impact of the LK mechanism extends to essentially all values of $a_{\rm in}$, but only for semi-major axis ratios below $a_{\rm out}/a_{\rm in} \lesssim 10^2$. Finally, if $a_{\rm in}(1-e_{\rm in}) \lesssim \mathcal{O}(10^1)\,{\rm R}_\odot$, the binary orbits can be significantly affected by tides. These binaries circularise due to tidal friction ($\Delta e_{\rm in} < 0$). Similar results are found by Toonen et al. (2020) who considered less massive triples with initial primary masses 1 – $7.5\,{\rm M}_\odot$.

Lastly, we investigate whether the tertiary companion changes the fraction of binaries that

*If an inner binary undergoes multiple mass transfer phases we are considering the first one.

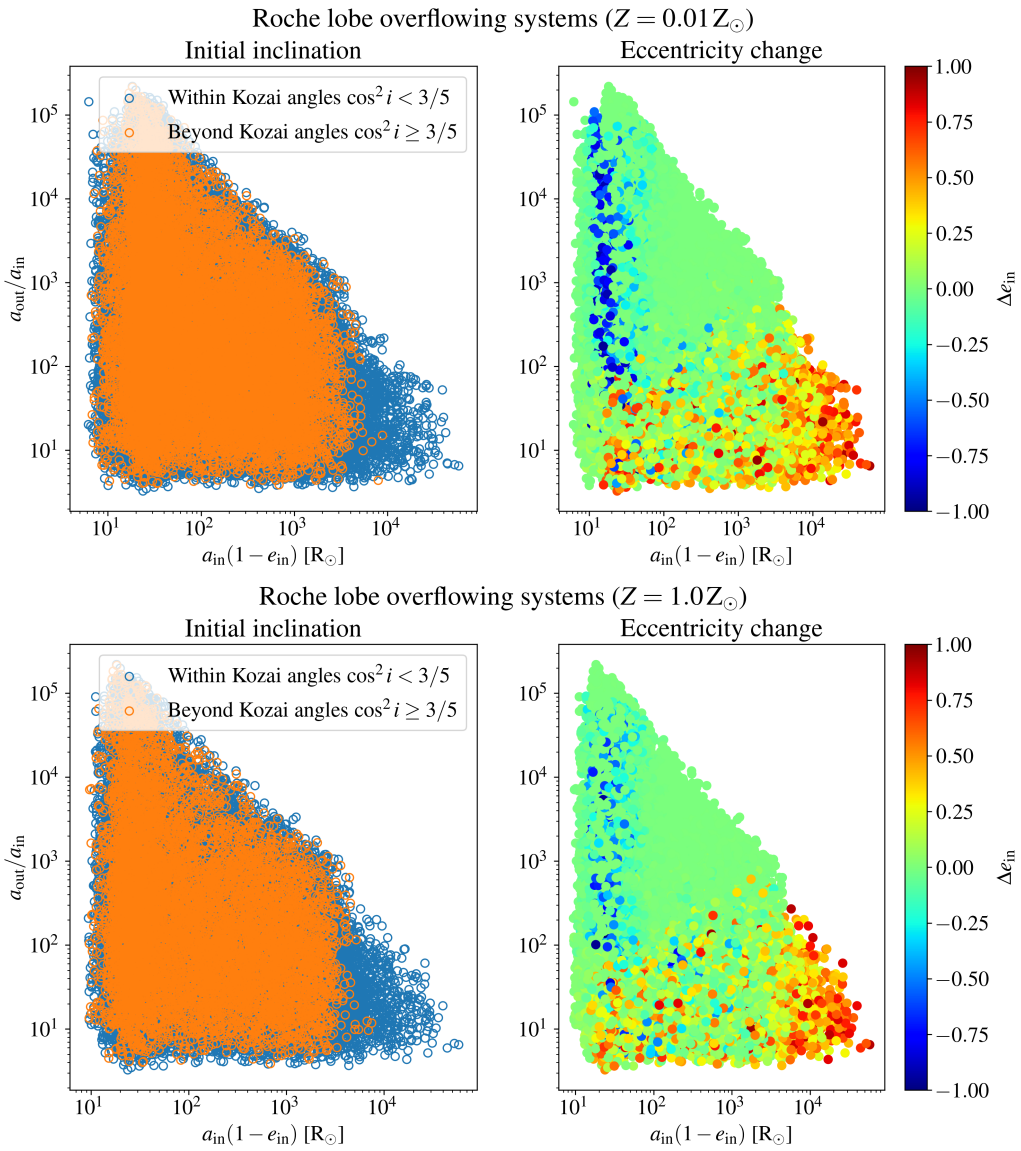

Figure 2.8. All triples whose inner binaries undergo a phase of mass transfer at $Z = 0.01\,Z_\odot$ (upper panels) and $Z = 1.0\,Z_\odot$ (lower panels). Plotted are the initial values for their semi-major axis ratio a_{out}/a_{in} and inner periapsis $a_{in}(1 - e_{in})$. The colour scheme on the left panels indicates the initial relative inclination between the inner and outer orbital plane. On the right panels, we indicate the eccentricity change Δe_{in} between the initial time and the onset of mass transfer.

experience a specific type of close interaction. More specifically, we distinguish between four types of stellar interactions:

(i) The inner binary stars merge;

(ii) The two stars do not merge, but undergo and survive at least one phase of CE;

(iii) The binary neither merges nor experiences a CE phase, but undergoes at least one phase of stable mass transfer;

(iv) If none of cases (i) – (iii) applies, the inner binary will evolve without undergoing any strong interaction and the stars will effectively behave as if they were single stars. Thus, we refer to this latter type of evolution as "effectively single".

As in Section 3.2, merger refers to any coalescence of the inner binary that involves at least one stellar component. In the left panels of Fig. 2.9, we show the fraction of binary interactions for $Z = 0.01$ (upper panel) and $1.0\ \mathrm{Z}_\odot$ (lower panel) as a function of their initial inner orbital period. Evidently, close stellar interactions between the massive inner binary members are prevalent at both metallicities since only 15% and 12% of them evolve as effectively single stars for $Z = 0.01$ and $1.0\ \mathrm{Z}_\odot$, respectively. The type of interaction depends on the binary orbital period. At $P_\mathrm{in} \lesssim 10\,\mathrm{days}$, the vast majority of inner binary stars merge. For those we highlight the binaries that merge in a CE which is initiated by a donor in the HG. Toward longer orbital periods the fraction of binary stars which undergo a stable mass transfer episode increases until the population becomes dominated by stars that do not interact at all (above $P_\mathrm{in} \gtrsim 10^4\,\mathrm{days}$). The major difference between the two metallicities lies in the fraction of systems that survive a CE phase (around $P_\mathrm{in} \approx 10^3\,\mathrm{days}$), which is 10% at $Z = 0.01\ \mathrm{Z}_\odot$ and only 2% at $Z = 1.0\ \mathrm{Z}_\odot$.

Systems whose evolution is terminated due to a tertiary RLO or due to dynamical instability are shown separately and found at short periods $P_\mathrm{in} \lesssim 10^2\,\mathrm{days}$ (cf., Section 2.3.1). Together these system contribute $12\,\%$ ($15\,\%$) at $Z = 0.01\,\mathrm{Z}_\odot$ ($Z = 0.01\,\mathrm{Z}_\odot$). Although their evolution is uncertain, we should expect that the triple interaction will leave a significant imprint on the evolution of the stars in these systems. In dynamical unstable systems, one member (typically the lightest star) is likely to be ejected from the triple leaving a bound pair of stars behind (Mardling & Aarseth, 2001). For tertiary RLO it can be expected that the inner binary will undergo some sort of interaction during the subsequent evolution, which is further perturbed by the mass accreted from the tertiary (Di Stefano, 2020a,b; Glanz & Perets, 2021; Hamers et al., 2022).

In the right panels of Fig. 2.9, we show the same analysis for the binary population model in which the initially identical inner binaries are evolved without tertiary companion (see Table 2.2). The phenomenon of tertiary-induced interactions as discussed in the previous section amounts to

a decrease by less than $3\,\%$ of effectively single inner binaries in the triple population. Hence, the presence of a tertiary companion only marginally changes the number of systems that evolve as effectively single binaries. On the other hand, as discussed above, the inner binary evolution is more significantly affected at short orbital periods, where we see systems that undergo a tertiary RLO or become dynamical unstable.

In Figures 2.10 and 2.11, we show the same comparison in the `proportional kicks` and `no kicks` model, respectively. While the former is nearly identical to the `fallback kicks` model, the latter shows a much higher fraction of systems which merge or undergo a CE evolution with a donor in the HG. This happens when the binary companion is already a compact object. In the non-zero kick models, these systems tend to be disrupted already at the formation of the compact object due to a natal kick.

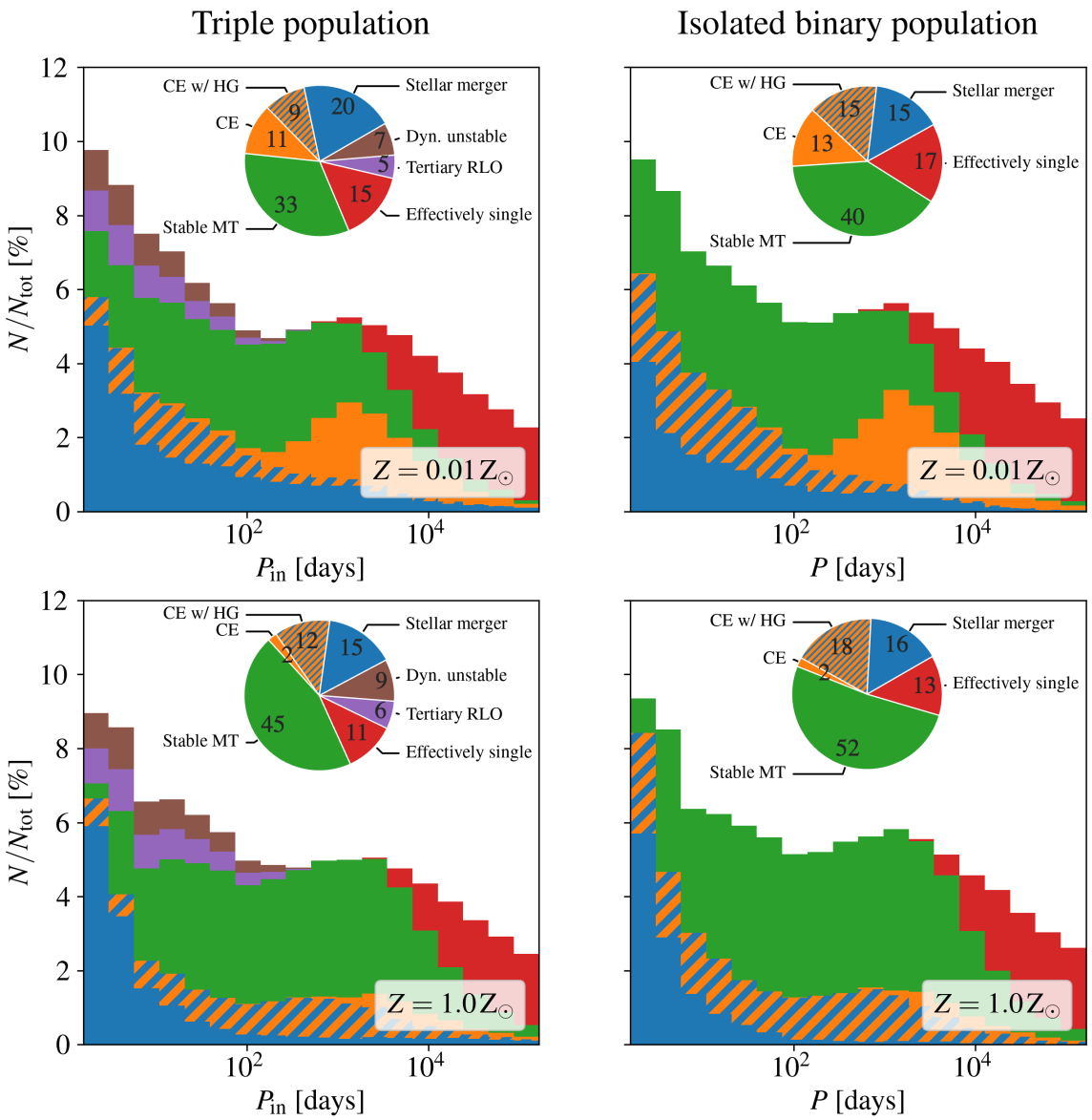

Figure 2.9. Fractions of systems in a triple population (left panels) and isolated binary population (right panels) that undergo a certain kind of close stellar interaction as a function of their initial (inner) orbital period in the `fallback kicks` model.

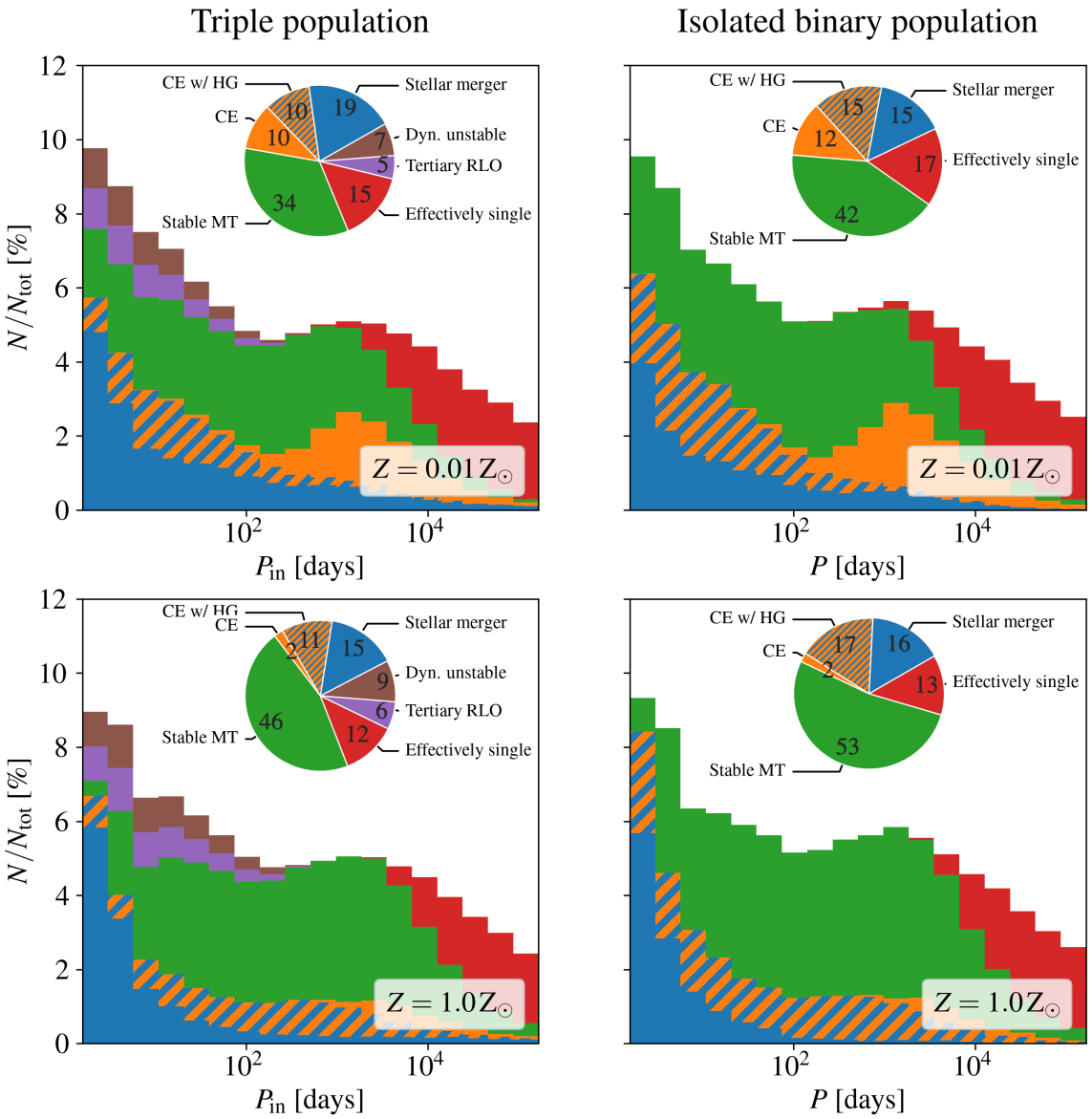

Figure 2.10. Same as Fig. 2.9 in the `proportional kicks` model.

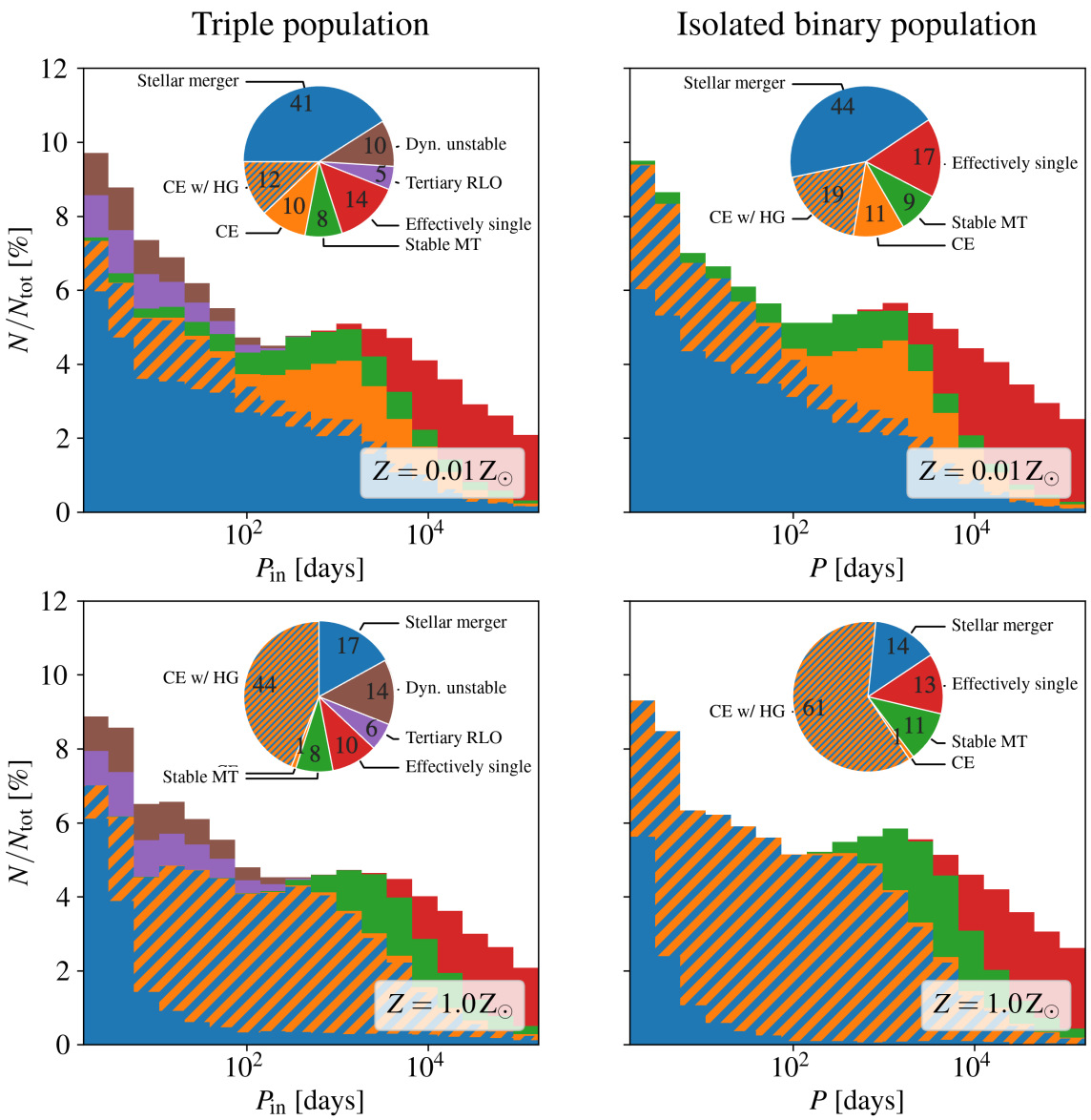

Figure 2.11. Same as Fig. 2.9 in the `no kicks` model.

Chapter 3

Black hole mergers from stellar mergers in triples

Massive binary stars are prone to merge before they could form any compact object (Sana et al., 2012; Menon et al., 2021). In Chapter 2, we have seen that this is also true for interacting massive stars in the inner binary of triples. In that case, additional stellar mergers could be dynamically driven by the gravitational perturbation from the tertiary companion. Regardless of whether the stellar merger is driven by the tertiary or if it would also take place if the inner binary was placed in isolation, a stellar merger in a triple opens up the interesting possibility of a post-merger binary evolution between the merger product star and the tertiary companion. Evidently, this possibility does not exist if the stellar merger took place in an isolated binary.

In this chapter, we investigate how the subsequent post-merger evolution of the merger product star and the tertiary companion could lead to the formation of a BBH which merges due to the emission of GWs. Moreover, we compare them with the BBH mergers formed via alternative formation channels. For this purpose, we distinguish between the following populations.

- Triple population: Starting from a hierarchical triple population, stable BBHs are formed which subsequently merge within a Hubble time due to the emission of GWs. These BBHs might form in two different ways as following.
  - Inner binary channel: The two stars in the inner binary form a stable BBH.
  - Outer binary channel: The two stars in the inner binary merge and the post-merger star and tertiary companion subsequently form a stable BBH.
- Isolated binary population: Starting from an isolated binary population the binary stars form stable BBHs which subsequently merge within a Hubble time due to the emission of GWs. This is a standard population model used in the literature for which the effect of a tertiary companion is not considered (Paczyński, 1967b; Podsiadlowski et al., 1992; Dominik et al.,

2012; Belczynski et al., 2016a; Giacobbo & Mapelli, 2018; Olejak et al., 2021; de Mink et al., 2013; Raucq et al., 2016; Stegmann & Antonini, 2021; Menon et al., 2021; Olejak et al., 2021).

Hereafter, *stellar merger* refers to the merger of two stars (or one star and a compact object), whereas *BBH merger* to the merger of a BBH promoted by GW radiation. The formation of BBH mergers via the outer binary channel is the novel mechanism investigated here.

3.1 Methods

3.1.1 Stellar evolution

To follow the stellar evolution in time, we use a simplified version of `TSE` in the majority of our models (see below) where we ignore the dynamical effect of the tertiary. Instead, we use the code `MOBSE` (Giacobbo et al., 2018; Giacobbo & Mapelli, 2018, 2019, 2020) which is an update of the widely-adopted binary stellar evolution code `BSE` (Hurley et al., 2002). `BSE/MOBSE` models all relevant evolutionary steps of stellar binaries including mass transfer episodes, CE evolution, and tidal interaction. `MOBSE` improves `BSE` by including up-to-date metal-dependent stellar wind prescriptions, fallback kicks imparted to the remnants of SN explosions, and (pulsational) pair instability SNe (Giacobbo et al., 2018; Giacobbo & Mapelli, 2018, 2019, 2020). For our purpose, `MOBSE` provides an adequate tool to simulate isolated binaries, starting on the ZAMS.

Applied to triples, we use `MOBSE` to evolve the inner binary and tertiary companion as two dynamically independent entities as done in previous triple studies (Antonini et al., 2017, 2018; Rodriguez & Antonini, 2018; Martinez et al., 2022). As in previous chapters, we consider hierarchical stellar triples in which a close inner binary with semi-major axis $a_{\rm in}$ and eccentricity $e_{\rm in}$ is orbited by a distant tertiary star with semi-major axis $a_{\rm out} \gg a_{\rm in}$ and eccentricity $e_{\rm out}$ (see Fig. 3.1).

In reality, the distant tertiary companion could perturb the dynamics of the inner binary through the LK mechanism, leading to large amplitude oscillations of $e_{\rm in}(t)$ (Lidov, 1962; Kozai, 1962). In Chapter 2, we have seen that this could alter the evolution of the inner binary stars by inducing eccentric mass transfer (see also Toonen et al., 2020; Hamers & Dosopoulou, 2019). Moreover, the long-term interaction with the companion could drive the inner binary to a merger after a BBH is formed (Silsbee & Tremaine, 2017; Antonini et al., 2017, 2018; Liu & Lai, 2018; Rodriguez & Antonini, 2018; Liu et al., 2019; Fragione & Kocsis, 2020; Martinez et al., 2022). In order to investigate the effect of dynamics on the outer binary channel, we do include one computationally expensive model (`3BodyDynamics`) in which we reevolve all systems which above lead to a BBH

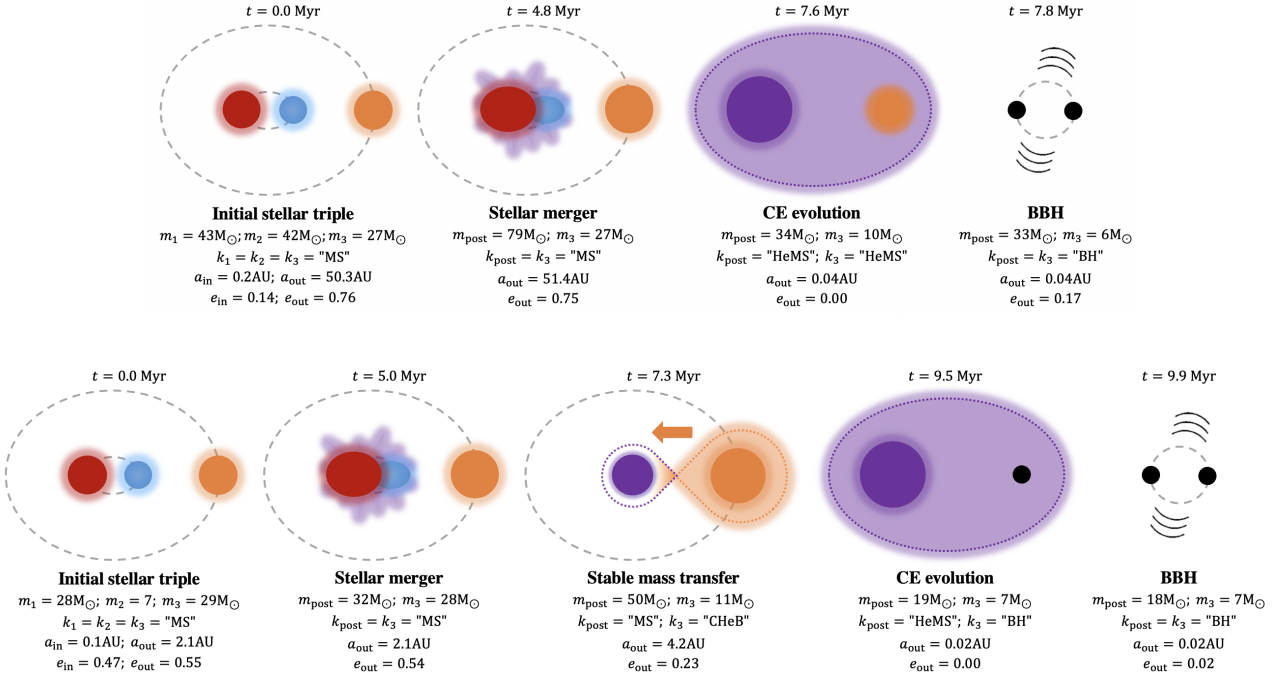

Figure 3.1. Two examples of low mass ratio BBH mergers due to the outer binary channel in the `Rapid1` model at metallicity $Z \simeq 1 \times 10^{-4}$ (upper panel) and 5×10^{-4} (lower panel). The final BBHs merge after $t_{\rm GW} \simeq 172\,{\rm Myr}$ and $29\,{\rm Myr}$, respectively. The type of the stars is described by $k_{1,2,3,{\rm post}}$, where CHeB and HeMS refers to a Core Helium Burning and Naked Helium MS star, respectively. The provided parameter values refer to the end of each event, e.g., to the time at which the two stars fully merge, the stable mass transfer peters out, or the CE is successfully ejected leaving behind a close binary. Distances and eccentricities are not drawn to scale.

merger using the secular three-body integrator, TSE, presented in Chapter 2. Only reevolving the systems which above lead to a BBH merger potentially ignores systems in which a stellar merger is solely driven by the dynamical effect of tertiary (Toonen et al., 2022), i.e., it would not occur if the inner binary was in isolation. Hence, the resulting rates of BBH mergers in the 3BodyDynamics must be treated as lower limits. As a result, we will show below that the tertiary effect on the distribution of these BBH mergers is small. Thus, in all the other models we neglect dynamics, which allows us to efficiently explore the relevant parameter space.

During the inner binary evolution $a_{\rm in}$ changes due to tides, SN kicks, GW emission, stellar winds or during an episode of mass transfer. These processes are self-consistently treated by MOBSE (and likewise for the isolated binary population). For the outer binary evolution we proceed as in Section 2.1.1 and expand $a_{\rm out}(t)$ according to the fractional mass loss from the system, e.g., due to winds and during a mass transfer episode in the inner binary.

At any point in time we check whether the triples become dynamically unstable (see Section 2.2.6), or if the tertiary companions fills their Roche-lobe (see Section 2.1.3). In either events we stop the evolution of the systems because their subsequent evolution is uncertain. Recent studies propose that additional stellar mergers could be triggered by a mass transfer phase initiated by Roche-lobe filling tertiary companions (Glanz & Perets, 2021; Gao et al., 2023).

During the stellar evolution the inner binary stars might merge. This happens when the two stars undergo a CE in which their inspiralling cores coalesce before the envelope could be ejected (see below), or when two stars of similar compactness, e.g., two MS stars, collide. Our description of stellar mergers follows closely that of Glebbeek & Pols (2008) and Hurley et al. (2002). Most relevant to our work are MS-MS stellar mergers (see Section 3.2). This kind of merger yields another MS star which is rejuvenated. That is, the additional hydrogen fuel delays the time at which the post-merger star leaves its MS. In general, the rejuvenation process can be described as

$$\tau_{\rm post} = \frac{1}{\alpha q_{c,\rm post}} \frac{1}{1-\phi} \frac{q_{c,1} m_1 \tau_1 + q_{c,2} m_2 \tau_2}{m_{\rm post}}, \tag{3.1}$$

where α parameterizes the amount of mixing and $\tau_{1,2,\rm post} \in [0,1]$ is the fractional timescale of the primary, secondary, and post-merger star on the MS, respectively (Glebbeek & Pols, 2008). ϕ is the fractional mass loss during the merger (see below) and $q_{c,1,2,\rm post}$ the effective core mass fraction defined as the fraction of hydrogen that is burned during the MS of the primary, secondary, and post-merger star, respectively. Stellar observables like the radius and luminosity substantially increase only toward the end of the MS evolution, $\tau_{\rm post} \to 1.0$ (Hurley et al., 2000). Rejuvenation is equivalent to $\tau_{\rm post} < \max(\tau_1, \tau_2)$, i.e., the post-merger star appears younger than the most evolved inner binary star did (or both).

Here, we adopt the mass-dependent approximation for the effective core mass fractions of Glebbeek & Pols (2008) and a mixing parameter of $\alpha = 1.14$ (Schneider et al., 2016). By default, `BSE/MOBSE` follows Tout et al. (1997) using $\phi = 0$, $q_{c,1} = q_{c,2} = q_{c,\mathrm{post}} = 0.1$, and $\alpha = 10$ (Glebbeek & Pols, 2008). This is based on the supposition that the merging stars fully mix and that the end of the MS is reached when 10 per cent of the total hydrogen fuel has been burnt (Tout et al., 1997). Thus, this prescription likely overestimates rejuvenation since it is expected that the MS stars do not fully mix and that less core hydrogen is replenished (Glebbeek & Pols, 2008; de Mink et al., 2013). We explore the original prescription in one additional model (`Tout97`).

The mass m_{post} of the post-merger star is uncertain. Here, we follow Glebbeek et al. (2013) and assume that during a MS-MS merger the system suffers a fractional mass loss

$$\phi = \frac{m_{\mathrm{in}} - m_{\mathrm{post}}}{m_{\mathrm{in}}} = 0.3 \frac{q_{\mathrm{in}}}{(1+q_{\mathrm{in}})^2}, \tag{3.2}$$

where $q_{\mathrm{in}} = \min(m_1, m_2)/\max(m_1, m_2)$.

Immediately after the merger, it is expected that the resulting star undergoes a bloated phase where its radius expands before it contracts to its equilibrium state on the (thermal) Kelvin-Helmholtz timescale (Suzuki et al., 2007; Hirai et al., 2021). If it is sufficiently close, the post-merger orbit may be partially or entirely enclosed by the outermost parts of the bloated post-merger star. This situation may give rise to interesting transient phenomena as the tertiary companion plunges into the bloated envelope (Portegies Zwart & van den Heuvel, 2016; Hirai et al., 2021). In general, it is not expected that the post-merger orbit gets significantly perturbed by the interaction between companion and envelope since the bloated phase is brief and only a small fraction of the stellar mass undergoes a large expansion (Schneider et al., 2020). Nevertheless, we also include a conservative model (`DiscardBloated`) in which we discard any system whose outer periapsis $a_{\mathrm{out}}(1-e_{\mathrm{out}})$ at the time of the merger is smaller than the radius of the bloated star. Unfortunately, it is not well understood by how much the radius of the bloated post-merger star expands. Here, we use the Hayashi limit as a theoretical upper bound to the radius, $R_{\mathrm{post}} = \sqrt{L_{\mathrm{post}}/4\pi\sigma T_{\mathrm{post}}^4}$, where σ is the Stefan-Boltzmann constant and we assume a surface temperature limit of $T_{\mathrm{post}} = 10^{3.7}\,\mathrm{K}$. For the luminosity L we use the Eddington limit $L_{\mathrm{Edd}}/L_\odot \simeq 3.2 \times 10^4 m_{\mathrm{post}}/M_\odot$ beyond which the star would leave hydrostatic equilibrium and its hydrogen envelope would suffer intense radiation-driven winds. Computed in this way the radius serves as strict upper limit to that of the bloated star.

After a stellar merger we use `MOBSE` to continue the integration of the outer orbit composed of the post-merger star and the tertiary companion. If the system survives the subsequent stellar evolution to form a stable BBH, we then calculate the merger timescale induced by GW emission

(Eq. (1.66), Peters, 1964). We add this timescale to the time elapsed until BBH formation to obtain the delay time between star formation and BBH merger, which is used to calculate the BBH merger rate (see below). An analogue expression holds for BBHs formed in inner and isolated binaries, respectively. An example evolution of two BBHs formed via the outer binary channel is sketched in Fig. 3.1.

In our models, most BBHs merge only if the orbits of the isolated, inner, or post-merger binaries, respectively, significantly inspiraled during a CE evolution. Otherwise, the progenitor stars are too far apart for the resulting BBH to merge within a Hubble time.

A CE evolution occurs when there is a collision involving a giant star with a dense core or if there is a mass transfer phase from a giant on a dynamical timescale. In either cases the giant's envelope engulfs the orbit of the binary companion and the giant's core. The orbit suffers a friction-driven decay within the envelope which heats up the latter. As a result, the companion and core either coalesce within the envelope or the latter is ejected leaving behind a tight binary which could subsequently form a (merging) BBH. Thus, the efficiency at which orbital energy of the inspiralling cores is transferred to the envelope significantly affects the number of surviving binaries but is very uncertain (Ivanova et al., 2013). Here, we adopt the standard $\alpha_{\rm CE}$-formalism (Hurley et al., 2002) where the efficiency is described by the free parameter $\alpha_{\rm CE}$.

In this chapter, we study a set of plausible values for $\alpha_{\rm CE}$ which are summarised in Table 2.1. Additionally, we explore different BH formation mechanisms following the “rapid" and “delayed" SN model from Spera et al. (2015) and assume different treatments of rejuvenation and the bloated stars. We also include three-body dynamics in one of our models as described above.

3.1.2 Initial conditions

In order to set up the initial conditions of the triple parameters on the ZAMS, we adopt simple probability density functions motivated by observations. We sample the primary mass m_1 from a standard Kroupa (2001) mass function $N(m_1) \propto m_1^{-2.3}$, between 5 and $150\,\mathrm{M}_\odot$. For the mass ratio $q_\mathrm{in} = m_2/m_1$, eccentricity e_in, and orbital period $P_\mathrm{in} = 2\pi a_\mathrm{in}^{3/2}/(Gm_\mathrm{in})^{1/2}$ we adopt simple power-law fits to the observational data of Galactic binaries with O-type primaries (Sana et al., 2012): $N(q_\mathrm{in}) \propto q_\mathrm{in}^{-0.1}$ between 0.1 and 1.0, $N(e_\mathrm{in}) \propto e_\mathrm{in}^{-0.45}$ between 0.0 and 0.9, and $N\left(\log(P_\mathrm{in}/\mathrm{days})\right) \propto \left(\log(P_\mathrm{in}/\mathrm{days})\right)^{-0.55}$ between 0.15 and 5.5. We only keep systems in which also $m_2 \geq 5\,\mathrm{M}_\odot$ since otherwise in neither of the investigated populations BBHs could be formed.

To any inner binary we repetitively propose tertiary companions until they meet the stability criterion (Mardling & Aarseth, 2001) (see Section 2.2.6, beyond which the triple would become chaotic and our adopted method breaks down. To this end, we sample the tertiary mass m_3 from a uniform distribution between $8\,\mathrm{M}_\odot$ and $m_1{+}m_2$, the outer eccentricity from a thermal distribution $N(e_\mathrm{out}) \propto e_\mathrm{out}$ between 0.0 and 0.9, and the outer semi-major axis from a log-uniform distribution between a_in and $10^4\,\mathrm{AU}$.

For our model with three-body dynamics included, we assume random orientations of the inner and outer orbit.

The massive stellar progenitors of BHs are consistent with a near hundred percent fraction of triples and higher order systems (Moe & Di Stefano, 2017). Nevertheless, most previous work focused on the evolution of isolated binaries (e.g., Paczyński, 1967b; Podsiadlowski et al., 1992; Dominik et al., 2012; Belczynski et al., 2016a; Giacobbo & Mapelli, 2018; Olejak et al., 2021; de Mink et al., 2013; Raucq et al., 2016; Stegmann & Antonini, 2021; Menon et al., 2021; Olejak et al., 2021). Thus, as a reference, we also study the evolution of an isolated binary population without tertiary companions. Comparing it to the triple population allows us to discern the impact of the simplified assumption made in the literature. For our isolated binary population we simply use the same distributions of masses and orbital parameters as for the inner binaries of the triple population. Since the orbital distributions of the latter were taken from observational surveys of binaries, their initial conditions are consistent with observations.

3.2 Results

A key parameter that determines the relative efficiency of both triple channels is their initial outer semi-major axis $a_\mathrm{out,0}$. In Fig. 3.2, we show the cumulative fraction of BBH mergers formed in either channel as a function of $a_\mathrm{out,0}$. In any of our models, we find the outer binary channel

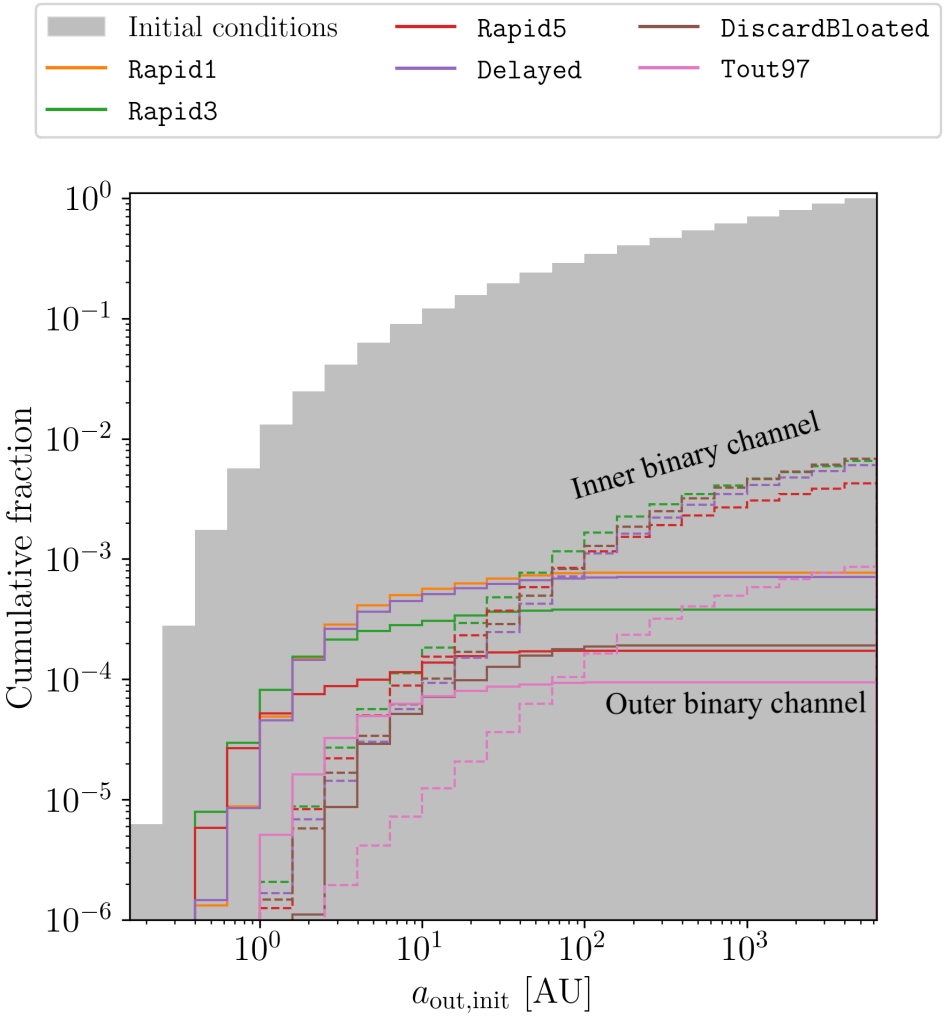

Figure 3.2. Cumulative distribution of BBH mergers from triple population as a function of the initial outer semi-major axis (denoted as $a_{\rm out,init} = a_{\rm out,0}$). Solid lines correspond to mergers via the outer binary channel and dashed lines to the inner binary channel. The outer binary channel dominates the formation of BBH mergers from compact triples with $a_{\rm out,0} \lesssim 10^1 - 10^2\,{\rm AU}$, where the precise value depends on the assumed model. The metallicity is sampled log-uniformly.

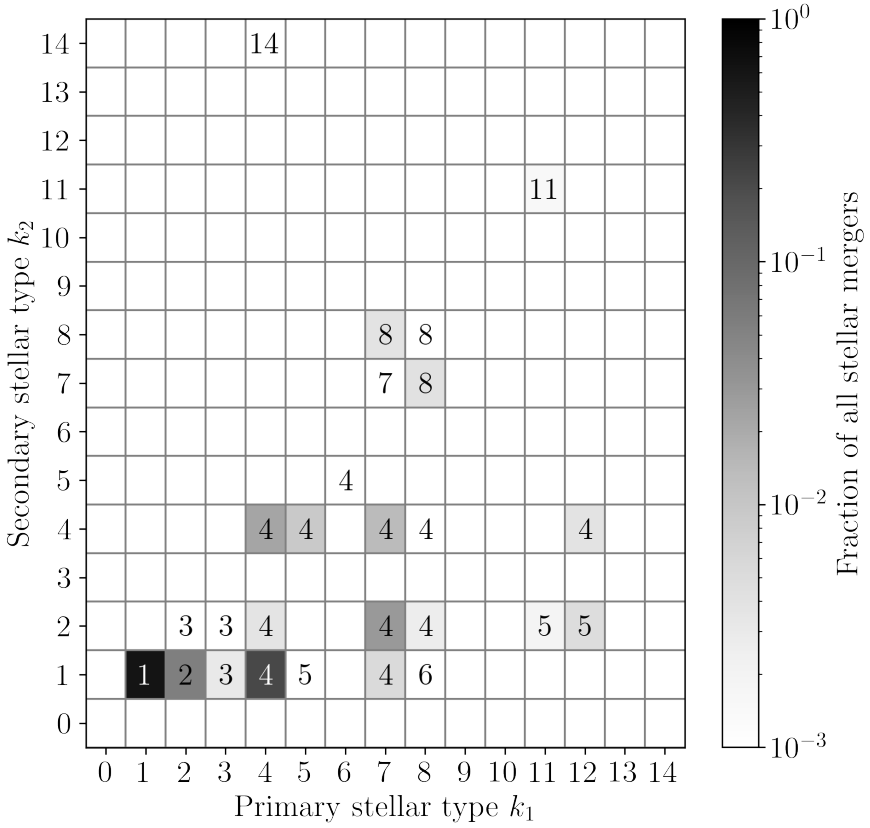

Figure 3.3. Collision matrix of stellar mergers in the `Rapid1` model. The grayscale correspond to the fraction of each merger type normalised to one. The axes and integers in each cell indicate the stellar type of the merging stars and the post-merger star, respectively (only cells with nonzero fractions are described). The integers are defined as in Hurley et al. (2002, Section 1), e.g., $k_{1,2} = 1$ for MS stars.

to be the dominant way of forming BBH mergers from triples with $a_{\rm out,0} \lesssim 10^1 - 10^2\,{\rm AU}$. This is simply because the inner orbits of these compact triples must be even closer in order to ensure dynamical stability and hierarchy. This makes the inner binary stars prone to undergo a stellar merger. Above $a_{\rm out,0} \gtrsim 10^1 - 10^2\,{\rm AU}$, the inner binary channel dominates. In these systems, any post-merger star and tertiary companion are too far apart from each other to undergo a mass transfer episode which is necessary to shrink their orbit. Hence, these systems are unable to form BBHs that end up close enough to merge within a Hubble time. Thus, in the entire triple population the inner BBH mergers outweigh those formed via the outer binary channel by a factor of $\sim \mathcal{O}(10)$.

As a typical example we show in Fig. 3.3 the distribution of stellar types which merge in the `Rapid1` model. In any model, the majority (ranging from $\simeq 60\,\%$ to $80\,\%$ in the `Rapid1` and

`Rapid5` model, respectively) of stars already merge on their MS yielding another star on the MS. By the time of the stellar merger, most ($\simeq$ 80 to 90 %) of the tertiary stars are still on their MS as well. Hence, these merger occur at a relatively early evolutionary stage of all three stars, typically after a few Myr.

Previously it has been suggested that stellar mergers of an evolved star with a carbon-oxygen core and a MS star could produce a post-merger star that circumvents a pair-instability SN (Di Carlo et al., 2019; Ballone et al., 2023). Thus, it has been suggested that GW190521-like events (Abbott et al., 2020b) with the primary BH mass being in the upper mass gap are possibly formed in young stellar clusters (Di Carlo et al., 2019, 2020a,b; Kremer et al., 2020). We note that our MS-MS mergers are not expected to produce a star which could populate the upper mass gap.

In both populations and channels, the fraction of systems which lead to BBH mergers is higher at low metallicity. We find that a fraction $\sim \mathcal{O}(10^{-2})$ of the isolated binaries and inner binaries, respectively, evolve to merging BBHs if $Z \lesssim \mathcal{O}(10^{-3})$. Above $Z \gtrsim \mathcal{O}(10^{-3})$ the fraction sharply drops to fractions $\sim \mathcal{O}(10^{-5})$ at solar metallicity. Similarly, the number of BBH mergers via the outer binary channel falls from $\sim \mathcal{O}(10^{-3})$ at low metallicities to $\sim \mathcal{O}(10^{-5})$ at solar metallicity.

As shown in Fig. 3.4, BBH mergers from the triple and isolated binary population are predominantly formed with equal masses ($q \simeq 1$). This results from the CE evolution of the progenitor stars which precedes most of our BBH mergers. In the α_{CE}-formalism, low mass ratio stellar binaries are more susceptible to merge within a CE rather than forming a close binary which could eventually lead to a BBH merger.

Yet, the BBH mergers formed from the triple population tend to have lower mass ratios than those from the isolated binary population. Although in both populations, we find BBH mergers with mass ratios as low as $q \simeq 0.1$, BBH mergers with $q \lesssim 0.4 - 0.6$ are much more frequently formed from triples because of the outer binary channel. In this channel, we identify two ways that facilitate the formation of low mass ratio BBH mergers which are shown in Fig. 3.1.

First, a stellar merger simply produces a more massive star. Thus, there are systems in which the post-merger star is much more massive than the tertiary companion. Typically, in these systems the mass of the post-merger star is larger than $m_{\mathrm{post}} \gtrsim 60\,\mathrm{M}_{\odot}$ whereas that of the tertiary companion is $m_3 \simeq 20 - 30\,\mathrm{M}_{\odot}$. While details depend on metallicity and the SN prescription (Spera et al., 2015; Fryer et al., 2012), there is the general tendency that more massive stars also form more massive BHs. As exemplified in the upper panel of Fig. 3.1, a low mass ratio BBH merger is formed after the massive post-merger star initiated a CE evolution during which the orbit of both stellar cores efficiently decays. This evolutionary pathway is responsible for the formation of the lowest BBH mass ratios down to $q \simeq 0.1$.

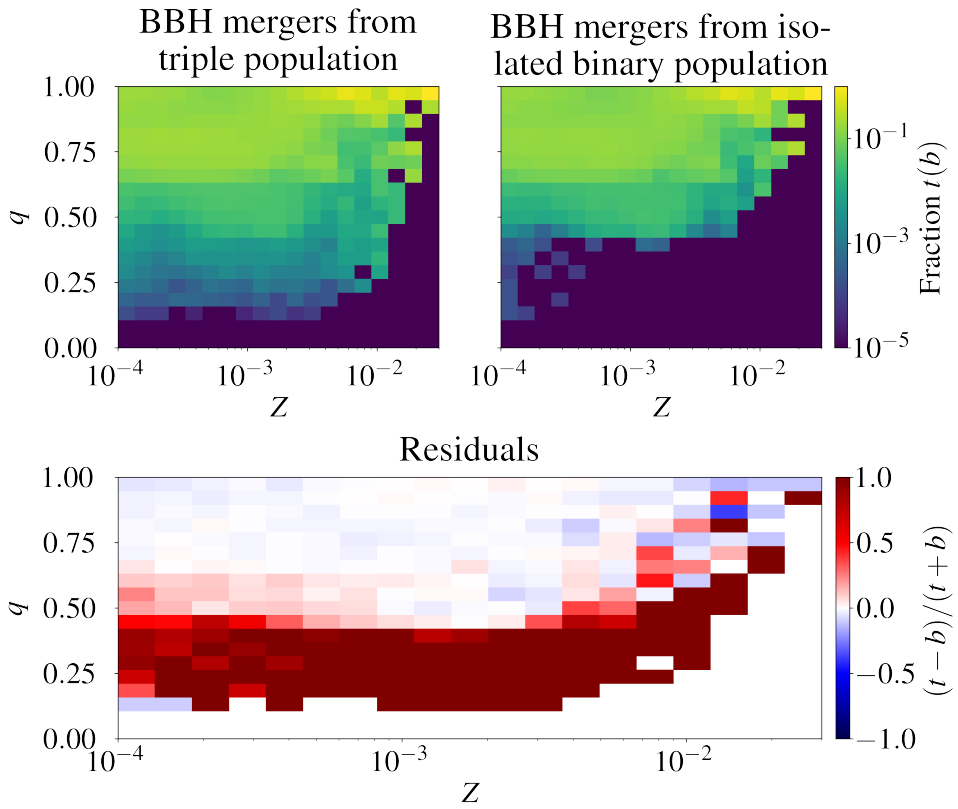

Figure 3.4. BBH merger distribution as a function of metallicity in the `Rapid1` model. The upper panels show for each metallicity the mass ratio distribution from triples and binaries, respectively. The lower panel shows the relative residuals between both populations. For any bin, they are defined as $(t-b)/(t+b)$ where t corresponds to the bin value in the triple population and b to that of the binary population. Thus, colored areas indicate a large difference between the two populations.

Second, as shown above, the very large majority of BBH mergers in the outer binary channel are preceded by a MS-MS stellar merger. The resulting MS star is rejuvenated. Thus, there are systems in which the post-merger star is more massive but less evolved than the tertiary companion star. Consequently, the latter fills its Roche-lobe first and initiates a stable mass transfer phase onto the post-merger star as exemplified in the lower panel of Fig. 3.1. This further increases the imbalance of the stellar progenitor masses and the resulting BH masses. In this way, low mass ratio BBH mergers with $q \gtrsim 0.3$ can be formed. It requires the mass of the post-merger star to be only a few solar masses $\lesssim 10\,\mathrm{M}_\odot$ larger than that of the tertiary progenitor star.

BBH mergers from an isolated binary population evolve differently. Typically, the progenitor of the primary BH was the donor star of the first stable mass transfer (e.g., Belczynski et al., 2016a, Figure 1) which reduces the imbalance of the resulting BH masses. We note that previous models of isolated binary populations can produce a larger number of low mass ratio BBH mergers only under certain assumptions (Stevenson et al., 2017; Olejak et al., 2020; Belczynski et al., 2020). As discussed by Belczynski et al. (2020), the resulting mass ratios of BBH mergers crucially depend on the fraction $f_a \in [0, 1]$ of transferred mass that is accreted by the progenitor of the secondary BH. Lower values of f_a tend to produce lower mass secondary stars/BHs and therefore lead to smaller mass ratios of BBH mergers. For example, Zevin & Bavera (2022) explore different values of f_a and find that the bulk of their BBH population has $q \gtrsim 0.2$ for $f_a = 0$ (fully nonconservative) whereas $q \gtrsim 0.4$ for $f_a = 1$ (fully conservative). Unfortunately, f_a is poorly constrained and any value between zero and one seems possible (Wellstein et al., 2001; de Mink et al., 2007; Erdem & Öztürk, 2014; Schneider et al., 2015; Shao & Li, 2016; Mennekens & Vanbeveren, 2017; Dervişoğlu et al., 2018; Belczynski et al., 2020).

In the remainder of this work, we investigate the BBH merger rates from both populations and compare them to the one inferred from GW detections.

In the local Universe the total BBH merger rate inferred from the third Gravitational-wave Transient Catalog (GWTC-3) is $\mathcal{R}(z = 0) = 16.7^{+16.5}_{-8.7}\,\mathrm{Gpc}^{-3}\,\mathrm{yr}^{-1}$ ($90\,\%$ C.L.) by using the "flexible mixture model" (Tiwari, 2021; Tiwari & Fairhurst, 2021; Tiwari, 2022). To calculate the BBH merger rate from our models, we consider the rate and metallicity at which the stellar progenitor systems are formed throughout cosmic history and convolve it with the delay time distribution. Thus, the rate at a given redshift z takes into account all systems that were formed at some earlier redshift $z_b > z$ and whose delay time matches the cosmic time elapsed between z_b and z. We use the metallicity-dependent cosmic star formation rate of Madau & Fragos (2017) and adopt concordant ΛCDM cosmology. Details of our calculations are provided in the Appendix A.3.

In Table 3.2, we report the resulting total rates for in our models at $z = 0$. Across all models, we find the median contribution of the outer binary channel to the total BBH merger rate to be

in the range $\mathcal{R}(z=0) = 0.3 - 25.2\,\mathrm{Gpc^{-3}\,yr^{-1}}$ which amounts to a typical fraction $\sim \mathcal{O}(0.01 - 0.1)$ of the BBH merger rate from the triple population. In any model, the total rates from the triple and isolated binary population are in the same order of magnitude as the observationally inferred one. Thus, although our medians tend to overpredict the inferred local BBH merger rate by a factor of two to three they are in good agreement compared to formation channels that were previously proposed (Mandel & Broekgaarden, 2022).

Table 3.2. BBH merger rates $\mathcal{R}(z = 0)$ in $\mathrm{Gpc}^{-3}\,\mathrm{yr}^{-1}$. For the total rate of the triple population, the contributions from both channels have to be added. The numbers in the table indicate the median rates and $5 - 95\,\%$ credible intervals, respectively.

Model name	Triple population		Isolated binary population	GWTC-3
	Inner binary channel	Outer binary channel		
`Rapid1`	$42.6^{+27.4}_{-18.4}$	$12.5^{+12.7}_{-6.1}$	$46.1^{+32.1}_{-17.6}$	$16.7^{+16.5}_{-8.7}$
`Rapid3`	$48.3^{+33.0}_{-17.8}$	$1.6^{+2.4}_{-0.8}$	$37.2^{+31.9}_{-13.4}$	
`Rapid5`	$16.5^{+13.9}_{-4.3}$	$0.7^{+1.8}_{-0.4}$	$16.9^{+14.8}_{-7.5}$	
`Delayed`	$21.7^{+15.2}_{-8.0}$	$5.3^{+14.6}_{-3.2}$	$22.1^{+26.7}_{-9.2}$	
`DiscardBloated`	$42.6^{+31.7}_{-14.6}$	$5.7^{+9.5}_{-2.8}$	$46.1^{+32.1}_{-17.6}$	
`Tout97`	$44.5^{+19.1}_{-12.8}$	$2.8^{+5.6}_{-1.5}$	$46.1^{+32.1}_{-17.6}$	

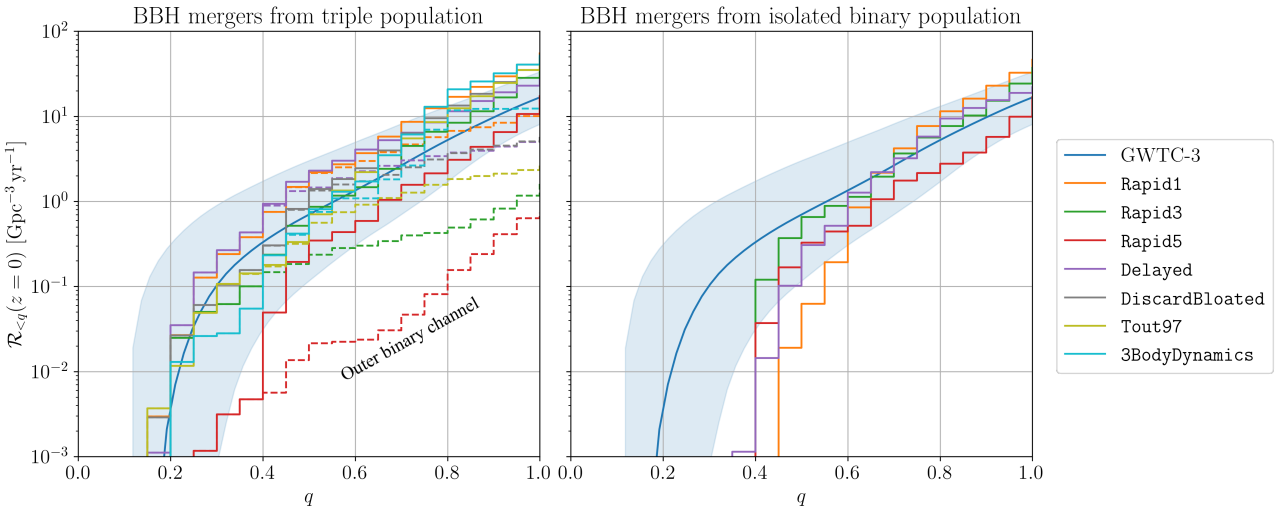

Figure 3.5. Cumulative mass ratio distribution of BBH mergers in the local Universe ($z = 0$). In the left panel, we show the BBH mergers from the triple population and in the right panel from the isolated binary population (solid lines). In the former, we highlight the contribution of BBH mergers via the outer binary channel (dashed lines) which start to dominate below $q \lesssim 0.4 - 0.6$. All lines indicate median values. The blue envelope shows the $5 - 95\,\%$ credible interval of GWTC-3.

Despite only adding a subdominant fraction to the total merger rate, the BBH mergers formed via the outer binary channel significantly affect the mass ratio distribution of the entire population. In Fig. 3.5, we plot the cumulative rate

$$\mathcal{R}_{<q}(z=0) = \int_0^q \frac{\mathrm{d}\mathcal{R}(z=0)}{\mathrm{d}q'}\,\mathrm{d}q' \tag{3.3}$$

of BBH mergers as a function of their mass ratio q. Neither the inner binary channel in triples nor isolated binaries are found to reproduce well the mass ratio distribution inferred by the GW detections. While they agree well with the cumulative rate above $q \simeq 0.4 - 0.6$ they fail at lower mass ratios. The inferred mass ratio distribution can be better recovered after including the contribution from the outer binary channel (dashed lines). For the aforementioned reasons, it is found to be more efficient in producing low mass ratio BBH mergers leading to a less steeply decreasing distribution toward low values of q. Below the threshold mass ratio $q \simeq 0.4 - 0.6$, BBH mergers from the outer binary channel dominate the inner binary channel.

Chapter 4

Flipping spins in mass transferring binaries

4.1 Introduction

A large number of stars are found to be in close binary systems. The fraction of MS stars which are bound to one or more companions ranges from ~ 40 per cent in the case of solar-type stars up to ~ 90 per cent for massive O-type stars (Duquennoy & Mayor, 1991; Sana et al., 2012; Moe & Di Stefano, 2017). A substantial fraction of binaries move on close orbits with orbital periods less than $\sim 10^3$ to 10^4 days. Compared to a life in isolation, their evolutionary pathways are significantly altered as they can undergo a phase of mass transfer in which they exchange a large amount of mass and rotational angular momentum with their close companions (Paczyński, 1971). Mass transfer between binary members is responsible for a set of astrophysical phenomena such as X-ray binaries (Shakura & Sunyaev, 1973) and millisecond pulsars (Bhattacharya & van den Heuvel, 1991). Moreover, the larger and more evolved but paradoxically less massive members of Algol-type eclipsing binaries are thought to become so during a phase of mass transfer to their companions (Crawford, 1955).

A number of binary stellar evolution codes exist that allow to simulate the life of binary stars including mass transfer phases along with other binary effects such as mass accretion, CE evolution, SN kicks, and angular momentum losses (e.g., `BSE` (Hurley et al., 2002), `StarTrack` (Belczynski et al., 2008), `MESA` (Paxton et al., 2011), `binary_c` (Izzard et al., 2004)). Regarding the mass transfer, these codes typically build upon two assumptions. Firstly, the effect of any orbital eccentricity is neglected during the mass transfer phase. For circular orbits, there exists the well-established Roche-lobe limit which a star's radius has to exceed so that it loses mass to its companion (see Section 2.1.3, Eggleton, 1983). In turn, modelling the mass transfer rate on eccentric orbits in which the orbital separation oscillates is extremely difficult since mass transfer might occur partially within each orbit at varying rate and does back-react on the orbital elements

changing the eccentricity and semi-major axis. Recently, several promising attempts have been made to solve these difficulties (Sepinsky et al., 2007; Dosopoulou & Kalogera, 2016b,a; Hamers & Dosopoulou, 2019). Secondly, the rotational angular momentum vectors (spins) of the binary stars are assumed to be aligned with the orbital axis. This assumption has partly been made due to simplicity and partly because tidal interactions between the binary members are believed to diminish any spin-orbit misalignment (e.g., Hut, 1981). However, there is observational evidence of close binaries with highly inclined spin axes suggesting that tides are not in all cases able to align the spins with the orbital axis (e.g., BANANA survey, Albrecht et al., 2009).

Here, we question the second assumption of spin-orbit alignment. Based on the work of Matese & Whitmire (1983), we will show that if a binary undergoes a phase of mass transfer the mass-donating star actually loses rotational angular momentum in a way that causes its spin vector to flip onto the orbital plane.

We will apply this result to the evolutionary pathways of massive stars in close binaries. Isolated in the galactic field, these systems have been proposed as the progenitors of a formation channel (Klencki et al., 2021; Belczynski et al., 2016a; Mandel & de Mink, 2016; Dominik et al., 2012) leading to the BBH mergers observed by GW facilities (Abbott et al., 2019). In this scenario, mass transfer between the two stars precedes a CE phase in which the orbital separation quickly shrinks to values small enough for the BH remnants to merge in less than $\sim 10\,\mathrm{Gyr}$.

The orientation and magnitude of the BH spins constitute an important observable to discriminate among the different binary formation channels (e.g., Mandel & O'Shaughnessy, 2010; Gerosa et al., 2013; Rodriguez et al., 2016b; Zevin et al., 2020). For instance, the LIGO-Virgo detectors are sensitive to the mass-weighted projection of the BH spins onto the orbital angular momentum,

$$\chi_{\mathsf{eff}} = \frac{m_1\chi_1\cos\theta_1 + m_2\chi_2\cos\theta_2}{m}. \tag{4.1}$$

Here, $m_{1,2}$ are the two BH masses and m their sum. The spins are usually expressed in terms of the dimensionless spin parameters $\boldsymbol{\chi}_{1,2}$ whilst we will use the canonical rotational angular momenta $\boldsymbol{S}_{1,2}$ to describe those of their stellar progenitors. Both vectors are related as $\boldsymbol{S}_{1,2} = \boldsymbol{\chi}_{1,2}Gm_{1,2}^2/c$. The angles $\theta_{1,2} = \cos^{-1}\hat{\boldsymbol{S}}_{1,2}\cdot\hat{\boldsymbol{h}}$ describe the tilts of the spins with respect to the specific orbital angular momentum $\boldsymbol{h}$. A viable formation channel has to be compatible with the χ_{eff}-distribution of the BBH mergers measured by LIGO-Virgo which peaks around $\chi_{\mathsf{eff}} \simeq 0$ with a slight tendency towards positive values (Abbott et al., 2019, 2021a; The LIGO Scientific Collaboration et al., 2021). This suggests that the final BH spins are either small, anti-aligned with each other, or perpendicular to $\boldsymbol{h}$.

By means of a population synthesis we will apply the spin dynamics that we derived to the

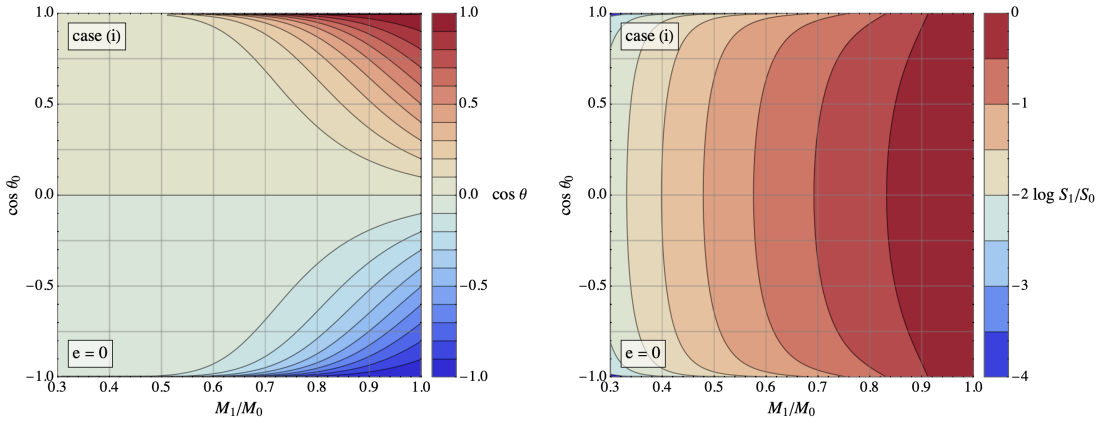

Figure 4.1. Donor spin evolution for a constant mass loss rate. We are considering circular orbits ($e = 0$). The quantities m_1 (m_0), S (S_0), and θ (θ_0) describe the current (initial) values of the donor's mass, spin magnitude, and tilt angle with respect to the specific orbital angular momentum $\boldsymbol{h}$, respectively. The left panel reveals that as the donor loses mass, i.e., m_1/m_0 decreases, any initial donor spin with $\cos\theta_0 \in (-1.0, 1.0)$ gets flipped towards the orbital plane $\cos\theta_0 = 0.0$. Meanwhile, the right panel shows how at the same time the spin magnitude efficiently gets damped down.

first stable mass transfer occurring in the isolated binary channel. There, we will also take other binary effects such as tidal interactions into account (Eggleton & Kiseleva-Eggleton, 2001) in order to investigate whether flipping spins are a prevalent phenomenon or not. Apart from that, we emphasise that the dynamics can be important for any other binary formation channel that might involve a phase of mass transfer, e.g., the triple channel (Di Stefano, 2020a), as well as for mass-exchanging stellar binaries in general.

4.2 Basic Assumptions

Here, we consider an isolated stellar binary in which one member star transfers mass to the other. We label all quantities related to the mass losing star (donor) and the mass-gaining star (accretor) with the indices $i = 1, 2$, respectively. Thus, let R_i, m_i, $\boldsymbol{r}_i$, and $\boldsymbol{d} = \boldsymbol{r}_2 - \boldsymbol{r}_1$ denote the stars' radii, masses, the distance between the stellar centres of mass to the binary centre of mass, and orbital separation, respectively. Together they carry a specific orbital angular momentum per reduced mass $\mu = m_1 m_2/m_{12}$ which is given by

$$\boldsymbol{h}(t) = \boldsymbol{d} \times \dot{\boldsymbol{d}}. \tag{4.2}$$

In terms of the semi-major axis a, eccentricity e, and total mass m_{12}, its magnitude can be written as

$$h = j\sqrt{Gm_{12}a}, \tag{4.3}$$

where $j = \sqrt{1-e^2}$. Furthermore, we associate with each star a rotational angular momentum vector (spin) given by

$$\boldsymbol{S}_i(t) = \sum_k \boldsymbol{\rho}_{i,k} \times (m_k \dot{\boldsymbol{\rho}}_{i,k}) = \sum_k \boldsymbol{\rho}_{i,k} \times (m_k \boldsymbol{\omega}_{i,k} \times \boldsymbol{\rho}_{i,k})\,. \tag{4.4}$$

The sums in Eq. (4.4) are taken over all particles with masses m_k, absolute positions $\boldsymbol{s}_{i,k}$, relative positions $\boldsymbol{\rho}_{i,k} = \boldsymbol{s}_{i,k} - \boldsymbol{r}_i$, and angular velocities $\boldsymbol{\omega}_{i,k}$ that constitute the star i at some time t. If we assume for simplicity that the stars retain spherically symmetric shapes during the mass transfer and uniformly rotate at some angular velocities $\boldsymbol{\omega}_i = \boldsymbol{\omega}_{i,k}$, one recovers the familiar form

$$\boldsymbol{S}_i(t) = \underline{\boldsymbol{\Theta}}_i \cdot \boldsymbol{\omega}_i, \tag{4.5}$$

where $\underline{\boldsymbol{\Theta}}_i = \kappa m_i R_i^2\, \underline{\mathbf{1}}$ is the respective star's total inertia tensor with $\underline{\mathbf{1}}$ being the identity. Henceforth, we set $\kappa = 0.08$ for a $n \sim 3$ polytrope (Motz, 1952).

In general, mass is transferred from the donor to the accretor via their first Lagrangian point L_1 once the former fills its Roche-lobe (Paczyński, 1971; Lubow & Shu, 1975). That is, the radius of the donor has to expand to the limit approximately given by (see Section 2.1.3, Eggleton, 1983)

$$R_L(t) = dF(q), \tag{4.6}$$

where $q = m_1/m_2$ is the stars' mass ratio and the function $F(q)$ is defined as

$$F(q) = \frac{0.49q^{2/3}}{0.6q^{2/3} + \ln\left(1+q^{1/3}\right)}. \tag{4.7}$$

Whenever the donor has grown to that size, $R_1 = R_L$, we assume that it loses mass at the point $\boldsymbol{R}_1 = R_1\hat{\boldsymbol{d}}$ at a rate $\dot{m}_1 = -\dot{m}$ where $\dot{m} > 0$ which subsequently gets transferred to the accretor (Matese & Whitmire, 1983). For simplicity, we assume that the mass transfer is conservative, i.e., no mass is lost from the binary during this process.

4.3 Donor spin evolution due to mass transfer

In this section we study the spin evolution of the donor based on the work of Matese & Whitmire (1983) and Sepinsky et al. (2010). For this reason and for better readability, we will henceforth

omit the donor's index $i = 1$ ($\boldsymbol{S} = \boldsymbol{S}_1$, $\boldsymbol{\omega} = \boldsymbol{\omega}_1$, $\boldsymbol{R} = \boldsymbol{R}_1$, etc.). Consider a general donor quantity G which at some time t can be written as $G(t) = \sum_k G_k(t)$, i.e., as a sum over all particles labeled with k that constitute the donor at that time (e.g., Eq. (4.4)). At a later time $t + \Delta t$, G will be given by $G(t + \Delta t) = \sum_{k'} G_{k'}(t + \Delta t)$, where

$$\sum_{k'} = \sum_{k} - \sum_{l} \tag{4.8}$$

is the sum over all particles that constitute the respective star at the later time $t + \Delta t$. That is, the donor lost the contribution of the particles labelled with l that left it within the time interval Δt. Consequently, the time derivative of $G(t)$ can be written as (Matese & Whitmire, 1983)

$$\dot{G} = \sum_k \dot{G}_k(t) - \lim_{\Delta t \to 0} \frac{1}{\Delta t} \sum_l G_l(t + \Delta t). \tag{4.9}$$

The first term on the r.h.s. of Eq. (4.9) describes the change of G if the mass were held constant, whereas the second term reflects the change due to mass transfer. Insertion of Eq. (4.4) into (4.9) yields $\dot{\boldsymbol{S}}(t) = \boldsymbol{\varepsilon}(t) - \boldsymbol{\zeta}(t)$ where we defined

$$\boldsymbol{\varepsilon}(t) = \sum_k \frac{\mathrm{d}}{\mathrm{d}t} \left\{ \boldsymbol{\rho}_k(t) \times [m_k \dot{\boldsymbol{\rho}}_k(t)] \right\}, \tag{4.10}$$

$$\boldsymbol{\zeta}(t) = \lim_{\Delta t \to 0} \frac{1}{\Delta t} \sum_l \boldsymbol{\rho}_l(t + \Delta t) \times [m_l \dot{\boldsymbol{\rho}}_l(t + \Delta t)]. \tag{4.11}$$

Physically, the first term $\boldsymbol{\varepsilon}(t)$ comprises all external torques applied to the donor spin if its total mass were held constant (Hrushow, 1969). These external torques can emerge, e.g., from the tidal forces of the companion star and will be discussed in Sections 4.4 and 4.5. In order to study the effect of mass loss alone we set $\boldsymbol{\varepsilon}(t) = 0$ in the remainder of this section. In that case, Eqs. (4.5) and (4.11) yield for the time derivative of the donor spin

$$\begin{aligned} \dot{\boldsymbol{S}}(t) &= -\dot{m} \boldsymbol{R} \times (\boldsymbol{\omega} \times \boldsymbol{R}) \\ &= -\dot{m} \left[R^2 \boldsymbol{\omega} - (\boldsymbol{R} \cdot \boldsymbol{\omega}) \boldsymbol{R} \right] \\ &= -\frac{1}{\kappa} \frac{\dot{m}}{m} S \left[\hat{\boldsymbol{S}} - \left(\hat{\boldsymbol{d}} \cdot \hat{\boldsymbol{S}} \right) \hat{\boldsymbol{d}} \right], \end{aligned} \tag{4.12}$$

since we approximated $\boldsymbol{R} = R\hat{\boldsymbol{d}}$ to be the first Lagrangian point where the donor loses its particles, i.e., $\boldsymbol{R} = \boldsymbol{\rho}_l$. Eq. (4.12) is equivalent to the derivations of Matese & Whitmire (1983) and partly uses Eq. (23) of Sepinsky et al. (2010). Here, we make two implicit key assumptions that are commonly used in the literature. Firstly, we assumed that the particles leave the donor through $\boldsymbol{R}$ at the donor's rotational velocity, i.e., at a velocity $\boldsymbol{\omega} \times \boldsymbol{R}$ in the frame co-rotating

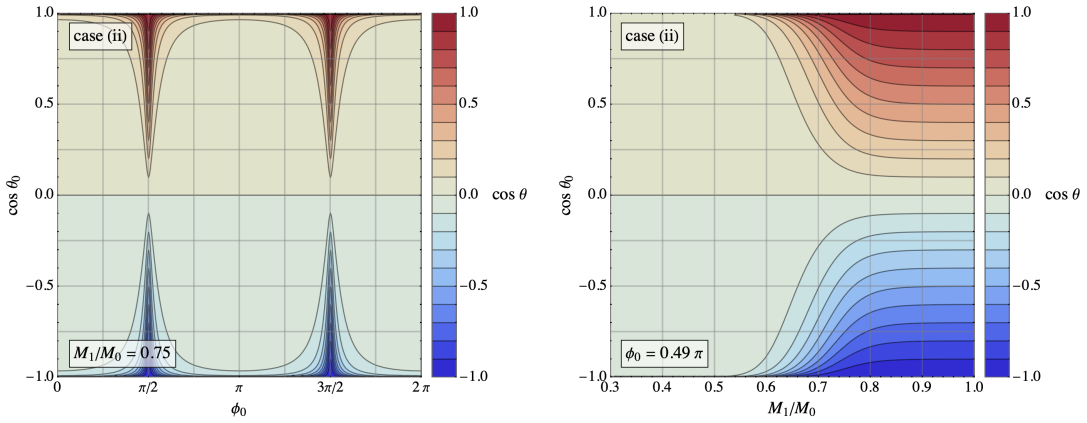

Figure 4.2. Donor spin evolution given that all mass is lost at the periapsis. The quantities m_1, m_0, θ, and θ_0 are defined as in Fig. 4.1 whilst ϕ_0 is the initial azimuthal angle of $\boldsymbol{S}$. For a fiducial fractional leftover mass of $m_1/m_0 = 0.75$, the left panel shows the additional dependency of the tilt angle evolution on the initial azimuthal angle ϕ_0, revealing that a flip onto the orbital plane is most (least) efficient if it is close to 0 or π ($\pi/2$ or $3\pi/2$). For the latter case ($\phi_0 = 0.49\pi$), the right panel shows that it requires smaller values of m_1/m_0 compared to Fig. 4.1 in order to achieve a significant flip. The opposite would be true if we were to plot the panel for ϕ_0 around 0 or π.

with the orbital motion (Sepinsky et al., 2010). Secondly, by replacing the angular velocity vector by the spin (cf., Eq. (4.5)) in the last step of Eq. (4.12) we assumed that the stellar interior transport of angular momentum is efficient enough to align the spins of all parts of the star on a timescale shorter than that of mass loss. Otherwise, the spin direction of some stellar parts, e.g., the core, could in principle decouple from the spin direction of the other parts, e.g., the envelope. We discuss the implications of these assumptions in Section 4.5.

The last part of Eq. (4.12) unveils a clear geometrical interpretation. The first term in the rectangular brackets causes the magnitude S of the donor spin to decrease. Meanwhile, the second term alters the spin direction unless $\hat{\boldsymbol{d}} \cdot \hat{\boldsymbol{S}} = 0$. Thus, depending on the orbital phase and the current spin direction, the second term causes the donor spin vector to either move towards the orbital plane or away from it. In what follows we will orbit-average the phase-dependent time-evolution equation (4.12) in order to investigate which effect dominates over longer timescales. We consider the two cases in which (i) $\dot{m}$ is constant within each orbit and (ii) all mass per orbit is lost at the periapsis. We note that on an eccentric orbit, $\dot{m}/m$ may vary smoothly along the orbit. For instance, it might be reasonable to assume that $\dot{m}$ has a local maximum and minimum at periapsis and apoapsis, respectively (Hamers & Dosopoulou, 2019). Detailed modelling of mass transfer in eccentric orbits is the subject of ongoing research which is beyond the scope of this work. Instead, we restrict ourselves to the two limiting cases (i) and (ii). We may assume that the former case is a valid approximation for circular and less eccentric systems whereas the latter

holds for more eccentric orbits.

In case (i), $\dot{m}/m$ and S only change on timescales that are much longer than the orbital period which is $T \lesssim \mathcal{O}(10^3)$ days for the systems we will be interested in (see Section 4.5). Hence, we can fix $\dot{m}/m$ and $\boldsymbol{S}$ when averaging Eq. (4.12) over one period. For that purpose, it is convenient to introduce a rotating reference frame $\mathfrak{F}$ by defining a right-handed orthonormal triad $(\hat{\boldsymbol{e}}, \hat{\boldsymbol{q}}, \hat{\boldsymbol{h}})$. Here, $\hat{\boldsymbol{e}}$ is the unit vector of the Laplace-Runge-Lenz vector $\boldsymbol{e}$ that has a magnitude equal to the orbit's eccentricity e and points towards its periapsis. Meanwhile, the unit vector $\hat{\boldsymbol{q}} = \hat{\boldsymbol{h}} \times \hat{\boldsymbol{e}}$ is along the latus rectum of the orbit. In this frame, $\hat{\boldsymbol{d}}$ and $\hat{\boldsymbol{S}}$ read in spherical coordinates

$$\hat{\boldsymbol{d}} = \cos\nu\hat{\boldsymbol{e}} + \sin\nu\hat{\boldsymbol{q}}, \tag{4.13}$$

$$\hat{\boldsymbol{S}} = \cos\phi\sin\theta\hat{\boldsymbol{e}} + \sin\phi\sin\theta\hat{\boldsymbol{q}} + \cos\theta\hat{\boldsymbol{h}}, \tag{4.14}$$

where $\phi \in [0, 2\pi)$ and $\theta \in [0, \pi]$ are the azimuthal and polar (tilt) angles of $\hat{\boldsymbol{S}}$, respectively. The angle $\nu \in [0, 2\pi)$ is the azimuthal angle of $\hat{\boldsymbol{d}}$ which is equivalent to the binary's orbital phase.

In general, the orbit-averaged change of some stellar quantity G over an orbit with eccentricity $0 \leq e < 1$ is given by (Dosopoulou & Kalogera, 2016b)

$$\langle \dot{G}(t) \rangle = \frac{(1-e^2)^{3/2}}{2\pi} \int_0^{2\pi} \frac{\dot{G}}{(1+e\cos\nu)^2}\,\mathrm{d}\nu. \tag{4.15}$$

For simplicity, we assume that also e does not change significantly on orbital timescales so that we can set $e = \text{const.}$ in the integral of Eq. (4.15). Thus, we find for the orbit-averaged change of $\boldsymbol{S}$

$$\langle \dot{\boldsymbol{S}}(t) \rangle = -\frac{1}{\kappa}\frac{\dot{m}}{m} S\{[1-f_1(e)]\cos\phi\sin\theta\hat{\boldsymbol{e}} + [1-f_2(e)]\sin\phi\sin\theta\hat{\boldsymbol{q}} + \cos\theta\hat{\boldsymbol{h}}\}, \tag{4.16}$$

where we defined $f_1(0) = f_2(0) = 1/2$, whereas for $0 < e < 1$ we have

$$f_1(e) = \frac{e^4 + 2e^2(j-1) - j + 1}{je^2}, \tag{4.17}$$

$$f_2(e) = \frac{(e^2-1)(j-1)}{e^2}, \tag{4.18}$$

whose difference is small and always negative, $0 > f_2(e) - f_1(e) > -1$. In terms of the spherical

coordinates of $\boldsymbol{S}$, Eq. (4.16) reads

$$\langle\dot{\theta}\rangle = \frac{1}{\kappa}\frac{\dot{m}}{m}\sin\theta\cos\theta\left[f_1(e)\cos^2\phi + f_2(e)\sin^2\phi\right], \tag{4.19}$$

$$\langle\dot{S}\rangle = -\frac{1}{\kappa}\frac{\dot{m}}{m}S\left\{1-\sin^2\theta\left[f_1(e)\cos^2\phi + f_2(e)\sin^2\phi\right]\right\}, \tag{4.20}$$

$$\langle\dot{\phi}\rangle = \frac{f_2(e)-f_1(e)}{\kappa}\frac{\dot{m}}{m}\sin\phi\cos\phi. \tag{4.21}$$

For the special case of circular, stationary orbits ($e = \langle\dot{e}\rangle = 0$), the integration of Eqs. (4.19)–(4.21) is particularly simple, yielding the analytical solutions

$$\theta = \tan^{-1}\left[\left(\frac{m}{m_0}\right)^{-1/2\kappa}\tan\theta_0\right], \tag{4.22}$$

$$S = S_0\left[\left(\frac{m}{m_0}\right)^{2/\kappa}\cos^2\theta_0 + \left(\frac{m}{m_0}\right)^{1/\kappa}\sin^2\theta_0\right]^{1/2}, \tag{4.23}$$

$$\phi = \text{const.}, \tag{4.24}$$

where $m_0 = m(t_0)$, $\theta_0 = \theta(t_0)$, and $S_0 = S(t_0)$ are the donor's mass, tilt angle, and spin magnitude at the onset of mass transfer, respectively. Importantly, θ and S are only functions of the initial tilt angle θ_0 and fractional leftover mass $0 \leq m/m_0 \leq 1$, i.e. the fraction between the donor's current and initial masses m and m_0, respectively. They are not explicit functions of time. Physically, this means that the details of the functional form of $\dot{m}(t)$ are irrelevant for $\theta(t)$ and $S(t)$ as long as the integrated mass loss is the same.

In Fig. 4.1, we plot $\cos\theta$ and S/S_0 for $e = 0$ as functions of m/m_0 and $\cos\theta_0$ revealing two essential features. Firstly, as the donor loses mass any initial tilt angle θ_0 gets flipped onto the orbital plane ($\cos\theta = 0$; see left panel). The only two exceptions are given by $\cos\theta_0 = -1$ and $+1$ for which $\cos\theta$ remains constant. However, the latter values constitute unstable equilibria since for any small deviation we do observe a flip. Moreover, in a realistic astrophysical setting these points are irrelevant because we will never start from perfect alignment of $\boldsymbol{S}$ and $\pm\boldsymbol{h}$. Most importantly, we see that the spin flip is very efficient in the sense that even moderate mass losses, e.g., $m/m_0 \simeq 0.75$, cause large changes of $\cos\theta$ towards zero unless $\cos\theta_0$ is very close to -1 or $+1$. Hence, the orbital plane is a strong dynamical attractor for the evolution of $\boldsymbol{S}$.

Secondly, the spin magnitude S of the donor gets efficiently damped down (see right panel). This is even true for $\cos\theta_0 = -1$ and $+1$. In fact, the closer $\cos\theta_0$ is to these values the stronger is the spin-down. Unless the mass loss is small the spin can decrease by several orders of magnitude.

Next, we investigate case (ii) in which all mass per orbit is lost at periapsis. To this end, we

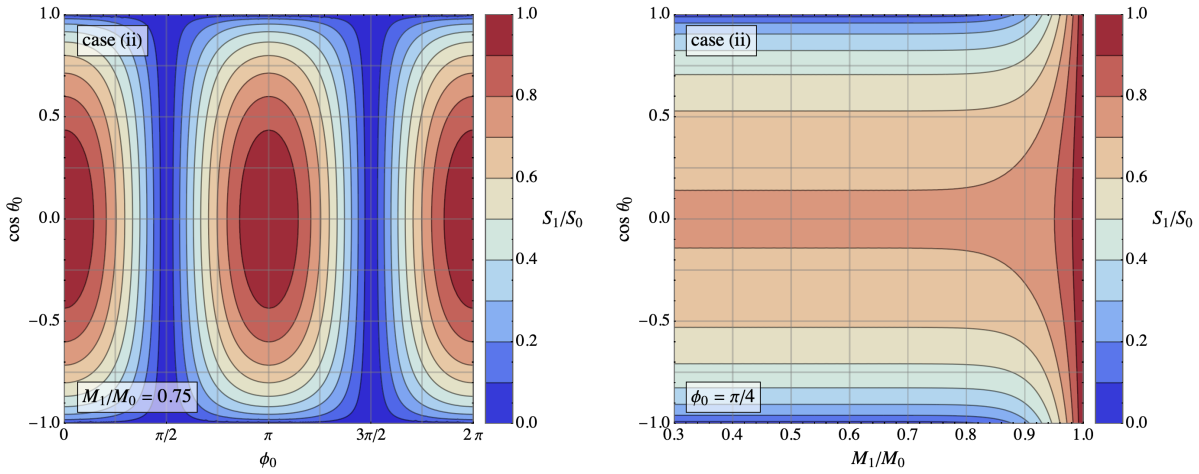

Figure 4.3. Donor spin-down if all mass is lost at the periapsis. All quantities are defined as in Figures 4.1 and 4.2. For $m_1/m_0 = 0.75$, the left panel shows the dependency on ϕ_0. We can see that the damping of the magnitude is most (least) efficient for $\pi/2$ or $3\pi/2$ (0 or π) whilst the opposite was true for the spin flip (e.g., Fig. 4.2, left panel). For the fiducial angle $\phi_0 = \pi/4$, the right panel shows that the spin magnitude gets damped down but much less efficiently than for the circular, constant mass loss rate case (Fig. 4.1).

introduce a mass loss rate $\dot{m}_0 > 0$ such that (Dosopoulou & Kalogera, 2016b)

$$\dot{m}(\nu) = \frac{\dot{m}_0}{2\pi}\delta(\nu), \tag{4.25}$$

where $\delta(\nu)$ is the Dirac-delta distribution. In this case, Eq. (4.15) yields for the donor spin,

$$\langle \dot{\boldsymbol{S}} \rangle = -\frac{1}{4\pi^2\kappa}\frac{(1-e^2)^{3/2}}{(1+e)^2}\frac{\dot{m}_0}{m} S \left(\sin\phi\sin\theta\hat{\boldsymbol{q}} + \cos\theta\hat{\boldsymbol{h}}\right). \tag{4.26}$$

In terms of the spherical coordinates we thus get

$$\langle \dot{\theta} \rangle = \frac{1}{\kappa}\frac{\langle \dot{m} \rangle}{m}\cos^2\phi\sin\theta\cos\theta, \tag{4.27}$$

$$\langle \dot{S} \rangle = -\frac{1}{\kappa}\frac{\langle \dot{m} \rangle}{m} S \left(\sin^2\phi\sin^2\theta + \cos^2\theta\right), \tag{4.28}$$

$$\langle \dot{\phi} \rangle = -\frac{1}{\kappa}\frac{\langle \dot{m} \rangle}{m}\sin\phi\cos\phi, \tag{4.29}$$

where we substituted the orbit-average of Eq. (4.25)

$$\langle \dot{m} \rangle = \frac{\dot{m}_0}{4\pi^2}\frac{(1-e^2)^{3/2}}{(1+e)^2}. \tag{4.30}$$

Note that since we defined $\dot{m}_0$ to be positive, the donor loses mass at a rate $-\langle \dot{m} \rangle$. Analogously

to Eqs. (4.19) – (4.24), we find analytical solutions to Eqs. (4.27) – (4.29) which are given by

$$\theta = \tan^{-1}\left\{\left[\left(\frac{m}{m_0}\right)^{-2/\kappa}\cos^2\phi_0 + \sin^2\phi_0\right]^{1/2}\tan\theta_0\right\}, \tag{4.31}$$

$$S = S_0 x^\alpha y^\beta, \tag{4.32}$$

$$\phi = \tan^{-1}\left[\left(\frac{m}{m_0}\right)^{1/\kappa}\tan\phi_0\right], \tag{4.33}$$

where we defined

$$x = \cos^2\phi_0\sin^2\theta_0 + \left(\frac{m}{m_0}\right)^{2/\kappa}\left(\cos^2\theta_0 + \sin^2\phi_0\sin^2\theta_0\right), \tag{4.34}$$

$$y = \frac{1}{4}\left[1 - \cos(2\theta_0) + 2\cos(2\phi_0)\sin^2\theta_0 + \left(\frac{m}{m_0}\right)^{2/\kappa}\left(3 + \cos(2\theta_0) - 2\cos(2\phi_0)\sin^2\theta_0\right)\right], \tag{4.35}$$

$$\alpha = \frac{1}{2 + 2\cot^2\theta_0\csc^2\phi_0}, \tag{4.36}$$

$$\beta = \frac{2\cos^2\theta_0}{3 + \cos(2\theta_0) - 2\cos(2\phi_0)\sin^2\theta_0}. \tag{4.37}$$

In the following, we investigate the implications of Eqs. (4.31) – (4.33). At first, note that these equations are not explicit functions of the eccentricity. Hence, their scope is only physically, but not mathematically, restricted to eccentricities that must be large enough so that Eq. (4.25) provides a valid approximation for the mass loss rate. Yet, Eqs. (4.31) – (4.33) are more complicated to analyse than Eqs. (4.22) – (4.24) due to their additional dependency on ϕ_0. The dependency of the tilt angle is shown in the left panel of Fig. 4.2 where we fixed $m/m_0 = 0.75$. It reveals that the flip is more efficient the closer the spin starts around the periapsis or apoapsis, i.e., around $\phi_0 = 0$ or π, respectively, whilst it does not flip at all if $\phi_0 = \pi/2$ or $3\pi/2$. The limiting behaviour at these values becomes evident from Eqs. (4.27) and (4.29). If ϕ_0 is an integer or half-integer multiple of π, ϕ becomes stationary ($\langle\dot{\phi}\rangle = 0$) since $\sin\phi\cos\phi = 0$ for these cases. Therefore, $\langle\dot{\theta}\rangle$ scales with a constant factor $\cos^2\phi_0$ which is zero or one if ϕ_0 is an half-integer or integer multiple of π, respectively. In the right panel of Fig. 4.2, we plot $\cos\theta$ for $\phi_0 = 0.49\pi$, i.e., for an initial azimuthal angle close to a half-integer minimum. We see that it requires smaller values of m/m_0 compared to Fig. 4.1 in order to achieve a significant flip. The opposite would be true if we were to plot the panel for ϕ_0 around 0 or π.

In Fig. 4.3, we show the spin magnitude evolution. In the left panel, we show its dependency on ϕ_0 for $m/m_0 = 0.75$. Whilst we explained above that the spin flip is most (least) efficient if

ϕ_0 is an integer (half-integer) multiple of π, respectively, the opposite is true for the spin-down. In the right panel, we show for $\phi_0 = \pi/4$ the spin-down as a function of $\cos\theta_0$. In comparison to the circular, constant mass loss rate case (Fig. 4.1), the spin-down is weaker leading to a typical fraction of about $S_1/S_0 \sim \mathcal{O}(0.1)$. Furthermore, there is a mass loss scale of about $m/m_0 \simeq 0.8$ below which the spin-down no longer depends on m/m_0. At this value, terms that are proportional to $(m/m_0)^{2/\kappa}$ become negligible in Eqs. (4.34) and (4.35) so that S/S_0 solely depends on θ_0 and ϕ_0. In this regime, the spin-down is the most (least) efficient if the spin is oriented towards the poles (orbital plane).

4.4 Tides

In a close semi-detached binary tidal bulges can emerge on the surface of a star because of the perturbing force of its companion. Due to the viscosity of the star these bulges will not instantaneously align with the relative distance vector $\boldsymbol{d}$ but they either slightly lag behind or lead ahead depending on whether its rotational angular frequency ω is smaller or greater than the orbital mean motion $n = 2\pi/T$, respectively (Alexander, 1973; Zahn, 1977; Hut, 1981). Further bulges arise at the star's equator due to its rotation introducing at lowest order a quadrupolar perturbation to the gravitational potential. Applying both effects to the donor star, the equations of motion for the evolution of the stellar spin and binary angular momentum are described by a set of differential equations for $\boldsymbol{S}$, $\hat{\boldsymbol{e}}$, $\hat{\boldsymbol{q}}$, $\hat{\boldsymbol{h}}$, e, and h as follows

$$\frac{\mathrm{d}\boldsymbol{S}}{\mathrm{d}t} = \left.\frac{\mathrm{d}\boldsymbol{S}}{\mathrm{d}t}\right|_{\dot{m}} + \left.\frac{\mathrm{d}\boldsymbol{S}}{\mathrm{d}t}\right|_{\text{Quad}} + \left.\frac{\mathrm{d}\boldsymbol{S}}{\mathrm{d}t}\right|_{\text{Diss}}, \tag{4.38}$$

$$\frac{\mathrm{d}\hat{\boldsymbol{u}}}{\mathrm{d}t} = \left.\frac{\mathrm{d}\hat{\boldsymbol{u}}}{\mathrm{d}t}\right|_{\text{Quad}} + \left.\frac{\mathrm{d}\hat{\boldsymbol{u}}}{\mathrm{d}t}\right|_{\text{Diss}}, \tag{4.39}$$

$$\frac{\mathrm{d}e}{\mathrm{d}t} = \left.\frac{\mathrm{d}e}{\mathrm{d}t}\right|_{\dot{m}} + \left.\frac{\mathrm{d}e}{\mathrm{d}t}\right|_{\text{Diss}}, \tag{4.40}$$

$$\frac{\mathrm{d}h}{\mathrm{d}t} = \left.\frac{\mathrm{d}h}{\mathrm{d}t}\right|_{\dot{m}} + \left.\frac{\mathrm{d}h}{\mathrm{d}t}\right|_{\text{Diss}}, \tag{4.41}$$

where $\hat{\boldsymbol{u}}$ is used as a proxy for $\hat{\boldsymbol{e}}$, $\hat{\boldsymbol{q}}$, and $\hat{\boldsymbol{h}}$, respectively. For simplicity, we ignore tides raised on the acceptor star which are much weaker than the tides raised on the donor. Each term in Eqs. (4.38) – (4.41) either emerges from the mass transfer (indicated by "$\dot{m}$"), the quadrupolar distortion of the donor ("Quad"), or the tidal dissipation ("Diss"). The mass transfer term for $\boldsymbol{S}$ is either given by Eq. (4.16) (case (i)) or (4.26) (case (ii)). In addition, conservative mass transfer

causes the magnitude of the specific angular momentum to change as (Eggleton, 2006)

$$\left.\frac{\mathrm{d}h}{\mathrm{d}t}\right|_{\dot{m}} = \dot{m}\left(\frac{1}{m_1} - \frac{1}{m_2}\right)h. \tag{4.42}$$

Meanwhile, the mass transfer term for the eccentricity depends on how the mass loss rate changes along the orbit. If the rate is independent on the orbital phase as in case (i), then (Eggleton, 2006)

$$\left.\frac{\mathrm{d}e}{\mathrm{d}t}\right|_{\dot{m}} = 0, \tag{4.43}$$

whereas for the delta-mass function case (ii), it can be written as (Sepinsky et al., 2007; Dosopoulou & Kalogera, 2016b)

$$\left.\frac{\mathrm{d}e}{\mathrm{d}t}\right|_{\dot{m}} = -\frac{\dot{m}}{m_1}\frac{R}{a}j + 2\dot{m}\left(\frac{1}{m_1} - \frac{1}{m_2}\right)j(1-e), \tag{4.44}$$

where we treated the accretor as a point mass. In any case, the orientation of the orbital frame $\mathfrak{F}$ remains unaffected by the mass transfer (Eggleton, 2006). Hence, Eq. (4.39) involves no term in this regard.

Together, the terms for the quadrupolar distortion and tidal dissipation can be conveniently expressed by means of five perturbing functions X, Y, Z, V, and W which we explicate in Appendix A.5 (Eggleton & Kiseleva-Eggleton, 2001; Eggleton, 2006) and which is equivalent to the prescription given in Chapter 2

$$\left.\frac{\mathrm{d}\boldsymbol{S}}{\mathrm{d}t}\right|_{\text{Quad}} + \left.\frac{\mathrm{d}\boldsymbol{S}}{\mathrm{d}t}\right|_{\text{Diss}} = \mu h(W\hat{\boldsymbol{h}} - \boldsymbol{K}\times\hat{\boldsymbol{h}}), \tag{4.45}$$

$$\left.\frac{\mathrm{d}\hat{\boldsymbol{u}}}{\mathrm{d}t}\right|_{\text{Quad}} + \left.\frac{\mathrm{d}\hat{\boldsymbol{u}}}{\mathrm{d}t}\right|_{\text{Diss}} = \boldsymbol{K}\times\hat{\boldsymbol{u}}, \tag{4.46}$$

$$\left.\frac{\mathrm{d}e}{\mathrm{d}t}\right|_{\text{Diss}} = -Ve, \tag{4.47}$$

$$\left.\frac{\mathrm{d}h}{\mathrm{d}t}\right|_{\text{Diss}} = -Wh, \tag{4.48}$$

where $\boldsymbol{K} = X\hat{\boldsymbol{e}} + Y\hat{\boldsymbol{q}} + Z\hat{\boldsymbol{h}}$ is the angular velocity of $\mathfrak{F}$. Of the perturbing functions, V and W are due to tidal dissipation which cause the orbit to circularise and the stellar rotation to synchronise. The functions X, Y, and Z incorporate the quadrupolar distortion which gives rise to apsidal motion and spin precession around $\hat{\boldsymbol{h}}$. However, also X and Y do include small terms due to tidal dissipation which enforce the spin to align with the orbital angular momentum.

Hence, the effect of tidal dissipation counteracts the flip of the donor spin due to mass transfer, i.e., its misalignment with $\hat{\boldsymbol{h}}$. Therefore, any spin flip is suppressed unless the mass transfer terms in Eq. (4.38) are able to dominate the others. In the following, we address in which circumstances this might happen.

In the equilibrium tide model the tidal friction timescale t_{F} is defined as (Fabrycky & Tremaine, 2007)

$$t_{\mathsf{F,e}} = \frac{t_{\mathsf{V}}}{9}\left(\frac{a}{R}\right)^8 \frac{m_1^2}{m_2 m_{12}} \frac{1}{(1+2k_{\mathrm{A}})^2}, \tag{4.49}$$

where $k_{\mathrm{A}} = 0.014$ is the apsidal motion constant which quantifies the quadrupolar deformability of a star and t_{V} is the viscous timescale given by

$$t_{\mathsf{V}} = 3\frac{(1+2k_A)^2}{k_A}\frac{R^3}{Gm_1\tau}. \tag{4.50}$$

Physically, τ describes the time by which the tidal bulges lag behind or lead ahead w.r.t. the line connecting both binary members. In the theory of equilibrium tides, τ is a constant which is an intrinsic property of the tidally forced star in question (Hut, 1981).

We also consider an approximate prescription for dynamical tides which could become important for stars with outer radiative envelopes (Zahn, 1977). Following Hurley et al. (2002), in this case we still use the equations from Eggleton & Kiseleva-Eggleton (2001) but with the tidal dissipation timescale now given by

$$t_{\mathsf{F,d}} = \left(\frac{a}{R}\right)^9 \sqrt{\frac{a^3}{Gm_1}} q \left(1+\frac{1}{q}\right)^{-11/6} \frac{1}{E_2}, \tag{4.51}$$

where E_2 is a coefficient that is related to the structure of the star and refers to the coupling between the tidal potential and gravity mode oscillations. Unfortunately, the value of E_2 is difficult to calculate since it is very sensitive to the structure of the star and therefore to the exact treatment of stellar evolution (e.g., Zahn, 1975; Yoon et al., 2010; Siess et al., 2013; Qin et al., 2018).

We can approximately quantify the effect of tides on the stellar spin by introducing a timescale for variations in the spin-orbit tilt angle due to tidal dissipation, $t_{\mathrm{S,e(d)}} \sim (S/\mu h) t_{\mathrm{F,e(d)}} j^{13}$. Thus, for a star which just fills its Roche-lobe, i.e., $R = F(q)a(1-e)$, and for the equilibrium tide model we have

$$t_{S,\mathrm{e}} = 1.6\times10^{-2}\,\mathsf{yr}\frac{\kappa}{0.08}\frac{0.014}{k_{\mathrm{A}}}\left(\frac{1\,\mathrm{s}}{\tau}\right)\left(\frac{1\,\mathrm{day}}{P}\right)\left(\frac{\mathrm{M}_\odot^{3/2}}{m_2\sqrt{m_{12}}}\right)\left(\frac{a}{\mathrm{R}_\odot}\right)^{9/2}\frac{qj^{12}}{\left[F(q)(1-e)\right]^3}, \tag{4.52}$$

where $P = 2\pi/\omega$. For the dynamical tide model we find

$$t_{S,\mathrm{d}} = 4.4 \times 10^2\,\mathrm{yr}\frac{\kappa}{0.08}\left(\frac{10^{-9}}{E_2}\right)\left(\frac{1\,\mathrm{day}}{P}\right)\left(\frac{\sqrt{m_1 m_{12}}}{m_2^2}\,\mathrm{M}_\odot\right)\left(\frac{a}{\mathrm{R}_\odot}\right)^3 \frac{j^{12}}{\left[F(q)(1-e)\right]^7}\left(\frac{m_2}{m_{12}}\right)^{11/6}. \tag{4.53}$$

We then compare the above timescales to the timescale for spin change due to mass loss, $t_{\dot{m}} \sim \kappa m_1/\dot{m}$. From the condition $t_{\dot{m}} = t_{S,\mathrm{e(d)}}$, we have that the mass loss effect dominates over tidal effects if at the onset of mass transfer the binary semi-major axis is larger than

$$a_\mathrm{e} = 11.9\,\mathrm{R}_\odot\left(\frac{k_\mathrm{A}}{0.014}\frac{\tau}{1\,\mathrm{s}}\frac{10^{-4}\,\mathrm{M}_\odot\,\mathrm{yr}^{-1}}{\dot{m}}\frac{P}{1\,\mathrm{day}}\right)^{2/9}\left(\frac{m_2^2\sqrt{m_{12}}}{\mathrm{M}_\odot^{5/2}}\right)^{2/9}\frac{\left[F(q)(1-e)\right]^{2/3}}{j^{8/3}}, \tag{4.54}$$

for equilibrium tides, and larger than

$$a_\mathrm{d} = 1.2\,\mathrm{R}_\odot\left(\frac{E_2}{10^{-9}}\frac{10^{-4}\,\mathrm{M}_\odot\,\mathrm{yr}^{-1}}{\dot{m}}\frac{P}{1\,\mathrm{day}}\frac{m_2^2 m_1}{\sqrt{m_1 m_{12}}\,\mathrm{M}_\odot^2}\right)^{1/3}\frac{\left[F(q)(1-e)\right]^{7/3}}{j^4}\left(\frac{m_{12}}{m_2}\right)^{11/18}, \tag{4.55}$$

for dynamical tides.

In Fig. 4.4, we plot a_e and a_d as a function of the donor mass. In this calculation, we consider circular equal-mass binaries. For the lag time constant we use $\tau = 10^{-1}\,\mathrm{s}$ which is a value typically adopted for solar type stars (e.g., Wu & Murray, 2003; Anderson et al., 2017), and set $E_2 = 10^{-9}\left(m_1/\,\mathrm{M}_\odot\right)^{2.8}$ which was obtained by Zahn (1977) for ZAMS stars. Although a_e and a_d depend weekly on τ and E_2 respectively, it is important to note that plausible values for these parameters can span orders of magnitude (e.g., Goldreich & Soter, 1966; Zahn, 1977). Moreover, we set $\dot{m} = 10^{-4}\,\mathrm{M}_\odot\,\mathrm{yr}^{-1}$ which is a realistic value for RLO. According to Kippenhahn et al. (1967) a $9\,\mathrm{M}_\odot$ donor loses more than $5\,\mathrm{M}_\odot$ to a $5\,\mathrm{M}_\odot$ accretor in only $6 \times 10^4\,\mathrm{yr}$ during the hydrogen burning and almost $7\,\mathrm{M}_\odot$ in $4 \times 10^4\,\mathrm{yr}$ when the mass transfer starts after exhaustion of hydrogen in the core. Paczyński (1967a) and van Rensbergen et al. (2010) find similar mass transfer rates for MS donors. The mass loss rate can be as large as $10^{-1}\,\mathrm{M}_\odot\,\mathrm{yr}^{-1}$ in the case of massive binaries (e.g., Figure 1 of Belczynski et al., 2016a).

Fig. 4.4 shows that a_e varies between several tens to $\sim 100\,\mathrm{R}_\odot$, increasing weakly with the mass of the donor, whilst a_d varies between $a_\mathrm{d} \simeq 2\,\mathrm{R}_\odot$ for a $2\,\mathrm{M}_\odot$ donor up to $a_\mathrm{d} \simeq 400\,\mathrm{R}_\odot$ for the most massive stars. We can now ask whether during a given evolutionary stage a mass transfer episode can occur at such, or smaller, orbital separations; this requires that $R/F(q)(1-e) > a_\mathrm{e(d)}$. In Fig. 4.4 we compute $R_\mathrm{MS}/F(q)$ and $R_\mathrm{RG}/F(q)$, where R_MS is the maximum stellar radius during the MS and R_GB is the radius at the start of He burning, as a function of the mass of the star at that evolutionary stage. The stellar radii were obtained with the fast binary stellar evolution code `BSE` (Hurley et al., 2002; Banerjee et al., 2020). Hence, $R_\mathrm{MS}/F(q)$ and $R_\mathrm{RG}/F(q)$

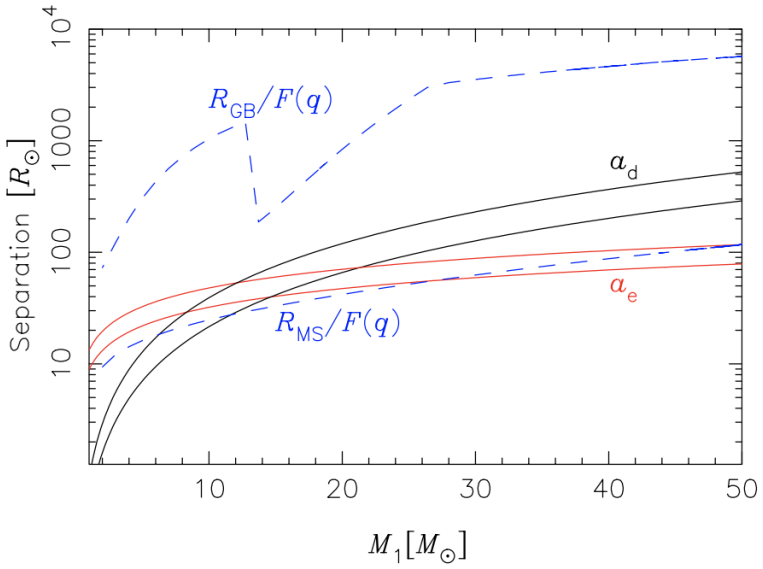

Figure 4.4. Critical binary semi-major axis a_e and a_d for a spin rotational period $P = 5\,\mathrm{days}$ (lower lines) and $P = 30\,\mathrm{days}$ (upper lines). Tides are expected to suppress the flip of the stellar spin due to mass loss if mass transfer starts at $a < a_e$ and $a < a_d$ for equilibrium and dynamical tides, respectively. The dashed blue lines give the maximum value of the binary semi-major axis that will still allow a mass transfer event to occur on the MS, $R_{MS}/F(q)$, and before He burning starts, $R_{GB}/F(q)$. Here, we consider circular binaries with $e = 0$, $q = 1$, and solar metallicity. Other parameters and details are given in Section 4.4.

represent the maximum value of the binary semi-major axis that will still allow a mass transfer event to happen during the MS or before He burning starts, respectively. Comparing these to the red and black lines in the figure, we see that the effect of mass loss can indeed be important for both MS and giant stars. If mass transfer starts near the tip of the giant branch, then the mass loss effect will dominate regardless of the exact treatment of tides. Even for MS stars, however, the mass loss effect can become comparable to tides for a large range of masses and dominates in some cases. For example, radiative damping on the dynamical tide is expected to be the most efficient dissipative mechanism in MS stars with $m_1 \gtrsim 1.5\,\mathrm{M}_\odot$. For these stars and for masses up to $m_1 \approx 5\,\mathrm{M}_\odot$, $R_{MS}/F(q) \gg a_d$ so that mass loss effects will dominate.

In conclusion, the results shown in this section demonstrate that the assumption that tides will erase any spin-orbit misalignment might not always be valid. In the following section, we will consider how the spin dynamics we described above can affect the spin-orbit alignment of BBHs formed from the evolution of field binaries.

Table 4.1. Initial parameter distribution of the binary population. The primary mass is drawn from the Kroupa (2002) initial mass function whilst the distributions for the mass ratio, eccentricity, and orbital period are adopted from Sana et al. (2012). Note that the observational sample used by Sana et al. (2012) only allowed for a statistical analysis of binaries with primary masses up to $60\,\mathrm{M}_\odot$. Here, we explicitly assume that the distributions are valid up to primary masses of $100\,\mathrm{M}_\odot$. The exponents $\varkappa$, η, and λ are assumed to follow normal distributions, i.e., for each binary instance we draw new values from normal distributions with means and standard deviations as given in the Table.

Parameter	Distribution	Exponent	Domain
Primary mass m_1	$P_{m_1} \propto m_1^{\varsigma}$	$\varsigma = -2.3$	$22 - 100\,\mathrm{M}_\odot$
Mass ratio m_2/m_1	$P_{m_2/m_1} \propto (m_2/m_1)^{\varkappa}$	$\varkappa = -0.2 \pm 0.6$	$0.1 - 1.0$
Eccentricity e	$P_e \propto e^{\eta}$	$\eta = -0.4 \pm 0.2$	$0.0 - 0.9$
Orbital period T	$P_{\log T/\mathrm{days}} \propto (\log T/\mathrm{days})^{\lambda}$	$\lambda = -0.4 \pm 0.2$	$10^{0.15} - 10^{3.5}$ days

4.5 Application to binary black hole formation

In this section, we simulate a population of isolated massive stellar binaries and use Eqs. (4.38) – (4.41) to investigate the implications of the spin dynamics described above. As in Chapter 3, the population is set up using the parameter distributions that Sana et al. (2012) inferred from the observation of 71 Galactic binaries. That is, we draw the primary masses, mass ratios, orbital periods, and eccentricities from the distribution functions given in Table 4.1. In the remainder of this section, we will refer to the star (and its compact remnant) that was initially the more massive one as the primary and to its companion as the secondary.

We evolve this binary population in time by means of the binary stellar evolution code `BSE` (Hurley et al., 2002; Banerjee et al., 2020). As described in the previous chapters, `BSE` simulates the stellar evolution including binary features such as mass transfer, mass accretion, CE evolution, SN kicks, and angular momentum losses. For the subset of systems that form merging BBHs through the isolated binary channel, interactions among the stellar binary members played a vital role (e.g., Belczynski et al., 2016a). Briefly, starting with two massive stars in the galactic field the primary star transfers mass to the secondary during a dynamically stable RLO phase. Soon after this process the primary star forms a (first-born) BH whereas the secondary expands as a supergiant. A second mass transfer phase from the secondary star to the BH takes place once the former fills its Roche-lobe. This time, the process is dynamically unstable leading to a CE phase in which the expanding star engulfs its BH companion. Whilst moving through the CE, drag forces cause the BH's orbit quickly to shrink and the CE might be ejected. Eventually, a BBH forms once the secondary star develops a BH, too. On this evolutionary pathway it is the CE phase which is of crucial importance for the BBH to finally merge. It can rapidly reduce the orbital separation to values small enough for energy loss due to GW emission to provoke a coalescence

within the age of the Universe.

In total, Eqs. (4.38) – (4.41) constitute a set of fourteen coupled differential equations (vectorial quantities counting thrice) that we numerically integrate once RLO starts. At that time, we use the masses, orbital parameters, and spin rates computed by BSE as the initial values for our integration scheme. Furthermore, we draw the initial value ϕ_0 for the azimuthal angle of the donor from a uniform distribution between zero and 2π. For the initial value of $\cos\theta_0$ of the tilt angle, we assume a uniform distribution in the interval $[0.9, 1.0)$. Thus, our approach is conservative in the sense that we start with donor spins which are fairly aligned with the orbital angular momentum. During the integration, we follow Hurley et al. (2002) by using $R = a(1 - e)F(q)$ as the effective donor radius. For comparison, we also ran a simulation using $R = aF(q)$ without noticing a substantial difference of the results. The mass loss rate we adopted is also obtained from the BSE calculation. This is, however, based on the assumption that the binary moves on a circular orbit which is not always the case for our binaries. Nonetheless, for want of a more detailed treatment we assume that this mass loss rate is still applicable to our eccentric systems. In particular, the BSE mass loss rate is used for the orbit-average given by Eq. (4.30) in case (ii).

Because the physics of stellar tides is much debated and the efficiency of tides itself is uncertain (e.g., Claret & Cunha, 1997; Langer, 2009), in the simulations presented here we opt for a simplified approach in which we employ the equilibrium tide equations for all stars. Then we use the constant time lag as a free parameter in order to tune the efficiency of tides. We set $\tau = 10^0$ s (efficient tides), $\tau = 10^{-1}$ s (moderately efficient tides), and $\tau = 10^{-2}$ s (inefficient tides). For $m_1 = 50\,\mathrm{M}_\odot$, $R = 10\,\mathrm{R}_\odot$, and $\tau = 10^0$ s, Eq. (4.50) gives a viscous time $t_\mathrm{V} \simeq 360\,\mathrm{yr}$.

Before presenting the results of our analysis, we comment on some assumptions in our treatment that we briefly introduced in Section 4.2 and that are also commonly adopted in the literature. Firstly, because the extent to which the rotation of the stellar core is coupled to that of the stellar envelope is very uncertain, we simply assume maximal coupling, i.e., that the entire star behaves as a rigid rotator with a uniform angular velocity (Steinle & Kesden, 2021; Sepinsky et al., 2010; Belczynski et al., 2008; Hurley et al., 2000; Belczynski et al., 2020), but comment here on the other extreme case of minimal coupling in which core and envelope are fully decoupled. As long as a star remains homogeneous, various processes (e.g., shear instability) will tend to rapidly restore uniform rotation. Thus, when the stars are on the MS the assumption of solid rotation might represent a good approximation. But, once the star leaves the MS it will then develop a compact He rich core whose rotation could fully decouple from that of the envelope before any significant amount of mass has been lost by the donor. The validity of our treatment for post MS stars therefore requires that mass and angular momentum transport within the star are efficient enough that the stellar core remains strongly coupled to the outer envelope. The angular momentum

evolution of stellar interiors, along with the resulting rotation rates of stellar remnants, remains poorly understood. However, several studies have shown that angular momentum transport within massive stars might be efficient enough to carry a significant amount of spin from the core to the envelope (e.g., Qin et al., 2018; Fuller & Ma, 2019). In this case, a spin tilt predicted by our model will reflect onto the spin of the core as well, although the latter might still rotate at a somewhat different angular frequency and at a different angle than the envelope. If the core and envelope are fully decoupled, we would expect that the core will keep rotating in the same direction as the entire star at the onset of mass transfer. The relative orientation between the spins of the binary stars and their orbital angular momentum then will largely depend on whether tides were efficient enough to realign any prior spin-orbit tilt, and on the primordial spin-orbit alignment.

Secondly, following Sepinsky et al. (2007, 2010) and Dosopoulou & Kalogera (2016b,a) we assume that any orbital angular momentum carried by the loss particles is immediately returned (only) to the orbit once they have passed the first Lagrangian point. Generally, mass transfer becomes non-conservative if not all mass lost from the donor can be accreted by its companion (Tout, 2012). In this case, the systemic mass and angular momentum losses would change the orbital elements differently compared to a conservative mass transfer. Sepinsky et al. (2009) showed for the case where all mass per orbit is lost at periapsis that the orbit would expand (contract) faster (slower). They found the same tendency for the growth (damping) of the eccentricity. Meanwhile, we showed in Section 4.3 that the donor spin dynamics foremostly depends on the donor's fractional mass loss rate. Thus, we expect our results to change under the consideration of non-conservative mass transfer only if the orbital elements are able to alter the latter significantly compared to the conservative case.

In the following, we present the results of our analysis. As a typical example, we show in Fig. 4.5 the spin flip during the mass transfer phase of a binary at low metallicity ($Z = 0.03\ \mathrm{Z}_\odot$) modelled with case (i) and a tidal lag time of $\tau = 10^{-1}$ s. This system started on the ZAMS ($t = 0$) with stellar masses, eccentricity, and orbital period set to $m_1 = 55\,\mathrm{M}_\odot$, $m_2 = 45\,\mathrm{M}_\odot$, $e = 0.1$, and $T = 10^2$ days, respectively. The mass transfer phase in question lasts from 4.37 to 4.48 Myr. In this period of time, the donor transfers about 60 per cent of its mass to the accretor (first panel). The normalised components of the donor spin in some inertial frame are shown in the second panel. This inertial frame is chosen such that the z-axis initially points along $\hat{\boldsymbol{h}}$. However, even at later time their directions will not deviate significantly from one another since $\boldsymbol{K}$ stays almost parallel to $\hat{\boldsymbol{h}}$ during the process. Thus, the reduction of $\hat{S}_z$ from about one to zero indicates the flip onto the orbital plane which can be also directly seen by the evolution of the cosine of the tilt angle, $\cos\theta = \hat{\boldsymbol{S}} \cdot \hat{\boldsymbol{h}}$ (third panel). The oscillations of the other two components describe the spin precession around $\hat{\boldsymbol{h}}$. Meanwhile, in terms of the dimensionless

parameter $\chi = cS/Gm_1^2$ the fourth panel shows that the donor spin magnitude decreases by approximately two orders of magnitude ending up at a value $\chi \sim \mathcal{O}(0.1)$. Evidently, the value of χ at the onset and hence also at the end of the mass transfer phase depend on its initial value $\chi(t = 0)$ and any torques which affect the spin until onset. Here, the initial spin is determined by a fit to the rotational velocities of MS star data (Lang, 1992) following Hurley et al. (2000). Starting with that value, BSE computes the subsequent spin evolution taking angular momentum losses due the isotropic stellar winds and tidal interactions with the companion into account (cf. Section 4.4).

After a second mass transfer phase from m_2 to m_1 starting at $5.76\,\mathrm{Myr}$ which leads to a CE evolution, this system evolves to a BBH at $6.12\,\mathrm{Myr}$ that merges after $\sim 6\,\mathrm{Gyr}$ due to the emission of GWs.

In Fig. 4.6, we show the primary star tilt angles for the whole binary population considering only those systems that according to BSE eventually develop BBHs. For each system, the value of the tilt angle is taken once the primaries stop transferring mass to their secondaries. If there was no mass transfer from the former to the latter we draw a random value from the initial value distribution of $\cos\theta_0$ between 0.9 and 1.0 (see above). Each histogram drawn with a solid line comprises 10^4 systems either at low ($Z = 0.03\ \mathrm{Z}_\odot$) or high metallicity ($Z = \mathrm{Z}_\odot$), whose lag time τ is either set to 10^0, 10^{-1}, or $10^{-2}\,\mathrm{s}$, and whose mass transfer is either modelled with case (i) or case (ii). We emphasise that the bin width of 0.1 is chosen such that the rightmost bin ($\cos\theta = 0.9 - 1.0$) covers the range of initial angles. Thus, spins ending up in any other bin ($\cos\theta < 0.9$) were dominated by the mass transfer terms. As a results, we find that any distribution is strongly bimodal with most of the primary spins either being flipped ($\cos\theta \lesssim 0.1$) or remaining aligned ($\cos\theta \gtrsim 0.9$). From longer to shorter lag times tides become weaker and allow the balance between the two peaks to pivot from the majority of systems being aligned to flipped. Thus, the means of the distributions indicated by the vertical solid lines shift from about $\cos\theta \sim 0.7$ to 0.8 ($\tau = 10^0\,\mathrm{s}$) to ~ 0.5 to 0.6 ($\tau = 10^{-1}\,\mathrm{s}$) and ~ 0.4 to 0.5 ($\tau = 10^{-2}\,\mathrm{s}$) for low metallicity. For high metallicity, the spin flips are more effective ranging from $\cos\theta \sim 0.5$ to 0.7 ($\tau = 10^0\,\mathrm{s}$) to ~ 0.3 to 0.4 ($\tau = 10^{-1}\,\mathrm{s}$) and ~ 0.1 to 0.2 ($\tau = 10^{-2}\,\mathrm{s}$). In reality, the relative number of flipped spins therefore depends on the precise value of the lag time. In turn, we do not see any major difference between our two models (i) and (ii) of mass transfer. Even though we pointed out that these models are arguably approximate with the caveats given above, the latter fact indicates that details about the orbital phase dependency of mass transfer might not play an important role for the effect that we are investigating.

In general, flipping spins are less numerous in the subsets of binaries whose BH remnants would coalesce within $10\,\mathrm{Gyr}$ (near the peak of cosmic star-formation rate, e.g., (Madau & Dickinson, 2014)) taken as a rough criterion for observability by GW detectors. Yet, the following results are

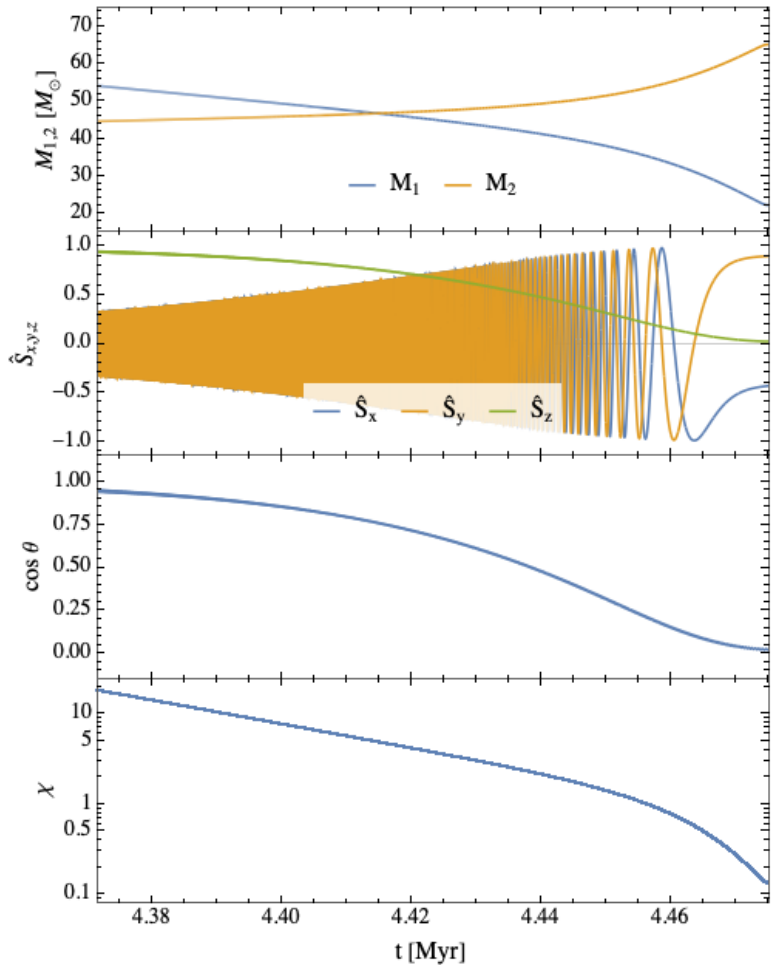

Figure 4.5. Spin-evolution in one exemplary mass transferring stellar binary. At $t = 0$ (ZAMS), the stellar masses, eccentricity, and orbital period were set to $m_1 = 55\,\mathrm{M}_\odot$, $m_2 = 45\,\mathrm{M}_\odot$, $e = 0.1$, and $T = 10^2$ days, respectively. This binary undergoes a mass transfer phase at about 4.37 to 4.48 Myr which is considered here. The tidal lag time was set to $\tau = 10^{-1}$ s. From top to bottom, the first panel shows the evolution of the stellar masses, the second panel the donor spin components in some inertial frame, the third panel the cosine of the tilt angle, and the fourth panel its dimensionless spin magnitude $\chi = cS/Gm_1^2$. The inertial frame is defined such that it coincides with $\mathfrak{F}$ at the onset of mass transfer (i.e., the z-axis is pointing along $\hat{\boldsymbol{h}}$).

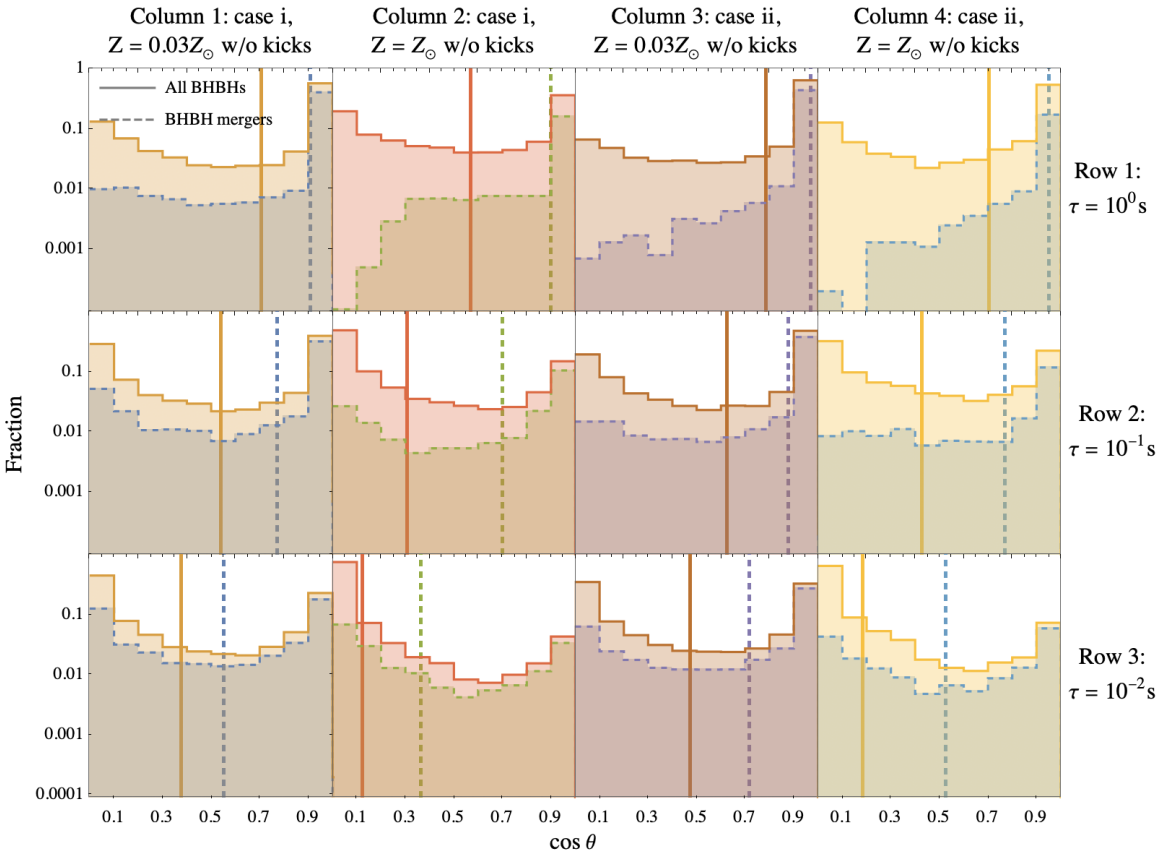

Figure 4.6. Tilt angle distributions of the primaries once they stopped donating mass. Initially, the tilt angles were uniformly distributed in the rightmost bins ($\cos\theta = 0.9 - 1.0$). Each solid histograms includes 10^4 systems in which the primary fills its Roche-lobe first and that eventually end up as BBH systems. The dashed histograms constitute the subset of systems that merge within $t_{\rm coal} < 10\,$Gyr. Vertical lines indicate the means of each distribution. From the top to the lowest panel row, the strength of the tides were decreased by lowering the lag time τ. The different panel columns incorporate low and high metallicities and mass transfer modelled with case (i) and (ii) (e.g., Section 4.3).

not very sensitive to the precise numerical value. The time to coalescence can be estimated by Eq. (1.66) which we evaluate once both BHs are formed. In Fig. 4.6, these subsets are indicated by dashed lines. We also display the means of the distributions by means of the vertical dotted lines. For $\tau = 10^0$ s, the number of flipped spins is insignificantly low and the means are close to or within the initial value range $[0.9, 1.0)$. Hence, it can be concluded that mass transfer would be irrelevant for the spin dynamics in that case. Only if shorter lag times are considered the number of flipped spins can become comparable to that of aligned spins. In terms of the means we achieve about 0.6 to 0.9 and 0.3 to 0.7 for $\tau = 10^{-1}$ s and $\tau = 10^{-2}$ s, respectively. The fact that flips are less prevalent in the merger subsets is due to the shorter binary separation which increases the strength of tides (see Section 4.4).

Once the primary stops transferring mass to the secondary, there are four successive evolutionary stages in which its spin direction relative to $\hat{\boldsymbol{h}}$ (or that of its BH remnant) could, in principle, change again (e.g., Fig. 1 of Belczynski et al. (2016a)). Firstly, during the rest of its lifetime the primary star is still subject to tidal forces by its companion. However, the tidal friction timescales of systems whose primaries flipped during mass transfer is typically much larger than the remaining lifetime which is about $\mathcal{O}(0.1)$ Myr. Hence, we do not expect a significant change of the spin distributions in Fig. 4.6. Secondly, when the primary forms a BH in a SN the latter can receive a kick due to asymmetric mass loss that tilts the orbital angular momentum inducing a misalignment with respect to the spin directions (Kalogera, 2000; Gerosa et al., 2013). We investigate this possibility below. Thirdly, if the secondary star fills its Roche-lobe it transfers mass towards the first-born BH that has been formed out of the primary. The timescale at which the BH spin would align with the angular momentum of an accretion disk has been derived by Natarajan & Pringle (1998) and is given by

$$t_{\mathsf{align}} \simeq 0.56\,\mathsf{Myr}\,\chi^{11/16}\left(\frac{\alpha}{0.03}\right)^{13/8}\left(\frac{L}{0.1L_{\mathsf{E}}}\right)^{-7/8}\left(\frac{m_1}{10^8\,\mathrm{M}_\odot}\right)^{-1/16}\left(\frac{\epsilon}{0.3}\right)^{7/8}, \tag{4.56}$$

where α the dimensionless viscosity parameter of the accretion disk (Shakura & Sunyaev, 1973), L the energy accretion rate onto the BH, $L_{\mathsf{E}} = 1.4\times10^{38} m_1\,\mathrm{M}_\odot^{-1}\,\mathsf{ergs\,s}^{-1}$ the Eddington luminosity, and $\epsilon = L/\dot{m}_1 c^2$ the efficiency of the accretion process. As an order-of-magnitude estimate we would get $t_{\mathsf{align}} \simeq 1.4\,\mathsf{Myr}$ for $\chi = 1$, $\alpha = 0.03$, $L = 0.1L_{\mathsf{E}}$, $m_1 = 50\,\mathrm{M}_\odot$, and $\epsilon = 0.3$. Again, this is typically much longer than the duration of the second mass transfer phase. Fourthly, if this mass transfer is succeeded by a CE phase in which the expanding envelope of the secondary engulfs the primary BH the latter is subject to dynamical friction forces promoting a quick inspiral. Recent hydrodynamic simulations show that whilst inspiralling the mass and dimensionless spin parameter of the BH do increase but not larger than 1 to 2 per cent and 0.05, respectively (De et al., 2020).

Based on this discussion, we have reason to believe that, unless natal kicks are considered, the tilt angle of the primary spin and the orbital angular momentum does not significantly change between the end of the first mass transfer phase and the formation of the BH binary. Fig. 4.6 would hence reflect the spin distributions of the first-born BH in the BBH unless the effect of natal kicks are considered.

In Fig. 4.7, we take the latter effect into account by implementing the tilts of $\hat{\boldsymbol{h}}$ due to the natal kicks at the first and second SNe. That is, for each SN we adopt the widely held assumption that the magnitude of the natal kick velocity v_{kick} of the BH follows the one observed for NSs scaled down by some fallback-fraction f_{fb} (Banerjee et al., 2020),

$$v_{\mathsf{kick}} = v_{\mathsf{kick,NS}}(1 - f_{\mathsf{fb}}), \tag{4.57}$$

where $0 \leq f_{\mathsf{fb}} \leq 1$ and $v_{\mathsf{kick,NS}}$ is drawn from a Maxwellian distribution with a velocity dispersion $\sigma_{\mathsf{kick,NS}} = 265\,\mathrm{km\,s^{-1}}$ (Hobbs et al., 2005). Assuming the SN explosion occurs instantaneously, Eq. (4.57) can be used to derive the angle ν between the new and old angular momentum before and after the SN, respectively (see appendix of Hurley et al., 2002). Thus, the new tilt angle θ_{new} of the primary's spin can be computed as

$$\cos\theta_{\mathsf{new}} = \cos\phi \sin\theta_{\mathsf{old}} \sin\nu + \cos\theta_{\mathsf{old}} \cos\nu, \tag{4.58}$$

where θ_{old} describes the tilt angle before the SN and ϕ is an angle drawn from a uniform distribution between 0 and 2π reflecting an isotropic kick distribution (e.g., Gerosa et al., 2013; Rodriguez et al., 2016b). For producing Fig. 4.7, this method has been successively applied for each SN. For the merging BBHs the effect of kicks alone can be seen from the dot-dashed histograms for which we skipped the spin dynamics given by Eq. (4.38). Instead, we directly applied the kick prescription to the initial tilt angles in the range $[0.9, 1.0)$ (see above). The resulting distributions have pronounced peaks at $\cos\theta = 1$ with an exponential tail ranging down to $\cos\theta = -1$. The effect of the tails is to broaden the distributions with the whole spin dynamics included (solid and dashed histograms) yielding a small fraction of donor spins that have a $\cos\theta$ below zero.

Furthermore, we investigate whether the distributions presented in Figures 4.6 and 4.7 are correlated with the chirp mass $\mathcal{M}_c = (m_1 m_2)^{3/5}/(m_1 + m_2)^{1/5}$ which the LIGO-Virgo detectors are most sensitive to. As a result, we find that $\cos\theta$ does not depend on $\mathcal{M}_c$. Finally, we also investigate the possibility that at the onset of mass transfer the spin direction is isotropically distributed. That is, we draw the initial value of $\cos\theta_0$ from a uniform distribution in the interval $(-1, 1)$. As one would expect, we find that the resulting distributions are shifted towards zero by up to ~ 0.2.

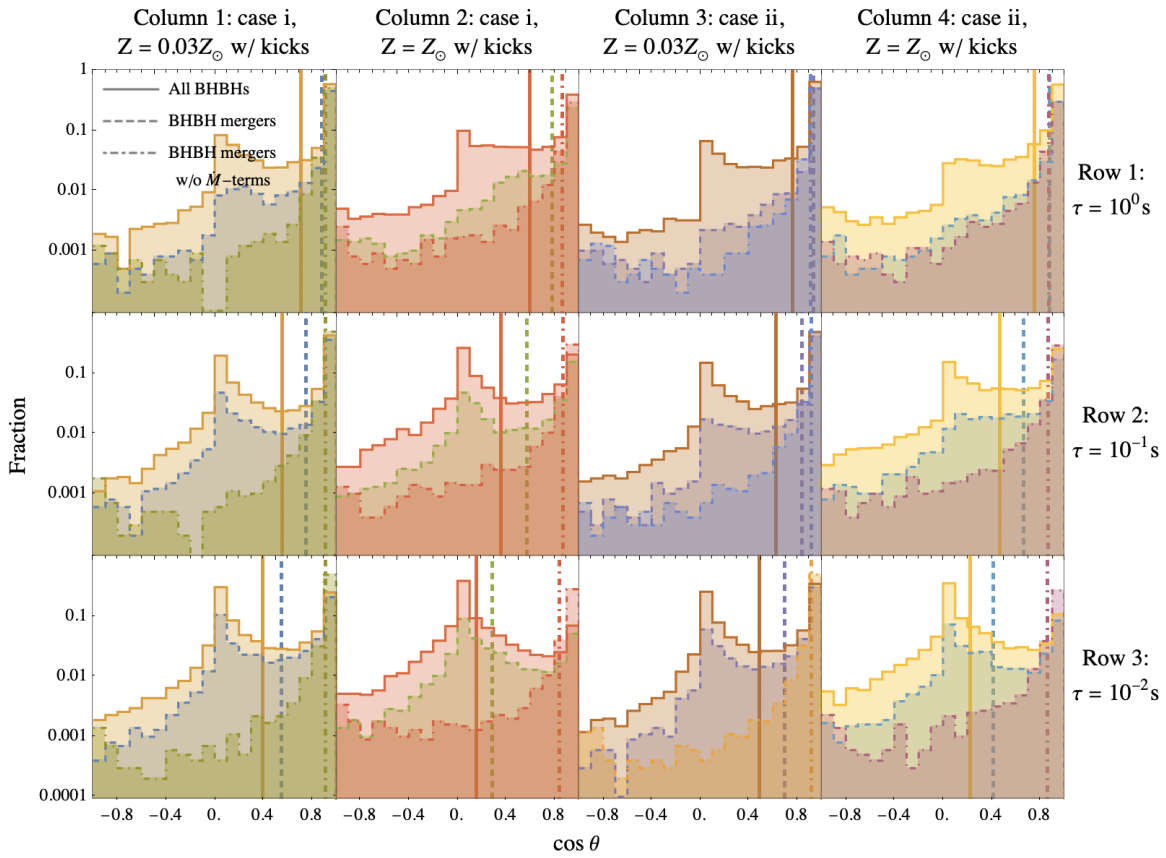

Figure 4.7. Same as Fig. 4.6 but natal kicks are included. Additionally, the dot-dashed histograms show the tilt angle distribution of the merging systems ($t_{\rm coal} < 10\,$Gyr; dashed histograms) if the spin directions were only affected by the natal kicks and not by the spin dynamics given by Eq. (4.38).

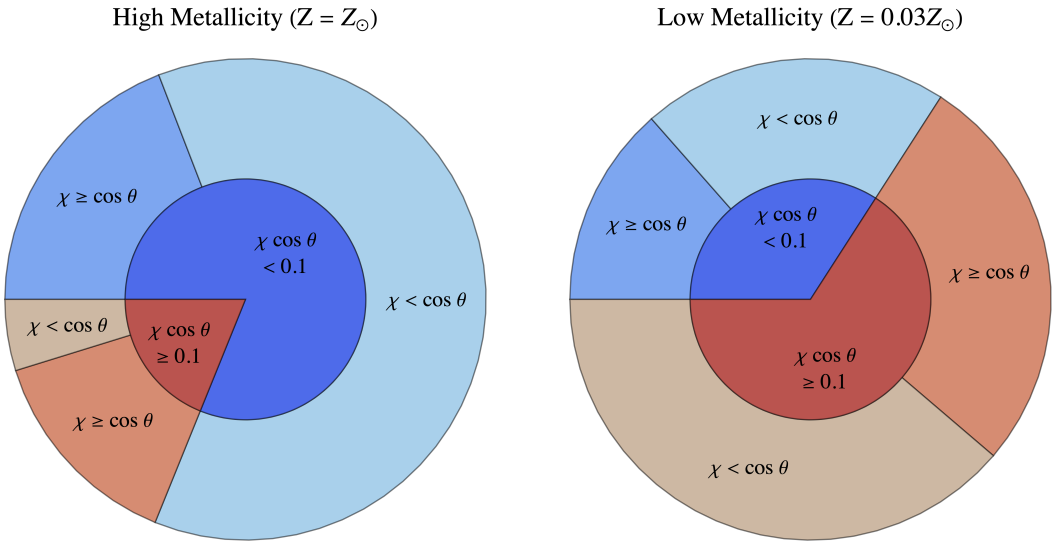

Figure 4.8. Spin projections onto the orbital axis of 10^4 binaries that form merging BBHs. The two panels differ from each other by their metallicities. In both cases, mass transfer and tides are modelled with case (i) and a lag time $\tau = 10^{-1}$ s.

Finally, we study the contributions of the first-born BHs to χ_{eff} (cf. Eq. (4.1)) at its formation. For this purpose, we plot in Fig. 4.8 the distribution of the primary spin projection $\chi \cos\theta$ at high (left) and low metallicity (right panel) for 10^4 binaries that form merging BBHs. In both cases, mass transfer and tides are modelled with case (i) and a lag time $\tau = 10^{-1}$ s. The effect of kicks is not taken into account. The inner pies of the panels differentiate the population between primaries whose contribution we consider to be insignificant ($\chi \cos\theta < 0.1$) and significant ($\chi \cos\theta \geq 0.1$). We stress that this differentiation is somewhat arbitrary, also we do not take the mass-weight into account, but it nevertheless gives a rough estimate of the primaries' spin contribution. We see a clear difference between the two metallicities. Whereas at high metallicity $\chi \cos\theta$ of about 80 per cent is insignificant, this is only true for 30 per cent at low metallicity. This shows that one must not neglect the spin of the first-born BH if formed at low metallicity. In particular, this result would also hold for stronger tides, i.e., larger values for τ, because in that case $\cos\theta$ would tend to increase towards 1, i.e., align with the orbital axis. For the systems with insignificant contribution we can ask whether this is due to a small magnitude χ or due to a flip, i.e., a small $\cos\theta$. At both metallicities, the fraction with $\chi \geq \cos\theta$ is non-negligible. This is true for about 20 per cent and even one half at high and low metallicity, respectively. This suggests that the spin orientation has to be taken into account when studying the spin-contribution of the first-born BH to χ_{eff} at formation. In Section 4.5, we have shown that the spin magnitude and its subsequent evolution depend on the spin value at $t = 0$. Evidently, the spin orientation becomes irrelevant if we had overestimated the initial spin magnitude, i.e., if χ were actually smaller than

we have assumed. Lastly, we note that during inspiral, the orbit-average of χ_{eff} remains constant at 2PN order whereas the relative contributions of the primary and secondary BH change due to relativistic effects which become more important as the orbit gets tighter (Damour, 2001; Racine, 2008).

Chapter 5

Conclusion

In this work, we investigated the long-term evolution of hierarchical massive stellar triples. For this purpose, we presented a novel Triple Stellar Evolution Code `TSE` that simultaneously takes into account the secular three-body interaction and the evolution of the stars. We used this code to follow the evolution of a population of isolated triples from their ZAMS until the formation of compact objects. We investigated and quantified the frequency of various evolutionary outcomes of massive triple evolution, and discussed the implications for the formation compact object triples that could be driven to a merger via the LK mechanism (Chapter 2).

As a result from the stellar triple evolution, we have seen that the inner binary stars frequently merge before they could form any compact object. Therefore, we studied in detail the evolution of the stellar post-merger binaries composed of the merger product star and the tertiary companion. We found that post-merger binaries originating from compact stellar triples with outer semi-major axes $a_{\rm out,0} \lesssim 10^1 - 10^2\,{\rm AU}$ provide a new way to form BBH mergers in the galactic field. By means of a population synthesis, we estimated their contribution to the total BBH merger rate to be $\mathcal{R}(z=0) = 0.3 - 25.2\,{\rm Gpc^{-3}\,yr^{-1}}$. Merging BBHs that form from stellar post-merger binaries have exceptionally low mass ratios. We identified a critical mass ratio $q \simeq 0.5$ below which they dominate the total BBH merger rate in the field. We showed that after including their additional contribution, the mass ratio distribution of BBH mergers in the galactic field scenario is in better agreement with that inferred from GW detections (Chapter 3).

Lastly, we examined the evolution of the rotational angular momentum (spin) vector of a massive (donor) star which transfers to a binary companion (accretor). Assuming that the donor star loses mass along the instantaneous interstellar axis, we derived the orbit-averaged equations of motion describing the evolution of the donor spin vector which accompanies the transfer of mass. We considered: (i) a model in which the mass transfer rate is constant within each orbit and (ii) a phase-dependent rate in which all mass per orbit is lost at periapsis. In both cases, we

found that the ejection of $\gtrsim 30$ per cent of the donor's initial mass causes its spin to nearly flip onto the orbital plane of the binary, independently of the initial spin-orbit alignment. Moreover, we showed that the spin flip due to mass transfer can easily dominate over tidal synchronisation in any giant stars and MS stars with masses ~ 1.5 to $5\,\mathrm{M}_\odot$. Finally, the general equations of motion, including tides, were used to evolve a realistic population of massive binary stars leading to the formation of BBHs. Assuming that the stellar core and envelope are fully coupled, the resulting tilt of the first-born BH reduced its spin projection onto the orbit normal by a factor $\sim \mathcal{O}(0.1)$. This result supports previous studies in favour of an insignificant contribution to the effective spin projection, χ_{eff}, in BBHs formed from the evolution of field binaries (Chapter 4).

In the following, we discuss for each chapter our findings in more detail.

5.1 Evolution of massive stellar triples

Simulating the evolution of a population of massive stellar triples, we found a well-defined mapping between the initial properties of the triples and the probability to achieve a certain evolutionary outcome (Fig. 2.3). Wide systems are vulnerable to disruption by a SN kick. In our models with non-zero kicks we found that in more than $50\,\%$ of triples with an outer semi-major axis $a_{\mathrm{out}} \gtrsim 400\,\mathrm{AU}$ the inner binary is disrupted during a SN. At smaller values of a_{out}, most systems either experience a merger in the inner binary before a DCO is formed, become dynamically unstable (for $q_{\mathrm{out}} \lesssim 0.8$), or have tertiary companion that fills its Roche-lobe (for $q_{\mathrm{out}} \gtrsim 0.8$). Stellar mergers can give rise to observable signatures such as red novae (Pastorello et al., 2019) and hydrogen-rich (Vigna-Gómez et al., 2019) or strongly magnetised remnants (Schneider et al., 2019). Dynamically unstable systems enter a regime in which our secular approach breaks down and a chaotic evolution takes place leading to the ejection of one component or the merger of two (Mardling & Aarseth, 2001; Petrovich, 2015; Toonen et al., 2022). The subsequent evolution of systems with a Roche-lobe filling tertiary companion is not well understood. Compared to RLO in isolated binaries, previous work on tertiary RLO is inherently more complex due to modulations caused by the periodic motion of the inner binary and its non-trivial response to mass accretion (Di Stefano, 2020a,b; Glanz & Perets, 2021; Hamers et al., 2022).

Our method provides a self-consistent way to generate compact object triples (and DCOs with a low mass star companion) which can be used to study the triple channel for GW sources (Silsbee & Tremaine, 2017; Antonini et al., 2018, 2017; Rodriguez & Antonini, 2018). Table 2.2 gives the fraction of triple evolutionary outcomes for our different models, showing that at most a few percent of systems evolve to become stable triples with an inner DCO binary – the exact fraction depends on metallicity and the adopted natal kick prescription. The orbital properties

of all systems that form a DCO binary are shown in Figures 2.4 and 2.5. At low metallicity, more than half of the surviving triples are LK-possible in the sense that LK oscillations are not quenched by the Schwarzschild precession of the inner binary orbit. At solar metallicity, this is the case for almost all triples.

In any of our models, the vast majority of surviving triples harbour an inner BBH (see Table 2.3). Triples with a NS component in the inner binary are very rare. In models with non-zero natal kicks their number is typically two orders of magnitude smaller than triples with BBHs. Unless `no kicks` are assumed, no surviving triple harbouring a BNS has been found in our population. We conclude that it is unlikely that BNSs can be driven to a merger via the LK mechanism in triples.

Population synthesis studies of massive stellar binaries do not follow the interaction of the binary with outer companions. However, treating the inner binary as being isolated poses a risk to miss out the perturbative effect a tertiary companion on the evolution of the inner binary. Our study shows that inner binaries with initial periapses $10^3 \lesssim a_{\rm in}(1-e_{\rm in})/{\rm R}_\odot \lesssim 10^5$ are driven to a RLO due to the presence of the tertiary companions (Fig. 2.8). The latter can effectively reduce the minimum periapses so that the inner binary stars have to be less expanded in order to fill their Roche-lobe. This gives rise to mass transfer episodes on very eccentric orbits. Below $\sim 10^3\,{\rm R}_\odot$ the inner binary stars undergo RLOs even if they were in isolation. Nonetheless, the tertiary companions can cause them to occur on more eccentric orbits provided that $a_{\rm out}/a_{\rm in} \lesssim 10^2$ initially.

By comparing the triple population to isolated binary population models, we showed that the interaction with the tertiary companion does not significantly change the resulting orbital distributions of the surviving (inner) DCOs. Moreover, in the triple population the fraction of systems in which the inner binaries evolve without undergoing a mass transfer episode is only decreased by not more than $3\,\%$ compared to the binary population models (Figures 2.9 – 2.11). However, compact triples with initial inner periods $P_{\rm in} \lesssim 10^2\,{\rm days}$ are prone to become dynamically unstable or to have a Roche-lobe filling tertiary companion. We found this to be the case in ~ 7 – $14\,\%$ and $\sim 5\,\%$ of the systems, respectively (Table 2.2). For these systems the evolution of the inner binary is expected to be significantly affected by the triple interaction.

5.2 Black hole mergers from stellar mergers in triples

Motivated by the large fraction of stellar mergers that take place in the inner binaries, we considered the subsequent evolution of the merger product stars and the tertiary companions to merging BBHs. As a consequence of the stellar mergers, the number of heavy primary stars in the post-merger binary gets inflated which which generally leads to heavier BHs. Consequently,

more low mass ratio BBH mergers are produced in the triple population. Additionally, rejuvenation of the merger product star can make it the acceptor during a mass transfer episode with the tertiary companion, which further increases the imbalance of the BH masses. Thus, exceptional BBH merger events like GW190412 with reported component masses $m_1 = 30.1^{+4.6}_{-5.3}\,\mathrm{M}_\odot$ and $m_2 = 8.3^{+1.6}_{-0.9}\,\mathrm{M}_\odot$ (Abbott et al., 2020a) could be a possible outcome of the outer binary channel.

Meanwhile, the marginalised mass distribution of BBH mergers is not significantly altered. We find the chirp mass distribution everywhere to be dominated by the high mass ratio BBH mergers formed via the inner binary channel (see Fig. A.1 in Appendix A.4). Moreover, we do not expect the outer binary channel to leave a distinctive imprint on the eccentricity distribution. Since a CE evolution precedes most BBH mergers in both channels, we expect high eccentricities to be suppressed. A thorough investigation of the spins of merging BHs is beyond the scope of this work. Yet, the outer binary channel might explain the observed correlation between low mass ratios and higher effective spin parameters (Packet, 1981; The LIGO Scientific Collaboration et al., 2021). It is expected that even little mass accretion efficiently spins up the post-merger star during the stable mass transfer episode (Renzo & Götberg, 2021). Previous magneto-hydrodynamical simulations suggest that the post-merger star is strongly magnetised (Schneider et al., 2019, 2020). A strong core-envelope coupling by the magnetic fields would ensure that the core also spins up due to the mass transfer phase (Fuller & Ma, 2019). As a result, low mass ratio BBH mergers with highly spinning primary BHs may be formed.

5.3 Flipping spins in mass transferring binaries

Considering the spin dynamics in mass transferring binaries, we showed that the mass loss from the donor is accompanied with an anisotropic spin-loss that causes the spin magnitude to decrease and its direction to flip onto the orbital plane, i.e., to form a tilt angle of $\theta = \pi/2$ w.r.t. the orbital angular momentum. Generally, this spin dynamics were described by Eq. (4.12). Provided that all parts of the star are sufficiently coupled by efficient angular momentum transport it follows that the solution to this equation also determines the spin direction of all individual parts of the star.

We derived the orbit averaged equations of motion describing the evolution of the donor spin, assuming either a constant mass transfer rate per orbit, Eqs. (4.19)–(4.21), or a delta-function mass transfer at periapsis, Eqs. (4.27)–(4.29). Whilst the former case holds for approximately circular orbits the latter may be a valid model for highly eccentric systems. By considering these two extreme cases we expect that, in reality, the mass transfer rate on moderately eccentric orbits lies somewhere in the intermediate range. As a key result of both cases, we found that for total

relative mass losses of about $\mathcal{O}(0.1)$ the spin flip is highly efficient unless it starts perfectly or nearly (anti-)aligned with the orbital angular momentum (see Section 4.3 and Figures 4.1 and 4.2). Meanwhile, the relative loss in spin magnitude is about several orders of magnitude. As a corollary, we found that both effects are independent of the actual duration of mass transfer but only depend on the total mass that is lost.

We compared the timescale for spin misalignment due to mass loss to the synchronisation timescale due to tidal torques. Whether the former effect is faster than tides depends strongly on the stellar separation at the onset of mass transfer, with smaller separations favoring tides. We found, however, that the effect of mass loss can dominate in both MS and giant stars and for a wide range of donor masses. Hence, the commonly adopted assumption that tides will very rapidly erase any spin-orbit misalignment in mass transferring binaries is not fully justified.

In reality, a donor might actually have expanded so much that it loses mass through the outer Lagrangian point too, i.e., through the second (L_2) or third (L_3) depending on whether it is the less or more massive binary member, respectively. By simulating the response of giant donors to mass loss, Pavlovskii & Ivanova (2015) showed that there exists a critical mass ratio below which its mass is transferred solely and stably through L_1. For example, they found that a $30\,\mathrm{M}_\odot$ donor undergoes L_2/L_3 overflow only if it is about two to three times as massive as its companion. If we replace $\boldsymbol{R}$ in Eq. (4.12) by some vector pointing to L_2/L_3, i.e., along $-\hat{\boldsymbol{d}}$, we see that $\dot{\boldsymbol{S}}$ remains invariant up to some positive factor accounting for the larger expansion of the star. Hence, we expect L_2/L_3 overflow to promote a spin flip as well. However, L_2/L_3 overflow of the donor is typically very short so that the stream of matter is negligible compared to that through L_1 (Pavlovskii et al., 2017; Pavlovskii & Ivanova, 2015).

As a potential application, we investigated the spin evolution of isolated stellar binaries which form a BBH (see Section 4.5). A fraction of these BBHs lead to a merger detectable by LIGO-Virgo though their emission of GWs. These binaries have to move on a close orbit making them prone to undergo a phase of stable mass transfer in which the stellar progenitor of the first-born BH typically loses up to about half of its mass to its companion. By means of a population synthesis, we followed the spin evolution of the primary stars in a large number of BBH forming binaries. To this end, we let our spin dynamics [Eq. (4.12)] compete with external torques emerging from the quadrupolar distortion of the donor and the tidal interaction between the binary members whose strength was parametrised by the constant lag times $\tau = 10^0$, 10^{-1}, and $10^{-2}\,\mathrm{s}$ [Eq. (4.50)]. The stellar physics was simulated at low ($Z = 0.03\,\mathrm{Z}_\odot$) as well as high metallicity ($Z = \mathrm{Z}_\odot$). We found that the resulting tilt angle distribution is strongly bimodal with most spins ending up either aligned with or perpendicular to the orbital angular momentum. The ratio of aligned and flipped systems, however, depends on the metallicity, the tidal lag time, and whether the BBHs merge within $10\,\mathrm{Gyr}$ or not. For instance, going from the long to the short lag time we found that for

mergers with low (high) metallicity the $\cos\theta$-distributions' means decrease from ~ 0.9 (0.8 to 0.9) to ~ 0.5 to 0.7 (~ 0.3 to 0.5), i.e., from fair alignment to a mature flip. The values were even smaller by $\sim 0.1 - 0.2$ when we considered all systems that form BBHs. Finally, we have argued that natal kicks are the only effect that could significantly change again the tilt angle between the end of the mass transfer phase and the BBH formation. Whilst the bulk of primary spins remains largely unaffected, natal kicks introduce an exponentially suppressed fraction of primaries with tilt angles towards anti-alignment ($-1 < \cos\theta < 0$). Overall, we found that at formation the first-born BH's contribution to χ_{eff} [see Eq. (4.1)] of a BBH which will merge through the channel considered is typically negligible not only due to its depleted spin magnitude but also due to its misalignment $\cos\theta \sim \mathcal{O}(0.1)$ w.r.t. the orbital axis.

Appendix A

Appendix

A.1 Hut's polynomials

$$f_1(e_{\rm in}) = 1 + \frac{31}{2}e_{\rm in}^2 + \frac{255}{8}e_{\rm in}^4 + \frac{185}{16}e_{\rm in}^6 + \frac{25}{64}e_{\rm in}^8, \tag{A.1}$$

$$f_2(e_{\rm in}) = 1 + \frac{15}{2}e_{\rm in}^2 + \frac{45}{8}e_{\rm in}^4 + \frac{5}{16}e_{\rm in}^6, \tag{A.2}$$

$$f_3(e_{\rm in}) = 1 + \frac{15}{4}e_{\rm in}^2 + \frac{15}{8}e_{\rm in}^4 + \frac{5}{64}e_{\rm in}^6, \tag{A.3}$$

$$f_4(e_{\rm in}) = 1 + \frac{3}{2}e_{\rm in}^2 + \frac{1}{8}e_{\rm in}^4, \tag{A.4}$$

$$f_5(e_{\rm in}) = 1 + 3e_{\rm in}^2 + \frac{3}{8}e_{\rm in}^4. \tag{A.5}$$

A.2 Exemplary triples

The initial parameters of the three triples shown in Figure 2.1 are as following.

The masses of the system in the left panel are $m_1 = 98.4\,\mathrm{M}_\odot$, $m_2 = 32.6\,\mathrm{M}_\odot$, and $m_3 = 44.1\,\mathrm{M}_\odot$. The eccentricities and semi-major axes are $e_{\rm in} = 0.89$, $e_{\rm out} = 0.48$, $a_{\rm in} = 30.7\,\mathrm{AU}$, and $a_{\rm out} = 915.2\,\mathrm{AU}$, respectively. The relative inclination reads $\cos i_{\rm tot} = 0.26$ while the arguments of periapses are $\sin g_{\rm in} = 0.11$ and $\sin g_{\rm out} = 0.87$.

For the systems in the middle panel we have $m_1 = 60.8\,\mathrm{M}_\odot$, $m_2 = 44.0\,\mathrm{M}_\odot$, $m_3 = 20.2\,\mathrm{M}_\odot$, $e_{\rm in} = 0.99$, $e_{\rm out} = 0.68$, $a_{\rm in} = 74.9\,\mathrm{AU}$, $a_{\rm out} = 1125.3\,\mathrm{AU}$, $\cos i_{\rm tot} = -0.83$, $\sin g_{\rm in} = -0.06$, and $\sin g_{\rm out} = 0.72$.

Finally, the parameters of the system in the right panel are $m_1 = 49.6\,\mathrm{M}_\odot$, $m_2 = 33.0\,\mathrm{M}_\odot$, $m_3 = 40.0\,\mathrm{M}_\odot$, $e_\mathrm{in} = 0.83$, $e_\mathrm{out} = 0.38$, $a_\mathrm{in} = 0.8\,\mathrm{AU}$, $a_\mathrm{out} = 17.2\,\mathrm{AU}$, $\cos i_\mathrm{tot} = 0.77$, $\sin g_\mathrm{in} = 0.27$, and $\sin g_\mathrm{out} = 0.82$.

A.3 BBH merger rate density

At cosmological redshift z, the merger rate of BBHs from a given stellar population can be calculated by a convolution of the delay time distribution and the cosmic star formation history (Safarzadeh et al., 2020)

$$\mathcal{R}_\mathrm{BBH}(z) = \int_{z_b=10}^{z_b=z} \int_{Z=10^{-4}}^{Z=0.03} \mathrm{d}z_b\,\mathrm{d}Z\,\frac{\mathrm{d}t}{\mathrm{d}z}(z_b)\mathcal{F}_\mathrm{Z}(t-t_b)\mathcal{R}_\mathrm{SFR}(Z,z_b). \tag{A.6}$$

We adopt standard ΛCDM cosmology in which $\mathrm{d}t/\mathrm{d}z = -\left[(1+z)E(z)H_0\right]^{-1}$ and $E(z) = \left[\Omega_{M,0}(1+z)^3 + \Omega_{K,0}(1+z)^2 + \Omega_{\Lambda,0}\right]^{1/2}$ with $1/H_0 = 14\,\mathrm{Gyr}$, $\Omega_{M,0} = 0.3$, $\Omega_{K,0} = 0$, and $\Omega_{\Lambda,0} = 0.7$ (Planck Collaboration et al., 2016).

The function $\mathcal{F}_\mathrm{Z}(t-t_b)$ results from the simulation of the stellar populations and describes the fraction of systems in a metallicity bin $[Z, Z+\mathrm{d}Z)$ which lead to BBH mergers with a delay time $t-t_b$ per $\mathrm{d}t$. The second term in the integration, $\mathcal{R}_\mathrm{SFR}(Z,z_b)$, is the cosmic star formation rate which we write as

$$\mathcal{R}_\mathrm{SFR}(Z,z_b)\mathrm{d}Z = \kappa\psi(z_b)p(Z,z_b)\mathrm{d}Z, \tag{A.7}$$

using the data fit from Madau & Fragos (2017)

$$\psi(z_b) = 0.01\frac{(1+z_b)^{2.6}}{1+\left[(1+z_b)/3.2\right]^{6.2}}\,\mathrm{M}_\odot\,\mathrm{Mpc}^{-3}\,\mathrm{yr}^{-1}, \tag{A.8}$$

and the chemical enrichment model where Z at redshift z_b follows a log-normal distribution

$$p(Z,z_b) = \frac{\log(e)}{\sqrt{2\pi\sigma_Z^2}Z}\exp\Big\{-\frac{\left[\log(Z/\mathrm{Z}_\odot)-\mu(z_b)\right]^2}{2\sigma_Z^2}\Big\}, \tag{A.9}$$

with mean metallicity $\mu(z_b) = 0.153 - 0.074z_b^{1.34}$ (Madau & Fragos, 2017). and standard deviation $\sigma_Z = 0.25$ (Dvorkin et al., 2015). Different choices for the value σ_Z For ψ we assume a log-normal distribution with a standard deviation of $\sigma_\psi = 0.5$.

Eq. (A.8) describes the rate at which mass of all stars with mass 0.1 – $100\,\mathrm{M}_\odot$ is formed, regardless whether they are multiplicity systems or not. Since we are only simulating massive triples and binaries with $m_{1(2)} \geq 5\,\mathrm{M}_\odot$ and $m_3 \geq 8\,\mathrm{M}_\odot$ (see Section 3.1.2) the constant κ is

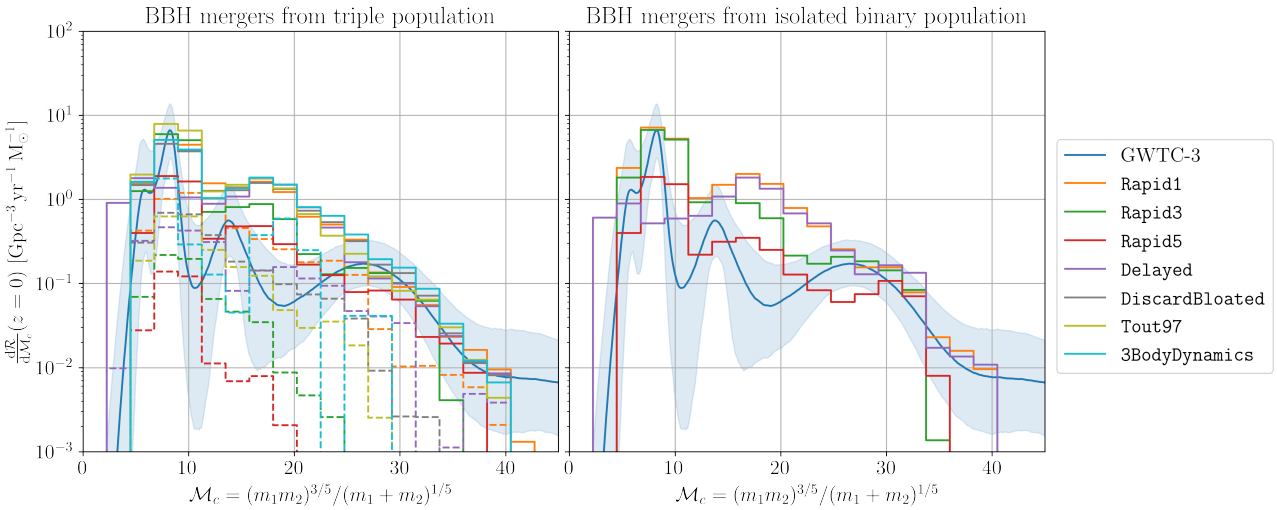

Figure A.1. Chirp mass distribution of BBH mergers in the local Universe ($z = 0$). As in Figure 3.5 dashed lines highlight the contribution from the outer binary channel.

introduced to convert ψ into a formation rate of progenitor systems with the assumed properties. To calculate κ we set up an entire stellar population of any mass assuming the same parameter distribution as in Section 3.1.2 and multiplicity fractions as a function of the primary spectral type as reported by Moe & Di Stefano (2017). Here, we only consider singles, binaries, and triples (neglecting the effect of quadruples and higher-order systems) and assume that any primary star with $m_1 \geq 20\,\mathrm{M}_\odot$ is in a triple. We then calculate κ and the resulting BBH merger rate for each spectral type individually.

In practice, the uncertainty of $\mathcal{R}_{\mathrm{BBH}}(z)$ is estimated by Monte-Carlo sampling of Eq. (A.6).

A.4 Chirp mass distribution

In Figure A.1, we show the differential merger rate per chirp mass $\mathcal{M}_c = (m_1 m_2)^{3/5}/(m_1 + m_2)^{1/5}$ which determines the gravitational waveform at leading order. On coarse-grained scales, we find agreement of our models with the "flexible mixture model" (GWTC-3) up to $\mathcal{M}_c \lesssim 40\,\mathrm{M}_\odot$, but note that neither the isolated nor the triple population could reproduce substructure of the mass distribution that were discovered in the third observing run of the The LIGO Scientific Collaboration et al. (2021).

A.5 Tides and Rotation

The perturbations of the equations of motion (4.45) – (4.48) can be expressed in terms of five functions X, Y, Z, V, and W (Eggleton & Kiseleva-Eggleton, 2001; Fabrycky & Tremaine, 2007):

$$X = -\frac{M_2 k_{\rm A} R^5}{\mu n a^5} \frac{(\boldsymbol{\omega}\cdot\hat{\boldsymbol{h}})(\boldsymbol{\omega}\cdot\hat{\boldsymbol{e}})}{j^4} - \frac{\boldsymbol{\omega}\cdot\hat{\boldsymbol{v}}}{2nt_{\rm F}} \frac{1+(9/2)e^2+(5/8)e^4}{j^{10}}, \tag{A.10}$$

$$Y = -\frac{M_2 k_{\rm A} R^5}{\mu n a^5} \frac{(\boldsymbol{\omega}\cdot\hat{\boldsymbol{h}})(\boldsymbol{\omega}\cdot\hat{\boldsymbol{v}})}{j^4} + \frac{\boldsymbol{\omega}\cdot\hat{\boldsymbol{v}}}{2nt_{\rm F}} \frac{1+(3/2)e^2+(1/8)e^4}{j^{10}}, \tag{A.11}$$

$$Z = \frac{M_2 k_{\rm A} R^5}{\mu n a^5} \left[\frac{2(\boldsymbol{\omega}\cdot\hat{\boldsymbol{h}})^2 - (\boldsymbol{\omega}\cdot\hat{\boldsymbol{e}})^2 - (\boldsymbol{\omega}\cdot\hat{\boldsymbol{v}})^2}{2j^4} + \frac{15GM_2}{a^3} \frac{1+(3/2)e^2+(1/8)e^4}{j^{10}} \right], \tag{A.12}$$

$$V = \frac{9}{t_{\rm F}} \left[\frac{1+(15/4)e^2+(15/8)e^4+(5/64)e^6}{j^{13}} - \frac{11\boldsymbol{\omega}_1\cdot\hat{\boldsymbol{h}}}{18n} \frac{1+(3/2)e^2+(1/8)e^4}{j^{10}} \right], \tag{A.13}$$

$$W = \frac{1}{t_{\rm F}} \left[\frac{1+(15/2)e^2+(45/8)e^4+(5/16)e^6}{j^{13}} - \frac{\boldsymbol{\omega}_1\cdot\hat{\boldsymbol{h}}}{n} \frac{1+3e^2+(3/8)e^4}{j^{10}} \right], \tag{A.14}$$

where the tidal friction timescale $t_{\rm F}$ depends on the dissipative mechanism at work as described in Section 4.4.

Bibliography

Abbott B. P., et al., 2016, *Phys. Rev. Lett.*, 116, 061102

Abbott B. P., et al., 2017, *Phys. Rev. Lett.*, 119, 161101

Abbott B. P., et al., 2019, Physical Review X, 9, 031040

Abbott R., et al., 2020a, *Phys. Rev. D*, 102, 043015

Abbott R., et al., 2020b, *Phys. Rev. Lett.*, 125, 101102

Abbott R., et al., 2021a, Physical Review X, 11, 021053

Abbott R., et al., 2021b, *ApJ*, 913, L7

Albrecht S., Reffert S., Snellen I. A. G., Winn J. N., 2009, *Nature*, 461, 373

Alexander M. E., 1973, *Astrophys. Space Science*, 23, 459

Anderson K. R., Storch N. I., Lai D., 2016, *MNRAS*, 456, 3671

Anderson K. R., Lai D., Storch N. I., 2017, *MNRAS*, 467, 3066

Antognini J. M. O., 2015, *MNRAS*, 452, 3610

Antoni A., MacLeod M., Ramirez-Ruiz E., 2019, *ApJ*, 884, 22

Antonini F., Gieles M., 2020, *Phys. Rev. D*, 102, 123016

Antonini F., Perets H. B., 2012, *ApJ*, 757, 27

Antonini F., Rasio F. A., 2016, *ApJ*, 831, 187

Antonini F., Murray N., Mikkola S., 2014, *ApJ*, 781, 45

Antonini F., Hamers A. S., Lithwick Y., 2016a, *AJ*, 152, 174

Antonini F., Chatterjee S., Rodriguez C. L., Morscher M., Pattabiraman B., Kalogera V., Rasio F. A., 2016b, *ApJ*, 816, 65

Antonini F., Toonen S., Hamers A. S., 2017, *ApJ*, 841, 77

Antonini F., Rodriguez C. L., Petrovich C., Fischer C. L., 2018, *MNRAS*, 480, L58

Ballone A., Costa G., Mapelli M., MacLeod M., Torniamenti S., Pacheco-Arias J. M., 2023, *MNRAS*, 519, 5191

Banerjee S., Baumgardt H., Kroupa P., 2010, *MNRAS*, 402, 371

Banerjee S., Belczynski K., Fryer C. L., Berczik P., Hurley J. R., Spurzem R., Wang L., 2020, *A&A*, 639, A41

Barker B. M., O'Connell R. F., 1975, *Phys. Rev. D*, 12, 329

Belczynski K., Kalogera V., Bulik T., 2002, *ApJ*, 572, 407

Belczynski K., Taam R. E., Kalogera V., Rasio F. A., Bulik T., 2007, *ApJ*, 662, 504

Belczynski K., Kalogera V., Rasio F. A., Taam R. E., Zezas A., Bulik T., Maccarone T. J., Ivanova N., 2008, *ApJS*, 174, 223

Belczynski K., Holz D. E., Bulik T., O'Shaughnessy R., 2016a, *Nature*, 534, 512

Belczynski K., et al., 2016b, *A&A*, 594, A97

Belczynski K., Repetto S., Holz D. E., O'Shaughnessy R., Bulik T., Berti E., Fryer C., Dominik M., 2016c, *ApJ*, 819, 108

Belczynski K., et al., 2020, *A&A*, 636, A104

Bhattacharya D., van den Heuvel E. P. J., 1991, *Phys. Repts.*, 203, 1

Blaauw A., 1961, *Bull. Astron. Inst. Netherlands*, 15, 265

Blaes O., Lee M. H., Socrates A., 2002, *ApJ*, 578, 775

Blagorodnova N., et al., 2017, *ApJ*, 834, 107

Boffin H. M. J., 2015, in Boffin H. M. J., Carraro G., Beccari G., eds, Astrophysics and Space Science Library Vol. 413, Astrophysics and Space Science Library. p. 153 (arXiv:1406.3473), doi:10.1007/978-3-662-44434-4_7

Bondi H., Hoyle F., 1944, *MNRAS*, 104, 273

Bonetti M., Haardt F., Sesana A., Barausse E., 2016, *MNRAS*, 461, 4419

Bonnell I. A., Bate M. R., 2005, *MNRAS*, 362, 915

Borkovits T., Hajdu T., Sztakovics J., Rappaport S., Levine A., Bíró I. B., Klagyivik P., 2016, *MNRAS*, 455, 4136

Breivik K., et al., 2020, *ApJ*, 898, 71

Bub M. W., Petrovich C., 2020, *ApJ*, 894, 15

Castor J. I., Abbott D. C., Klein R. I., 1975, *ApJ*, 195, 157

Claret A., Cunha N. C. S., 1997, *A&A*, 318, 187

Correia A. C. M., Laskar J., Farago F., Boué G., 2011, Celestial Mechanics and Dynamical Astronomy, 111, 105

Crawford J. A., 1955, *ApJ*, 121, 71

Crowther P. A., 2001, in Vanbeveren D., ed., Astrophysics and Space Science Library Vol. 264, The Influence of Binaries on Stellar Population Studies. p. 215 (arXiv:astro-ph/0010581), doi:10.1007/978-94-015-9723-4_17

Damour T., 2001, *Phys. Rev. D*, 64, 124013

De S., MacLeod M., Everson R. W., Antoni A., Mandel I., Ramirez-Ruiz E., 2020, *ApJ*, 897, 130

Dervişoğlu A., Pavlovski K., Lehmann H., Southworth J., Bewsher D., 2018, *MNRAS*, 481, 5660

Di Carlo U. N., Giacobbo N., Mapelli M., Pasquato M., Spera M., Wang L., Haardt F., 2019, *MNRAS*, 487, 2947

Di Carlo U. N., Mapelli M., Bouffanais Y., Giacobbo N., Santoliquido F., Bressan A., Spera M., Haardt F., 2020a, *MNRAS*, 497, 1043

Di Carlo U. N., et al., 2020b, *MNRAS*, 498, 495

Di Stefano R., 2020a, *MNRAS*, 491, 495

Di Stefano R., 2020b, *MNRAS*, 493, 1855

Dominik M., Belczynski K., Fryer C., Holz D. E., Berti E., Bulik T., Mandel I., O'Shaughnessy R., 2012, *ApJ*, 759, 52

Dong S., Katz B., Socrates A., 2014, *ApJ*, 781, L5

Dormand J. R., Prince P. J., 1978, Celestial Mechanics, 18, 223

Dosopoulou F., Kalogera V., 2016a, *ApJ*, 825, 70

Dosopoulou F., Kalogera V., 2016b, *ApJ*, 825, 71

Duchêne G., Kraus A., 2013, *ARAA*, 51, 269

Duquennoy A., Mayor M., 1991, *A&A*, 248, 485

Dvorkin I., Silk J., Vangioni E., Petitjean P., Olive K. A., 2015, *MNRAS*, 452, L36

Eggleton P. P., 1983, *ApJ*, 268, 368

Eggleton P., 2006, Evolutionary Processes in Binary and Multiple Stars

Eggleton P. P., Kiseleva-Eggleton L., 2001, *ApJ*, 562, 1012

Eggleton P. P., Kiseleva L. G., Hut P., 1998, *ApJ*, 499, 853

Einstein A., 1918, Sitzungsberichte der Königlich Preussischen Akademie der Wissenschaften, pp 154–167

Eldridge J. J., Izzard R. G., Tout C. A., 2008, *MNRAS*, 384, 1109

Erdem A., Öztürk O., 2014, *MNRAS*, 441, 1166

Fabrycky D., Tremaine S., 2007, *ApJ*, 669, 1298

Ford E. B., Kozinsky B., Rasio F. A., 2000, *ApJ*, 535, 385

Fragione G., Banerjee S., 2021, *ApJ*, 913, L29

Fragione G., Kocsis B., 2020, *MNRAS*, 493, 3920

Fryer C. L., Belczynski K., Wiktorowicz G., Dominik M., Kalogera V., Holz D. E., 2012, *ApJ*, 749, 91

Fuller J., Ma L., 2019, *ApJ*, 881, L1

GRAVITY Collaboration et al., 2018, *A&A*, 620, A116

Gao Y., Toonen S., Leigh N., 2023, *MNRAS*, 518, 526

García B., Mermilliod J. C., 2001, *A&A*, 368, 122

Gerosa D., Kesden M., Berti E., O'Shaughnessy R., Sperhake U., 2013, *Phys. Rev. D*, 87, 104028

Giacobbo N., Mapelli M., 2018, *MNRAS*, 480, 2011

Giacobbo N., Mapelli M., 2019, *MNRAS*, 482, 2234

Giacobbo N., Mapelli M., 2020, *ApJ*, 891, 141

Giacobbo N., Mapelli M., Spera M., 2018, *MNRAS*, 474, 2959

Glanz H., Perets H. B., 2021, *MNRAS*, 500, 1921

Glebbeek E., Pols O. R., 2008, *A&A*, 488, 1017

Glebbeek E., Gaburov E., Portegies Zwart S., Pols O. R., 2013, *MNRAS*, 434, 3497

Goldreich P., Soter S., 1966, Icarus, 5, 375

Gowers T., Barrow-Green J., Leader I., eds, 2008, The Princeton Companion to Mathematics. Princeton University Press, Princeton

Gräfener G., Hamann W. R., 2008, *A&A*, 482, 945

Gräfener G., Vink J. S., de Koter A., Langer N., 2011, *A&A*, 535, A56

Grishin E., Perets H. B., Fragione G., 2018, *MNRAS*, 481, 4907

Hamers A. S., 2021, *MNRAS*, 500, 3481

Hamers A. S., Dosopoulou F., 2019, *ApJ*, 872, 119

Hamers A. S., Lai D., 2017, *MNRAS*, 470, 1657

Hamers A. S., Safarzadeh M., 2020, *ApJ*, 898, 99

Hamers A. S., Rantala A., Neunteufel P., Preece H., Vynatheya P., 2021, *MNRAS*, 502, 4479

Hamers A. S., Glanz H., Neunteufel P., 2022, *ApJS*, 259, 25

Hamilton C., Rafikov R. R., 2019, *ApJ*, 881, L13

Harrington R. S., 1968, *AJ*, 73, 190

Hayashi T., Trani A. A., Suto Y., 2023, *ApJ*, 943, 58

Hirai R., Podsiadlowski P., Owocki S. P., Schneider F. R. N., Smith N., 2021, *MNRAS*, 503, 4276

Hoang B.-M., Naoz S., Kocsis B., Rasio F. A., Dosopoulou F., 2018, *ApJ*, 856, 140

Hobbs G., Lorimer D. R., Lyne A. G., Kramer M., 2005, *MNRAS*, 360, 974

Hrushow W. K., 1969, AIAA Journal, 7, 337

Hurley J. R., Pols O. R., Tout C. A., 2000, *MNRAS*, 315, 543

Hurley J. R., Tout C. A., Pols O. R., 2002, *MNRAS*, 329, 897

Hut P., 1981, *A&A*, 99, 126

Iben Icko J., Tutukov A. V., 1999, *ApJ*, 511, 324

Ito T., Ohtsuka K., 2019, Monographs on Environment, Earth and Planets, 7, 1

Ivanova N., et al., 2013, A&A Rev., 21, 59

Izzard R. G., Tout C. A., Karakas A. I., Pols O. R., 2004, *MNRAS*, 350, 407

Janka H.-T., Wongwathanarat A., Kramer M., 2022, *ApJ*, 926, 9

Kalogera V., 2000, *ApJ*, 541, 319

Kervella P., Thévenin F., Lovis C., 2017, *A&A*, 598, L7

Kippenhahn R., Kohl K., Weigert A., 1967, ZAp, 66, 58

Kirk B., et al., 2016, *AJ*, 151, 68

Klencki J., Nelemans G., Istrate A. G., Pols O., 2020, *A&A*, 638, A55

Klencki J., Nelemans G., Istrate A. G., Chruslinska M., 2021, *A&A*, 645, A54

Kobulnicky H. A., et al., 2014, *ApJS*, 213, 34

Kozai Y., 1962, *AJ*, 67, 591

Kremer K., et al., 2020, *ApJ*, 903, 45

Kroupa P., 2001, *MNRAS*, 322, 231

Kroupa P., 2002, Science, 295, 82

Kroupa P., Weidner C., Pflamm-Altenburg J., Thies I., Dabringhausen J., Marks M., Maschberger T., 2013, in Oswalt T. D., Gilmore G., eds, , Vol. 5, Planets, Stars and Stellar Systems. Volume 5: Galactic Structure and Stellar Populations. p. 115, doi:10.1007/978-94-007-5612-0_4

Lang K. R., 1992, Astrophysical Data I. Planets and Stars.

Langer N., 2009, *A&A*, 500, 133

Lépine S., Bongiorno B., 2007, *AJ*, 133, 889

Lidov M. L., 1962, Planet. Space Sci., 9, 719

Lithwick Y., Naoz S., 2011, *ApJ*, 742, 94

Liu B., Lai D., 2017, *ApJ*, 846, L11

Liu B., Lai D., 2018, *ApJ*, 863, 68

Liu B., Muñoz D. J., Lai D., 2015, *MNRAS*, 447, 747

Liu B., Lai D., Wang Y.-H., 2019, *ApJ*, 881, 41

Lu C. X., Naoz S., 2019, *MNRAS*, 484, 1506

Lubow S. H., Shu F. H., 1975, *ApJ*, 198, 383

MacLeod M., Macias P., Ramirez-Ruiz E., Grindlay J., Batta A., Montes G., 2017, *ApJ*, 835, 282

Madau P., Dickinson M., 2014, *ARAA*, 52, 415

Madau P., Fragos T., 2017, *ApJ*, 840, 39

Mandel I., Broekgaarden F. S., 2022, Living Reviews in Relativity, 25, 1

Mandel I., O'Shaughnessy R., 2010, Classical and Quantum Gravity, 27, 114007

Mandel I., de Mink S. E., 2016, *MNRAS*, 458, 2634

Mapelli M., 2016, *MNRAS*, 459, 3432

Mardling R. A., Aarseth S. J., 2001, *MNRAS*, 321, 398

Martinez M. A. S., Rodriguez C. L., Fragione G., 2022, *ApJ*, 937, 78

Mason B. D., Gies D. R., Hartkopf W. I., Bagnuolo William G. J., ten Brummelaar T., McAlister H. A., 1998, *AJ*, 115, 821

Mason B. D., Hartkopf W. I., Gies D. R., Henry T. J., Helsel J. W., 2009, *AJ*, 137, 3358

Mastrodemos N., Morris M., 1998, *ApJ*, 497, 303

Matese J. J., Whitmire D. P., 1983, *ApJ*, 266, 776

Mennekens N., Vanbeveren D., 2017, *A&A*, 599, A84

Menon A., et al., 2021, *MNRAS*, 507, 5013

Merritt D., 2013, Dynamics and Evolution of Galactic Nuclei

Michaely E., Perets H. B., 2014, *ApJ*, 794, 122

Moe M., Di Stefano R., 2015, *ApJ*, 810, 61

Moe M., Di Stefano R., 2017, *ApJS*, 230, 15

Motz L., 1952, *ApJ*, 115, 562

Muñoz D. J., Lai D., Liu B., 2016, *MNRAS*, 460, 1086

Naoz S., 2016, *ARAA*, 54, 441

Naoz S., Fabrycky D. C., 2014, *ApJ*, 793, 137

Naoz S., Farr W. M., Lithwick Y., Rasio F. A., Teyssandier J., 2011, *Nature*, 473, 187

Naoz S., Farr W. M., Rasio F. A., 2012, *ApJ*, 754, L36

Naoz S., Farr W. M., Lithwick Y., Rasio F. A., Teyssandier J., 2013a, *MNRAS*, 431, 2155

Naoz S., Kocsis B., Loeb A., Yunes N., 2013b, *ApJ*, 773, 187

Naoz S., Fragos T., Geller A., Stephan A. P., Rasio F. A., 2016, *ApJ*, 822, L24

Natarajan P., Pringle J. E., 1998, *ApJ*, 506, L97

Noutsos A., Kramer M., Carr P., Johnston S., 2012, *MNRAS*, 423, 2736

Noutsos A., Schnitzeler D. H. F. M., Keane E. F., Kramer M., Johnston S., 2013, *MNRAS*, 430, 2281

Olejak A., Fishbach M., Belczynski K., Holz D. E., Lasota J. P., Miller M. C., Bulik T., 2020, *ApJ*, 901, L39

Olejak A., Belczynski K., Ivanova N., 2021, *A&A*, 651, A100

Packet W., 1981, *A&A*, 102, 17

Paczyński B., 1967a, Acta Astron., 17, 193

Paczyński B., 1967b, Acta Astron., 17, 355

Paczyński B., 1971, *ARAA*, 9, 183

Paczynski B., 1976, in Eggleton P., Mitton S., Whelan J., eds, Vol. 73, Structure and Evolution of Close Binary Systems. p. 75

Park D., Kim C., Lee H. M., Bae Y.-B., Belczynski K., 2017, *MNRAS*, 469, 4665

Pastorello A., et al., 2019, *A&A*, 630, A75

Pavlovskii K., Ivanova N., 2015, *MNRAS*, 449, 4415

Pavlovskii K., Ivanova N., Belczynski K., Van K. X., 2017, *MNRAS*, 465, 2092

Pawlak M., et al., 2016, Acta Astron., 66, 421

Paxton B., Bildsten L., Dotter A., Herwig F., Lesaffre P., Timmes F., 2011, *ApJS*, 192, 3

Perets H. B., Fabrycky D. C., 2009, *ApJ*, 697, 1048

Perets H. B., Kenyon S. J., 2013, *ApJ*, 764, 169

Perets H. B., Kratter K. M., 2012, *ApJ*, 760, 99

Peters P. C., 1964, Physical Review, 136, 1224

Petrovich C., 2015, *ApJ*, 808, 120

Petrovich C., Antonini F., 2017, *ApJ*, 846, 146

Pijloo J. T., Caputo D. P., Portegies Zwart S. F., 2012, *MNRAS*, 424, 2914

Pinsonneault M. H., Stanek K. Z., 2006, *ApJ*, 639, L67

Planck Collaboration et al., 2016, *A&A*, 594, A13

Podsiadlowski P., Joss P. C., Hsu J. J. L., 1992, *ApJ*, 391, 246

Portegies Zwart S., Leigh N. W. C., 2019, *ApJ*, 876, L33

Portegies Zwart S. F., van den Heuvel E. P. J., 2016, *MNRAS*, 456, 3401

Preibisch T., Balega Y., Hofmann K.-H., Weigelt G., Zinnecker H., 1999, New A, 4, 531

Prinja B. K., 1992, in Drissen L., Leitherer C., Nota A., eds, Astronomical Society of the Pacific Conference Series Vol. 22, Nonisotropic and Variable Outflows from Stars. p. 167

Prodan S., Antonini F., Perets H. B., 2015, *ApJ*, 799, 118

Qin Y., Fragos T., Meynet G., Andrews J., Sørensen M., Song H. F., 2018, *A&A*, 616, A28

Racine É., 2008, *Phys. Rev. D*, 78, 044021

Raucq F., Rauw G., Gosset E., Nazé Y., Mahy L., Hervé A., Martins F., 2016, *A&A*, 588, A10

Renzo M., Götberg Y., 2021, *ApJ*, 923, 277

Rizzuto A. C., et al., 2013, *MNRAS*, 436, 1694

Rodriguez C. L., Antonini F., 2018, *ApJ*, 863, 7

Rodriguez C. L., Loeb A., 2018, *ApJ*, 866, L5

Rodriguez C. L., Chatterjee S., Rasio F. A., 2016a, *Phys. Rev. D*, 93, 084029

Rodriguez C. L., Zevin M., Pankow C., Kalogera V., Rasio F. A., 2016b, *ApJ*, 832, L2

Rose S. C., Naoz S., Geller A. M., 2019, *MNRAS*, 488, 2480

Safarzadeh M., Biscoveanu S., Loeb A., 2020, *ApJ*, 901, 137

Sana H., et al., 2012, Science, 337, 444

Sana H., et al., 2014, *ApJS*, 215, 15

Schneider F. R. N., Izzard R. G., Langer N., de Mink S. E., 2015, *ApJ*, 805, 20

Schneider F. R. N., Podsiadlowski P., Langer N., Castro N., Fossati L., 2016, *MNRAS*, 457, 2355

Schneider F. R. N., Ohlmann S. T., Podsiadlowski P., Röpke F. K., Balbus S. A., Pakmor R., Springel V., 2019, *Nature*, 574, 211

Schneider F. R. N., Ohlmann S. T., Podsiadlowski P., Röpke F. K., Balbus S. A., Pakmor R., 2020, *MNRAS*, 495, 2796

Schneider F. R. N., Podsiadlowski P., Müller B., 2021, *A&A*, 645, A5

Schwarzschild K., 1916, Abh. Konigl. Preuss. Akad. Wissenschaften Jahre 1906,92, Berlin,1907, 1916, 189

Sepinsky J. F., Willems B., Kalogera V., Rasio F. A., 2007, *ApJ*, 667, 1170

Sepinsky J. F., Willems B., Kalogera V., Rasio F. A., 2009, *ApJ*, 702, 1387

Sepinsky J. F., Willems B., Kalogera V., Rasio F. A., 2010, *ApJ*, 724, 546

Shakura N. I., Sunyaev R. A., 1973, *A&A*, 24, 337

Shao Y., Li X.-D., 2016, *ApJ*, 833, 108

Shappee B. J., Thompson T. A., 2013, *ApJ*, 766, 64

Siess L., Izzard R. G., Davis P. J., Deschamps R., 2013, *A&A*, 550, A100

Silsbee K., Tremaine S., 2017, *ApJ*, 836, 39

Soszyński I., et al., 2016, Acta Astron., 66, 405

Spera M., Mapelli M., 2017, *MNRAS*, 470, 4739

Spera M., Mapelli M., Bressan A., 2015, *MNRAS*, 451, 4086

Stegmann J., Antonini F., 2021, *Phys. Rev. D*, 103, 063007

Stegmann J., Vermeulen S. M., 2023, arXiv e-prints, p. arXiv:2301.02672

Stegmann J., Capelo P. R., Bortolas E., Mayer L., 2020, *MNRAS*, 492, 5247

Stegmann J., Antonini F., Schneider F. R. N., Tiwari V., Chattopadhyay D., 2022a, *Phys. Rev. D*, 106, 023014

Stegmann J., Antonini F., Moe M., 2022b, *MNRAS*, 516, 1406

Steinle N., Kesden M., 2021, *Phys. Rev. D*, 103, 063032

Stephan A. P., Naoz S., Ghez A. M., Witzel G., Sitarski B. N., Do T., Kocsis B., 2016, *MNRAS*, 460, 3494

Stephan A. P., Naoz S., Gaudi B. S., 2018, *AJ*, 156, 128

Stephan A. P., et al., 2019, *ApJ*, 878, 58

Stevenson S., Vigna-Gómez A., Mandel I., Barrett J. W., Neijssel C. J., Perkins D., de Mink S. E., 2017, Nature Communications, 8, 14906

Storch N. I., Anderson K. R., Lai D., 2014, Science, 345, 1317

Storch N. I., Lai D., Anderson K. R., 2017, *MNRAS*, 465, 3927

Suzuki T. K., Nakasato N., Baumgardt H., Ibukiyama A., Makino J., Ebisuzaki T., 2007, *ApJ*, 668, 435

The LIGO Scientific Collaboration et al., 2021, arXiv e-prints, p. arXiv:2111.03634

Thompson T. A., 2011, *ApJ*, 741, 82

Tiwari V., 2021, Classical and Quantum Gravity, 38, 155007

Tiwari V., 2022, *ApJ*, 928, 155

Tiwari V., Fairhurst S., 2021, *ApJ*, 913, L19

Tokovinin A. A., 2000, *A&A*, 360, 997

Tokovinin A., 2017, *ApJ*, 844, 103

Toonen S., Hamers A., Portegies Zwart S., 2016, Computational Astrophysics and Cosmology, 3, 6

Toonen S., Perets H. B., Hamers A. S., 2018, *A&A*, 610, A22

Toonen S., Portegies Zwart S., Hamers A. S., Bandopadhyay D., 2020, *A&A*, 640, A16

Toonen S., Boekholt T. C. N., Portegies Zwart S., 2022, *A&A*, 661, A61

Tout C. A., 2012, in Richards M. T., Hubeny I., eds, Vol. 282, From Interacting Binaries to Exoplanets: Essential Modeling Tools. pp 417–424, doi:10.1017/S1743921311027967

Tout C. A., Aarseth S. J., Pols O. R., Eggleton P. P., 1997, *MNRAS*, 291, 732

Tremaine S., Yavetz T. D., 2014, American Journal of Physics, 82, 769

Tremaine S., Touma J., Namouni F., 2009, *AJ*, 137, 3706

Tylenda R., Kamiński T., 2016, *A&A*, 592, A134

Vanbeveren D., 1991, *A&A*, 252, 159

Vick M., Lai D., 2019, *Phys. Rev. D*, 100, 063001

Vick M., Lai D., Anderson K. R., 2019, *MNRAS*, 484, 5645

Vigna-Gómez A., Justham S., Mandel I., de Mink S. E., Podsiadlowski P., 2019, *ApJ*, 876, L29

Vigna-Gómez A., Toonen S., Ramirez-Ruiz E., Leigh N. W. C., Riley J., Haster C.-J., 2021, *ApJ*, 907, L19

Vigna-Gómez A., Liu B., Aguilera-Dena D. R., Grishin E., Ramirez-Ruiz E., Soares-Furtado M., 2022, *MNRAS*, 515, L50

Vink J. S., 2017, Philosophical Transactions of the Royal Society of London Series A, 375, 20160269

Vink J. S., de Koter A., Lamers H. J. G. L. M., 2001, *A&A*, 369, 574

Vink J. S., Muijres L. E., Anthonisse B., de Koter A., Gräfener G., Langer N., 2011, *A&A*, 531, A132

Wang H., Stephan A. P., Naoz S., Hoang B.-M., Breivik K., 2021, *ApJ*, 917, 76

Wellstein S., Langer N., Braun H., 2001, *A&A*, 369, 939

Will C. M., 2017, *Phys. Rev. D*, 96, 023017

Wu Y., 2018, *AJ*, 155, 118

Wu Y., Murray N., 2003, *ApJ*, 589, 605

Yoon S. C., Woosley S. E., Langer N., 2010, *ApJ*, 725, 940

Zahn J. P., 1975, *A&A*, 41, 329

Zahn J. P., 1977, *A&A*, 57, 383

Zahn J. P., 1989, *A&A*, 220, 112

Zevin M., Bavera S. S., 2022, *ApJ*, 933, 86

Zevin M., Berry C. P. L., Coughlin S., Chatziioannou K., Vitale S., 2020, *ApJ*, 899, L17

Zevin M., et al., 2021, *ApJ*, 910, 152

Ziosi B. M., Mapelli M., Branchesi M., Tormen G., 2014, *MNRAS*, 441, 3703

de Mink S. E., Pols O. R., Hilditch R. W., 2007, *A&A*, 467, 1181

de Mink S. E., Langer N., Izzard R. G., Sana H., de Koter A., 2013, *ApJ*, 764, 166

de Val-Borro M., Karovska M., Sasselov D., 2009, *ApJ*, 700, 1148

de Vries N., Portegies Zwart S., Figueira J., 2014, *MNRAS*, 438, 1909

van Rensbergen W., De Greve J. P., Mennekens N., Jansen K., De Loore C., 2010, *A&A*, 510, A13

van Son L. A. C., et al., 2022, *ApJ*, 940, 184